Title
Chemical Consequences of Heme Distortion and the Role of Heme Distortion in Signal Transduction of H-NOX Proteins

Author
Olea, Jr., Charles

Publication Date
2010

Peer reviewed|Thesis/dissertation

Chemical Consequences of Heme Distortion and the Role of Heme Distortion in Signal Transduction of H-NOX Proteins

by

Charles Olea, Jr.

A dissertation submitted in partial satisfaction of the
requirements for the degree of

Doctor of Philosophy

in

Molecular and Cell Biology

in the

Graduate Division

of the

University of California, Berkeley

Committee in charge:

Professor Michael A. Marletta, Chair
Professor John Kuriyan
Professor James M. Berger
Professor Matthew B. Francis

Spring 2010

Chemical Consequences of Heme Distortion and the
Role of Heme Distortion in Signal Transduction of H-NOX Proteins

by Charles Olea, Jr.

Abstract

Chemical Consequences of Heme Distortion and the
Role of Heme Distortion in Signal Transduction of H-NOX Proteins
by
Charles Olea, Jr.
Doctor of Philosophy in Molecular and Cell Biology
University of California, Berkeley
Professor Michael A. Marletta, Chair

Nitric oxide (NO) signaling in mammals controls important processes such as smooth muscle relaxation and neurotransmission by the activation of soluble guanylate cyclase (sGC). NO binding to the heme domain of sGC leads to dissociation of the iron–histidine (Fe–His) bond, which is required for enzyme activity. The heme domain of sGC belongs to a larger class of proteins called H-NOX (Heme-Nitric oxide/OXygen) binding domains. H-NOX proteins act as sensors for nitric oxide (NO) or oxygen (O_2). The crystal structure of a H-NOX domain from *Thermoanaerobacter tengcongensis* (*Tt* H-NOX) contains one of the most distorted hemes reported to date. In this dissertation, I engineered *Tt* H-NOX to adopt a flatter heme by mutating a conserved residue in the H-NOX family. Decreasing heme distortion in *Tt* H-NOX increases affinity for oxygen and decreases the reduction potential of the heme iron. Additionally, flattening the heme is associated with significant shifts at the N-terminus of the protein. These results show a clear link between the heme conformation and *Tt* H-NOX structure and demonstrate that heme distortion is an important determinant for maintaining biochemical properties in H-NOX proteins.

The reduction potential of *Tt* H-NOX was rationally modulated through mutations of the protein scaffold. The degree of heme distortion is directly correlated with the reduction potential of the heme iron. Inducing planarity in the heme causes overlap of the porphyrin orbitals with the d-orbitals of the iron, leading to increased electron density at the iron, which lowers the reduction potential. Rational design of *Tt* H-NOX to broaden the reduction potential range and change the function of the protein may potentially be used for further applications.

NMR solution structures of H-NOX proteins show a conformational change upon disconnection of the heme and proximal helix. The atomic details of these conformational changes are lacking in the NMR structures, however, especially at the heme pocket. I solved a high-resolution crystal structure of a H-NOX mutant mimicking a broken Fe–His bond. This mutant exhibits specific heme conformational changes and a major N-terminal displacement relative to the wild-type H-NOX protein. Fe–His ligation is ubiquitous in all H-NOX domains, thus the heme and protein conformational changes observed in this study are likely to occur throughout the H-NOX family when NO binding ruptures the Fe–His bond.

All mechanistic studies on H-NOX activation have been focused on the response to NO. However, little is known about the sub-class of H-NOX proteins that are predicted to sense oxygen (O_2). A key question is how these H-NOX proteins respond to O_2 binding. I solved the crystal structure of an unligated mimic of *Tt* H-NOX at high resolution. When compared to wild-type, which is O_2-bound, large conformation changes in the protein and heme are observed. Essentially, O_2 acts as a link between the N- and C-terminal domains in *Tt* H-NOX and locks the protein and heme in a particular state. *Tt* H-NOX is part of a larger protein that contains a methyl-accepting chemotaxis domain that is predicted to sense O_2 in *T. tengcongensis*. Follow-up experiments will focus on developing an assay in Tar4 that can test the response to O_2 and the importance of heme distortion on activity.

Dedication

For My Father Charles Olea, Sr.

Table of Contents

Abstract **1**

Dedication ..... **i**

Table of Contents ..... **ii**

List of Figures and Tables ..... **iv**

Acknowledgements ..... **ix**

Chapter 1: H-NOX Proteins and Significance of Heme Distortion **1**

Nitric Oxide Function in Biology 1
H-NOX Family of Hemoproteins 2
Crystal Structure of *Tt* H-NOX 3
Heme Distortion in *Tt* H-NOX 4
Significance of Heme Distortion in Biology 5
Thesis 6

Chapter 2: Probing the Role of Heme Distortion in H-NOX Protein Family **8**

Background 8
Materials and Methods 10
Results and Discussion 11
Conclusions 19

Chapter 3: Modulating the Redox Potential of a Heme Using an H-NOX Domain **20**

Materials and Methods 21
Results and Discussion 22
Conclusions 31

Chapter 4: Insights Into the Molecular Mechanism of H-NOX Activation **33**

Background 33
Materials and Methods 34
Results and Discussion 35
Conclusions 41

Chapter 5: Crystal Structure of a 5-coordinate Unligated Mimic of an O_2-binding H-NOX **42**

Background 42
Materials and Methods 43
Results and Discussion 44
Conclusions 48

Chapter 6: Initial Biochemical Characterization of Tar4 ..... **50**

Background 50
Materials and Methods 51
Results 52

Future Directions....54
References....55
Appendix....59

List of Figures and Tables

Figure 1.1. NO signaling in mammals. NO is produced by NOS in the endothelial cell by the oxygen dependent conversion of L-arginine to citruline. NO freely diffuses across the **....1** membrane and coordinates to the heme in sGC. NO binding leads to an increase in cGMP production in the smooth muscle cell. **.....2**

Figure 1.2. Topology of the H-NOX Protein Family. sGC is comprised of an H-NOX, PAS, and guanylate cyclase domain. A conserved coil-coil domain separates the PAS and **....2** cyclase domain. Mammalian sGC H-NOX domains selectively bind and are activated by NO in the presence of atmospheric oxygen. Atypical sGC binds both NO and O_2 and, in contrast, is inhibited upon ligand binding. H-NOX proteins in facultative aerobes are found in the same operon as histidine kinases, GGDEF-EAL, or HD-GYP proteins and selectively bind NO similar to mammalian H-NOX domains. In obligate anaerobes, HNOX domains bind both NO and O_2 and are fused to methyl-accepting chemotaxis proteins. **.....3**

Figure 1.3. Crystal Structure of *Tt* H-NOX. Shown is molecule A (monoclinic PDB ID: 1U55). The heme is shown in ball and stick and spherical representation (red). The distal hydrogen bonding residues Trp-9, Asn-74, and Tyr-140 are shown in orange. The N-terminal domain is mostly α-helical, whereas the C-terminus is predominately β-sheet. **.....4**

Figure 1.4. Structural changes associated with heme distortion. Shown are wild-type molecules A and B (PDB ID 1U55) in purple and orange, respectively. A shift of the N-terminus is associated with heme flattening. Conserved residues are involved in the conformational change and maintenance of heme distortion, which suggests that the heme/protein conformation coupling is part of a signal transduction mechanism. **.....5**

Figure 1.5. Comparison of *Tt* H-NOX heme with other distorted hemes. Pyrrole groups labeled A-D. Ball-and-stick representation of oxy-myoglobin heme (blue) compared with *Tt* H-NOX and other distorted hemes. This figure was obtain from Pellicena *et al*.,[19] National Academy of Sciences. **.....6**

Figure 2.1. Heme distortion in wild-type *Tt* H-NOX. a) Ball-and-stick and space filling model of Pro115 and the surrounding heme environment of wild-type *Tt* H-NOX.[19] The invariant Pro115 (orange) makes the largest contribution to heme (red) distortion in *Tt* H-NOX. Pro115 pushes up against pyrrole D, which causes a pronounced kink in the connected propionate group. Out-of-plane distortions of up to 2 Å are observed in *Tt* H-NOX. b) Heme prosthetic group with pyrrole groups A–D labeled. Figure 2.1 was obtained from Olea *et al*.[39], The American Chemical Society. **.....9**

Figure 2.2 Structural comparison of P115A with wild-type *Tt* H-NOX. The heme in P115A (silver) is flatter than wild-type (gold). Significant translations are observed in the N-terminal region of the heme-flattened P115A crystal structure. Shown are molecule A from the monoclinic crystal structure of *Tt* wild-type H-NOX and molecule D from the P115A crystal structure. Figure 2.2 was obtained from Olea *et al*.[39], The American Chemical Society. **.....12**

Figure 2.3. N-Terminal movement from wild-type *Tt* H-NOX (WT) *versus* heme distortion in P115A. The N-terminal (residues 1–83) rms deviation (Å) was calculated and plotted *versus* rms deviation (Å) from planarity for each of the four molecules in the

asymmetric unit cell (A–D). Wild-type molecule A in the monoclinic space group was used for analysis. Figure 2.3 was obtained from Olea *et al*.[39], The American Chemical Society. **...14**
Figure 2.4. The effect of heme flattening on the N-terminal domain. Shown is a comparison of P115A molecule D (silver) and wild-type monoclinic *Tt* H-NOX molecule A (gold) heme/N-terminal interface. The planar heme makes new contacts with Met1 and Ile5 of α-helix A, which shifts the helix away from the C-terminal domain. Shifting of α-helix A, along with the rest of the N-terminal region, causes shifts over 4.9 Å. Figure 2.4 was obtained from Olea *et al*.[39], The American Chemical Society. **.....16**
Figure 2.5. Comparison of the iron–histidine bond geometry. Shown are the iron–histidine tilts of a) wild-type *Tt* H-NOX (gold) and b) P115A (silver). The least-squares plane of the heme was calculated using the four pyrrole nitrogens of the heme (other atoms were excluded because of the high degree of distortion) and the five imidazole ring atoms of His102 using MOLEMAN2.[52] Wild-type has a tilt of 78°, whereas P115A has a tilt of 87°. Figure 2.5 was obtained from Olea *et al*.[39], The American Chemical Society. **.....17**
Figure 2.6. Reduction potential of wild-type *Tt* H-NOX and P115A. a) Titration spectra for wild-type *Tt* H-NOX and P115A. b) Titration curves for wild-type *Tt* H-NOX and P115A. The reduction potentials of P115A and wild-type *Tt* H-NOX were determined against the standard hydrogen electrode (SHE). The ratio of reduced Fe^{2+} to oxidized Fe^{3+} heme was measured on the basis of their α/β maximum at approximately 557 nm for wild-type. The difference in absorbance of the α/β maximum for reduced and the α/β minimum for oxidized was used to calculate the fraction reduced for P115A. The voltage against the SHE was measured for both oxidative and reductive titrations of wild-type and P115A. Error bars represent the standard error. Figure 2.6 was obtained from Olea *et al*.[39], The American Chemical Society. **.....18**
Figure 3.1. Heme Distortion in wild-type *Tt* H-NOX. A) Heme prosthetic group with pyrrole groups A-D labeled. B) Ball-and-stick and space filling model of Ile-5 and C) Pro-115 and the surrounding heme environment of wild-type *Tt* H-NOX. Ile-5 and Pro-115 push down and up against the heme, respectively, causing pronounced kinks in the heme. Out-of-plane distortions up to 2 Å are observed in the crystal structure. **.....23**
TABLE 3.1. Statistics of crystallographic data collection and refinement statistics.....24
Figure 3.2. Comparison of mutants of *Tt* H-NOX with wild-type *Tt* H-NOX. Shown are A) I5L molecule B (blue), B) I5L/P115A molecule A (green), and C) P115A molecule D (silver) overlaid with wild-type *Tt* H-NOX monoclinic molecule A. All mutants of *Tt* H-NOX have been crystallized with distinct degrees of heme distortion and N-terminal movements from wild-type. **.....25**
Figure 3.3. Reduction Potential of wild-type and mutants. Titration curves for wild-type[39], I5L, I5L/P115A, and P115A[39] were determined against the standard hydrogen electrode (SHE). The ratio of reduced Fe^{2+} to oxidized Fe^{3+} heme was measured based on their α/β maximum at approximately 557 (reduced) nm for wild-type and I5L. The difference absorbance of the a/b maximum for reduced and the α/β minimum for oxidized was used to calculate the fraction reduced for I5L/P115A and P115A. The voltage against the SHE was measured for both oxidative and reductive titrations of wild-type and mutants. Error bars represent the standard error for wild-type and P115A and range and standard deviation for I5L and I5L/P115A, respectively. **.....26**

Figure 3.4. Heme distortion versus reduction potential in wild-type and mutants. Plotted is the mean rms deviation from planarity of wild-type and mutants versus the mean reduction potential against SHE. The error bars for the potential represent the standard error for wild-type and P115A and the range and standard deviation for I5L and I5L/P115A. The vertical bars for the rmsd from planarity represent the range of values for all molecules in the AU for each protein. **27**

Figure 3.5. Ferric Spectra of wild-type and mutants. A) Full spectra of wild-type mutants. B) Values for λ max of the Soret and α/β regions. Spectral zoom in on the C) Soret and D) α/β regions of wild-type and planar mutants. **28**

Figure 3.6. pH titration curves and pK_a values of wild-type and mutants. Titrations for wild-type and I5L were fit to the Henderson-Hasselbalch equation. Error bars for wild-type and I5L represent the standard deviation. The pK_a values for I5L/P115A and P115A could not be determined within the range of the experiment. **29**

Figure 3.7. Theoretical orbital energy schematic of distorted and planar heme orbital interactions. Shown is a model of the relative energies of the d_x2-$_y2$ and d_z2 orbitals in a distorted and planar heme. Orbital spheres are modeled in for the iron d-orbitals, the lone pairs of the nitrogen pyrrole groups in the heme, and the nitrogen in the proximal histidine. **30**

Figure 4.1. H102G mutant rationale. Nitric oxide (NO) binds in a five-coordinate state where the proximal Fe-His bond is broken, which leads to a displacement of the heme and proximal α-helix (α-helix F). Displacement of the heme and proximal helix in the axial histidine mutant. Figure 4.1 was adapted from Olea *et al.*,[85] John Wiley & Sons, Inc. **32**

TABLE 1. Statistics of crystallographic data collection and refinement **34**

Figure 4.2. Electron density map and structural comparison of H102G (PDB ID: 3LAH and 3LAI) versus wild type (PDB ID: 1U56). a) 2Fo - Fc electron density map of the heme pockets in H102G crystal form F2 (PDB ID: 3LAI) for molecules A and B at 1.0σ contour levels. The imidazoles and hemes were omitted during the generation of the electron density map. b) H102G heme cofactor (maroon) overlaid with wild type (gold). The heme cofactor in H102G adopts a significantly different conformation when compared with wild type. Pyrroles A and D move toward the distal pocket. Figure 4.2 was adapted from Olea *et al.*,[85] John Wiley & Sons, Inc. **36**

Figure 4.3. Effects of H102G on the overall structure. Overall structural comparison of H102G (maroon) versus wild type (gold). A significant N-terminal shift away from wild type is observed in H102G. Shown are F2 molecule B and molecule A for H102G and wild type, respectively. Figure 4.3 was adapted from Olea *et al.*,[85] John Wiley & Sons, Inc. **37**

Figure 4.4. Effects of H102G on the local heme environment. A) Pyrrole A, Met-1, and Ile-5 move with the heme causing large conformational changes at the N-terminus. B) The propionate group attached to pyrrole A moves above the heme plane along with an insertion of the loop following α-Helix F. The H102G mutant allows for displacement of α-helix F away from the heme cofactor. Figure 4.1 was adapted from Olea *et al.*,[85] John Wiley & Sons, Inc. **38**

Figure 5.1. Zn-porphyrin acts as a mimic of the ferrous unligated state and native incorporation of orthogonal porphyrins. A) Schematic of oxygen binding in H-NOX domains. In atypical sGC, cyclase activity is inhibited upon binding oxygen. B) Zn-porphyrin acts as a mimic of the ferrous unligated H-NOX protein. C) Schematic of the heme knock-out *E. coli* cell line. The *E. coli* strain has a step in the heme biosynthesis pathway

mutated and an uncharacterized heme intake mutation. Orthogonal porphyrins are supplemented during protein expression are natively incorporated into heme proteins. Figure 5.1C was obtained from Woodward *et al.*,[94] Nature Publishing Group. **.....43**
Figure 5.2. Electron Density Map of Zn *Tt* H-NOX. The Zn-porphyrin is shown in red and His-102 is shown in orange. The electron density map was calculated with the Zn-porphyrin and His-102 residue omitted at 1.5 σ. The electron density is continuous between the His and Zn bond. Importantly, no electron density is observed above the heme. **.....45**
TABLE 5.1. Preliminary Statistics of crystallographic data collection and refinement statistics.....45
Figure 5.3. Comparison of Zn *Tt* H-NOX with Wild-type. Zn molecule A and wild-type molecule A (1U55) are shown in maroon and gold, respectively. A shift over 6 Å at the N-terminus is observed upon oxygen binding. The 5-coordinate Zn-porphyrin mimic is significantly flatter than wild-type. **.....46**
Figure 5.4. Hydrogen bonding network in wild-type vs. Zn *Tt* H-NOX. The distal hydrogen bonding residues Trp-9, Asn-74, and Tyr-140 are shown. Zn and wild-type *Tt* H-NOX residues are shown in maroon and gold, respectively. All hydrogen-bonding residues are farther away from the metal center in Zn *Tt* H-NOX. **.....47**
Figure 5.5. Proposed Model for Response for Oxygen-binding. Oxygen links the N-terminus to the C-terminal domain in *Tt* H-NOX. An N-terminal shift over 6 Å is observed upon oxygen binding. **.....48**
Figure 6.1. Tar4 is Predicted to be Involved in Chemotaxis. Tar4 contains an H-NOX, type-2 transmembrane spanning, and a methyl-accepting chemotaxis (MCP) domain. It is predicted that the H-NOX domain will bind oxygen and activate the MCP domain to become methylated by the methyltranferase, *Tt* CheR2. The methylated MCP may act on downstream proteins leading to chemotaxis in *T. tengcongensis*. **.....50**
Figure 6.2. Reconstitution of Tar4 activity. Tar4 activity end-point assays after 30 min. are shown. Tar4 is active in the presence of *Tt* CheR2 and SAM. Negative control membranes and reactions without *Tt* CheR2 show no activity. MCPc249 is active in the presence of *Tt* CheR2 and SAM. **.....53**
Figure 6.3. MCPc249 is Methylated at Two Sites. Nanoelectrospray ionization of the intact MCPc249 with (+) and without (-) *Tt* CheR2. An increase in mass of 28 Da is observed in the presence of SAM and *Tt* CheR2 indicative of two sites of methylation. **.....53**
Figure 6.4. Identification of Methylation Sites in MCPc249. MCPc249 was methylated and digested with trypsin. The digested protein was analyzed using liquid chromatography tandem mass spectroscopy (MS/MS). Highlighted residues are covered peptides. Glu-557 was identified as being methylated. **.....54**
Table A1. Heme deviations from planarity of P115A and wild-type *Tt* H-NOX[a] 59
Table A2. Heme deviations from planarity in the crystal structure of P115A.....59
Table A3. N-terminal and overall rms deviation of P115A from wild-type *Tt* H-NOX. .60
Figure A1a. 61
Figure A1b. 61
Figure A1c. 62
Figure A1d. 63
Table A4. O_2-binding kinetic constants for *Tt* H-NOX and some ferrous heme proteins64
Table A5. Net partition coefficient difference of mutants of *Tt* H-NOX 65

Table A6. Heme deviations from planarity of mutants of and wild-type *Tt* H-NOX[a].....66
Table A7. Heme deviations from planarity in the crystal structure of P115A.....68
Table A8. Soret and α/β values for ferric wild-type and mutants of *Tt* H-NOX at pH 7.5 70
Table A9. N-terminal root mean square deviation (rmsd) values for H102G from wild-type.....70
Table A10. NSD calculations for wild-type and H102G.....70
Table A11. Distances of bond in the heme pocket of wild-type and Zn *Tt* H-NOX. 71
Table A12. Rmsd from planarity and NSD calculations for Zn *Tt* H-NOX. 71
Table A13. N-terminal root mean square deviation (rmsd) values for Zn *Tt* H-NOX....72

Acknowledgements

I am truly fortunate to have Michael Marletta as my scientific mentor. His consummate professionalism and excitement for science has set a great example for me. He sets a high bar for excellence and has been there every step of the way. It has been a fantastic six years at Berkeley. Thank you Michael.

I would like to thank John Kuriyan for his generosity and support, especially during my first few years in graduate school. He treated me as if I was his own graduate student, and I thank him for inviting me to learn X-ray crystallography in his lab. I would like to thank Susan Marqusee for the opportunity to work in her lab the summer before I started graduate school, my first rotation, and support during my final year in graduate school.

My senior labmates and good friends, Dr. Nathaniel Martin and Dr. Mark Price, were there from day one. I considered them my "big" brothers in the lab. They gave me invaluable scientific advice on my project and made lab an enjoyable place to be. I thank Nathaniel for advice on dealing with the stresses of graduate school and the fun times we had outside lab. I thank Mark for helping me keep focused on my project goals and for tips on skateboarding.

The opportunity to collaborate with my labmates helped me go beyond the scope of my own project. Mike Winter and I worked on several projects together and it has been a delight to work with him. I thank Mike for his critical input on all my manuscripts and seminar preparations. Europe was fun too.

I thank my three Stanley Hall baymates Dr. Jacquin Niles, Dr. Steve Reece, and Mark Herzik. Jacquin gave me great input on the development of my biochemical experiments. Steve and I had many invaluable scientific conversations that helped me further develop my project. I had a blast during Mark's rotation, and I am glad to see that he will continue X-ray crystallography projects in the lab.

I would like to thank Josh Woodward and Theo Agapie for scientific advice and the exciting opportunity to collaborate with them on their NOS projects. I thank Jungjoo Yoon for his advice on the inorganic aspects of my research and the opportunity to collaborate with him on his project. I thank Lars Plate and Emily Weinert and the rest of the H-NOX group for critical discussions and input on my research.

I thank my rotation mentors and collaborators Patricia Pellicena and Liz Boon for helping me get started in the lab. I thank Debora Makino, Meindert Lamers, Xuewu Zhang, Nick Levinson and the rest of the Kuriyan Lab members for help learning X-ray crystallography and for preparation for my qualifying exam. I thank all past and present members of the Marletta and Kuriyan labs that I have not mentioned.

Most importantly I want to thank my father, Charles Olea, Sr., for his love and support throughout my whole education. I could not have done this without him.

Chapter 1: H-NOX Proteins and Significance of Heme Distortion

Nitric Oxide Function in Biology

Nitric oxide (NO) is a free radical diatomic gas that is toxic to humans and a major component of air pollution.[1,2] Despite its inherent toxicity, NO is involved in several crucial biological functions. For example, macrophages use NO as a weapon against pathogenic bacteria by reacting with superoxide (O_2^-), forming reactive oxygen species (ROS), which causes oxidative damage and destroys the invading bacteria.[3] Surprisingly, NO is produced in mammals and serves as an important signaling molecule that is involved in processes such as smooth muscle relaxation and neurotransmission.[4,5]

NO is produced by nitric oxide synthase (NOS) from arginine, molecular oxygen, and NADPH. NO freely diffuses across membranes binding to the heme domain of the primary mammalian receptor for NO, soluble guanylate cyclase (sGC, Figure 1.1).[6] The heme domain of sGC is located at the N-terminus followed by a PAS domain, coil-coil region, and a catalytic domain (Figure 1.2) that converts GTP to GMP. Upon binding NO, the catalytic activity of the cyclase domain increases two orders of magnitude. cGMP acts as a secondary messenger for NO that activates cGMP-dependent kinases which regulate important biological processes such as smooth muscle relaxation.[7]

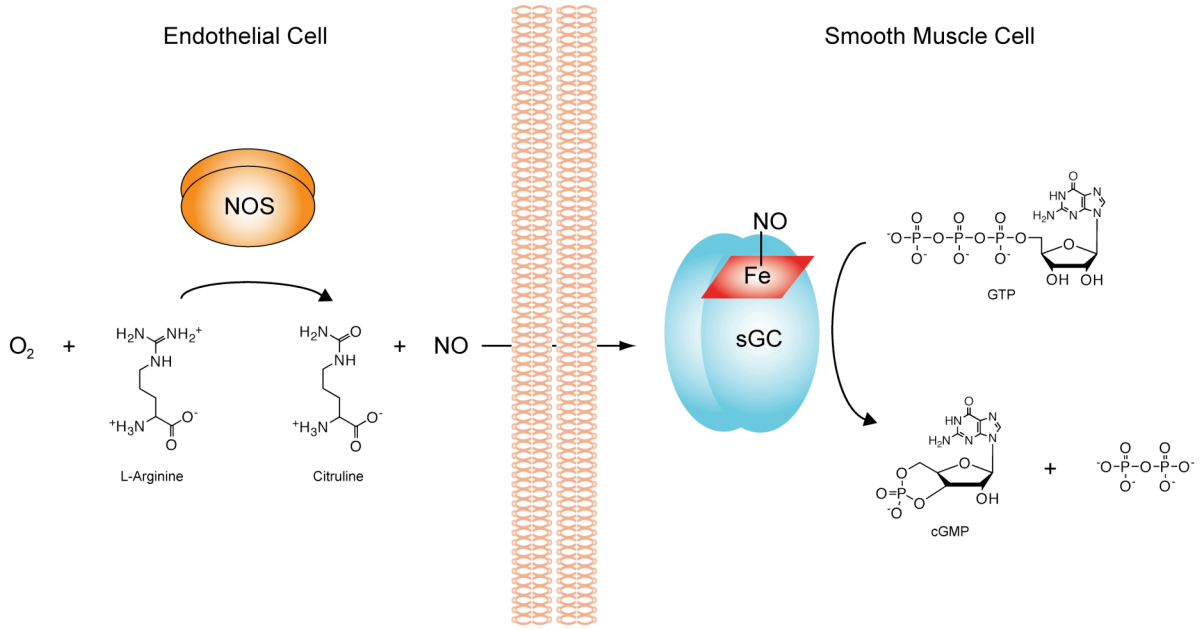

Figure 1.1. NO signaling in mammals. NO is produced by NOS in the endothelial cell by the oxygen dependent conversion of L-arginine to citruline. NO freely diffuses across the

membrane and coordinates to the heme in sGC. NO binding leads to an increase in cGMP production in the smooth muscle cell.

H-NOX Family of Hemoproteins

The heme domain of sGC belongs to a larger class of proteins called **H**eme **N**itric oxide/**OX**ygen binding (H-NOX) proteins.[8,9] Interestingly, H-NOX domains are found in bacteria where they are either fused to or part of the same operon with putative signaling proteins such as histidine kinases and methyl-accepting chemotaxis proteins (Figure 1.2). H-NOX proteins from facultative aerobes bind NO selectively over O_2 like their sGC counterpart. However, H-NOX domains from obligate anaerobes[9], *C. elegans*[10], and *Drosophila*[11] bind both NO and O_2.[12-14] Sequence homology and association with signaling proteins suggest that lower eukaryotic and prokaryotic H-NOX domains likely serve as sensors for NO and O_2.

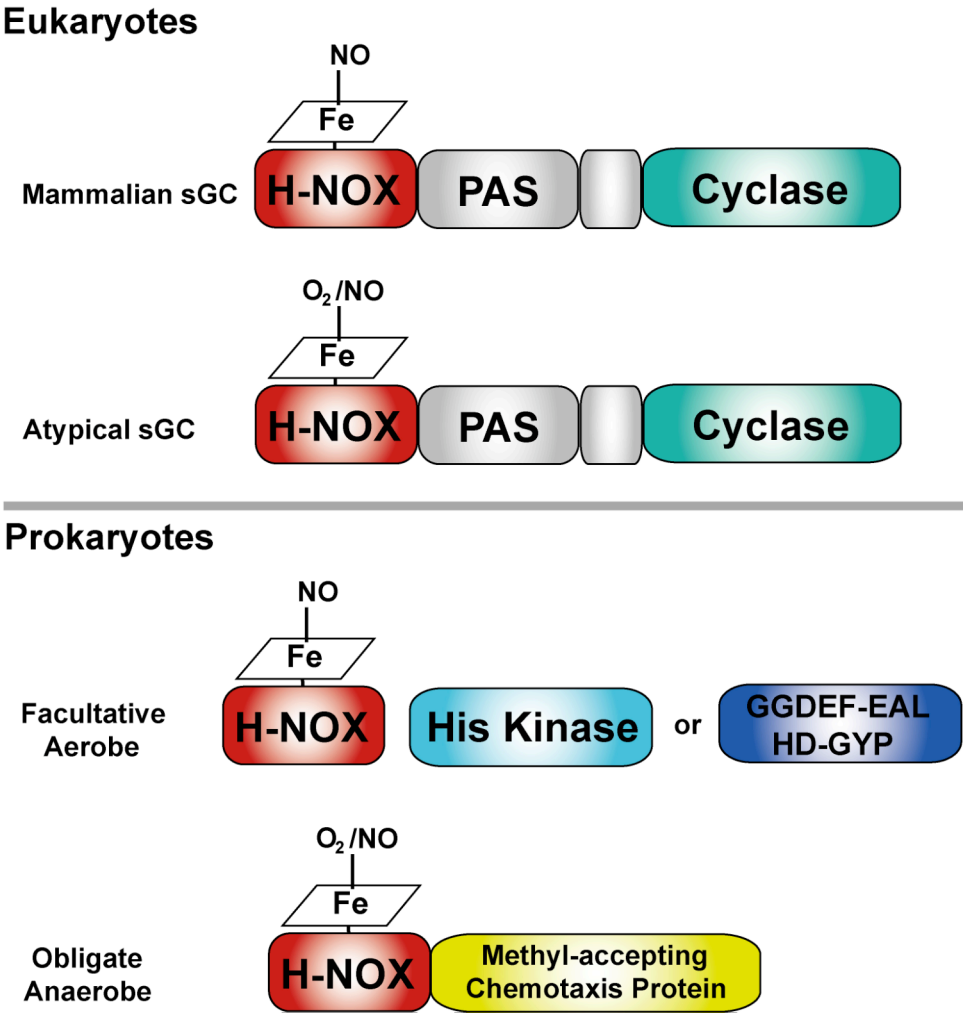

Figure 1.2. Topology of the H-NOX Protein Family. sGC is comprised of an H-NOX, PAS, and guanylate cyclase domain. A conserved coil-coil domain separates the PAS and

cyclase domain. Mammalian sGC H-NOX domains selectively bind and are activated by NO in the presence of atmospheric oxygen. Atypical sGC binds both NO and O_2 and, in contrast, is inhibited upon ligand binding. H-NOX proteins in facultative aerobes are found in the same operon as histidine kinases, GGDEF-EAL, or HD-GYP proteins and selectively bind NO similar to mammalian H-NOX domains. In obligate anaerobes, HNOX domains bind both NO and O_2 and are fused to methyl-accepting chemotaxis proteins.

Spectral data with sGC demonstrate that NO binds to the ferrous unligated state of the heme, forms a transient six-coordinate state, and ruptures the Fe-histidine bond forming and 5-coordinate nitrosyl complex.[15-17] The H-NOX from Shewanella oneidensis acts similarly. The 5-coordinate nitrosyl complex inhibits autophosphoylation of its associated histidine kinase.[18] It has been suggested that breakage of the Fe-his bond leads to a conformational change in the H-NOX domain that regulates activity. The sGC homolog in *Drosophila*, Gyc-88E, binds O_2 and NO in a 6-coordinate complex, which as opposed to mammalian sGC with NO bound, inhibits cyclase activity.[11]

Crystal Structure of *Tt* H-NOX

The first crystal structure of an H-NOX domain was solved from an obligate anaerobic bacterium *Thermoanaerobacter tengcongensis* (*Tt* H-NOX).[19,20] The crystal structure is of an H-NOX domain at the N-terminus (residues 1-188) of a larger protein called Tar4. The structure was solved to 1.77 Å and has a unique protein fold not previously observed. The crystal structure was crystallized in two coordination states: six-coordinate ferrous-oxy and six-coordinate ferric-hydroxide. Both distal ligands, oxygen and hydroxide, are stabilized by a distal hydrogen bonding network conserved in H-NOX domains found in obligate anaerobes. The residue directly hydrogen bonding to the ligand in the distal pocket is Tyr-140, which is stabilized by a hydrogen-bonding network comprised of Thr-8, Trp-9, Thr-12, and Asn-74.

The distal hydrogen-bonding network in *Tt* H-NOX is conserved in obligate anaerobes and atypical sGCs all of which bind O_2. It was shown that this hydrogen-bonding network was responsible for molecular basis of O_2 discrimination in H-NOX domains.[12,13,21] Stable Oxygen binding was eliminated when Trp-9 and Tyr-140 was removed from *Tt* H-NOX. Introduction of a tyrosine in the distal pocket of β1(1-385), a non-oxygen binder, led to oxygen binding. The crystal structure revealed that the YxSxR motif, which is completely conserved in the H-NOX family[8], makes hydrogen-bonding contacts to the heme propionate groups. The YxSxR motif has previously shown to be critical for heme binding in sGC.[22]

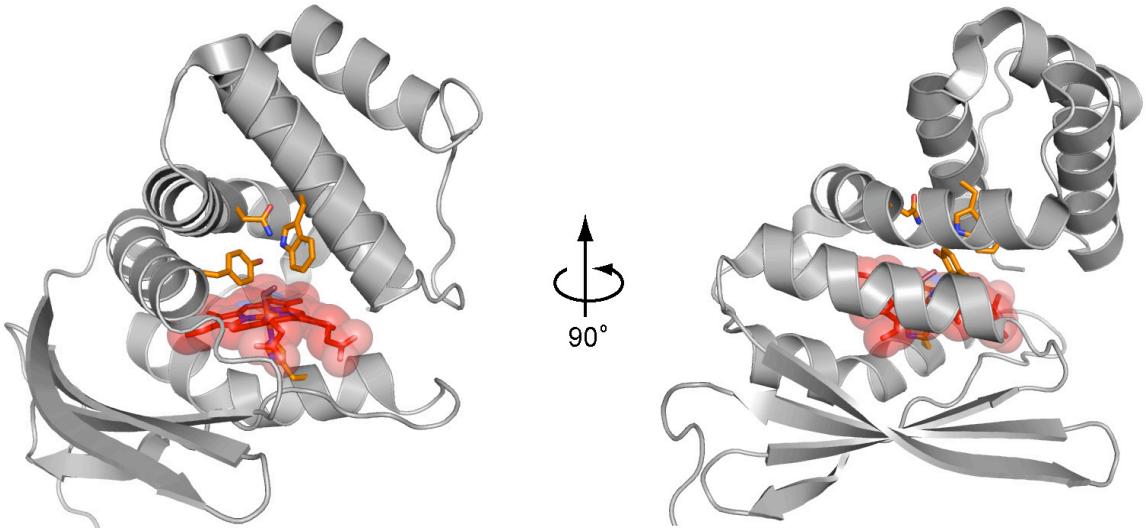

Figure 1.3. Crystal Structure of *Tt* H-NOX. Shown is molecule A (monoclinic PDB ID: 1U55). The heme is shown in ball and stick and spherical representation (red). The distal hydrogen bonding residues Trp-9, Asn-74, and Tyr-140 are shown in orange. The N-terminal domain is mostly α-helical, whereas the C-terminus is predominately β-sheet.

Heme Distortion in *Tt* H-NOX

One of the most striking features of the *Tt* H-NOX structure is the highly distorted heme prosthetic group. The rmsd from planarity for the heme cofactor was as high as 0.46 Å. Normal-coordinate analysis, which describes the type of porphyrin distortion, shows that the major contributions to heme deformation are ruffling and saddling.[19] Solution resonance Raman data contain out-of-plane modes that are consistent with the crystal structures.[9]

In the monoclinic crystal form (PDB ID: 1U55), the heme was trapped in two different conformations. Interestingly, a shift at the N-terminus was associated with flattening of the heme (Figure 1.4). It was postulated that the heme/N-terminus coupling was part of a signaling mechanism in H-NOX due to conserved elements involved in the movement.[19] For example, the rotation of the N-terminus is about a conserved glycine pivot point between α–helices D and G. Ile-5, Pro-115, and Leu-144 are also highly conserved in the H-NOX family and are important for the maintenance of heme distortion.

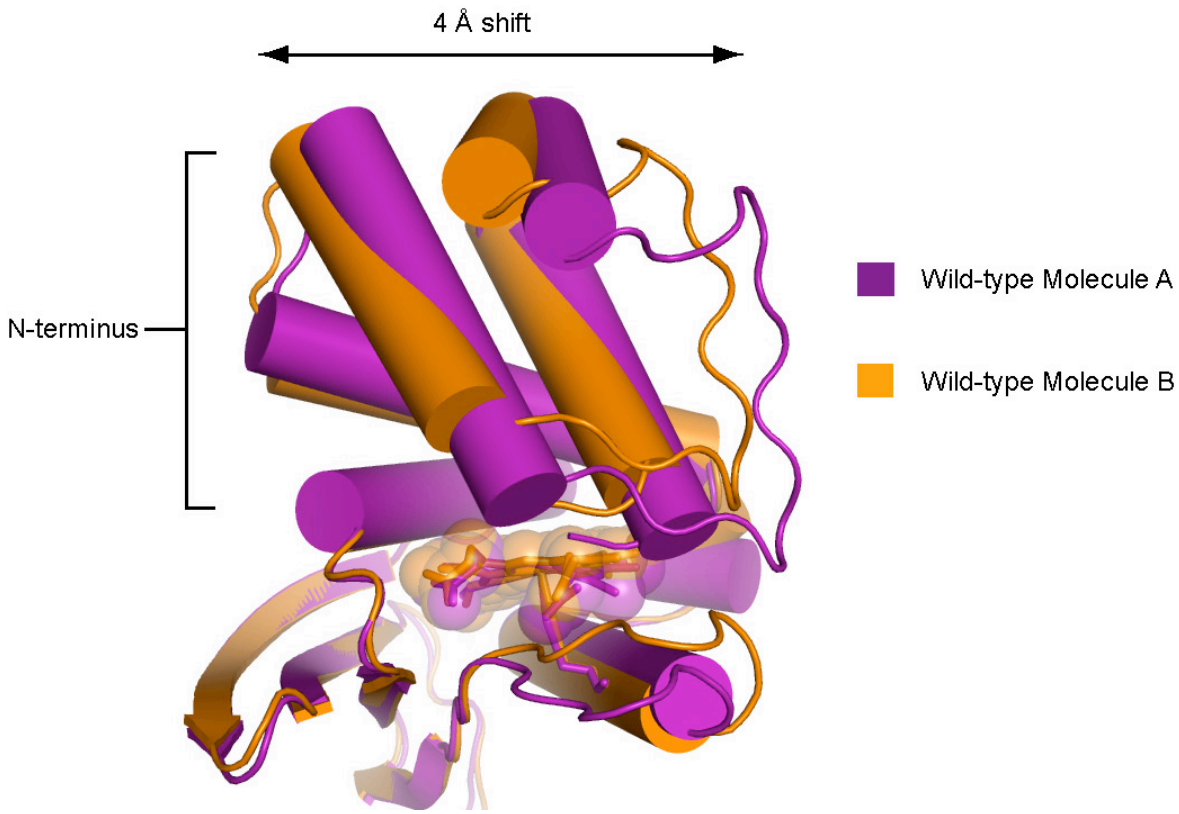

Figure 1.4. Structural changes associated with heme distortion. Shown are wild-type molecules A and B (PDB ID 1U55) in purple and orange, respectively. A shift of the N-terminus is associated with heme flattening. Conserved residues are involved in the conformational change and maintenance of heme distortion, which suggests that the heme/protein conformation coupling is part of a signal transduction mechanism.

Significance of Heme Distortion in Biology

Free heme in solution is planar due to its aromatic and highly conjugated character. It is clear from high resolution crystal structures and spectroscopy that hemes are not planar when bound to proteins.[23] Not only are hemes bent when bound to protein scaffolds, but the types of distortions are conserved within the same class of hemoproteins.[24] The conservation of heme distortion in hemoproteins suggest that distortion is important for protein function. This is evident from classical studies with globins and the importance of heme doming and cooperative mechanism of oxygen binding.[25]

The degree of heme distortion in *Tt* H-NOX is unprecedented. Figure 1.5 shows a comparison of the heme of oxy-myoglobin, which has a very planar heme, with H-NOX and other distorted hemes. Deviations over 2 Å above and below the plane of the heme of oxy-myoglobin are observed in *Tt* H-NOX. Bending the porphyrin comes at an energetic cost,[26]

which further alludes to heme distortion is important for function. This is especially pronounced in *Tt* H-NOX and its high degree of heme distortion.

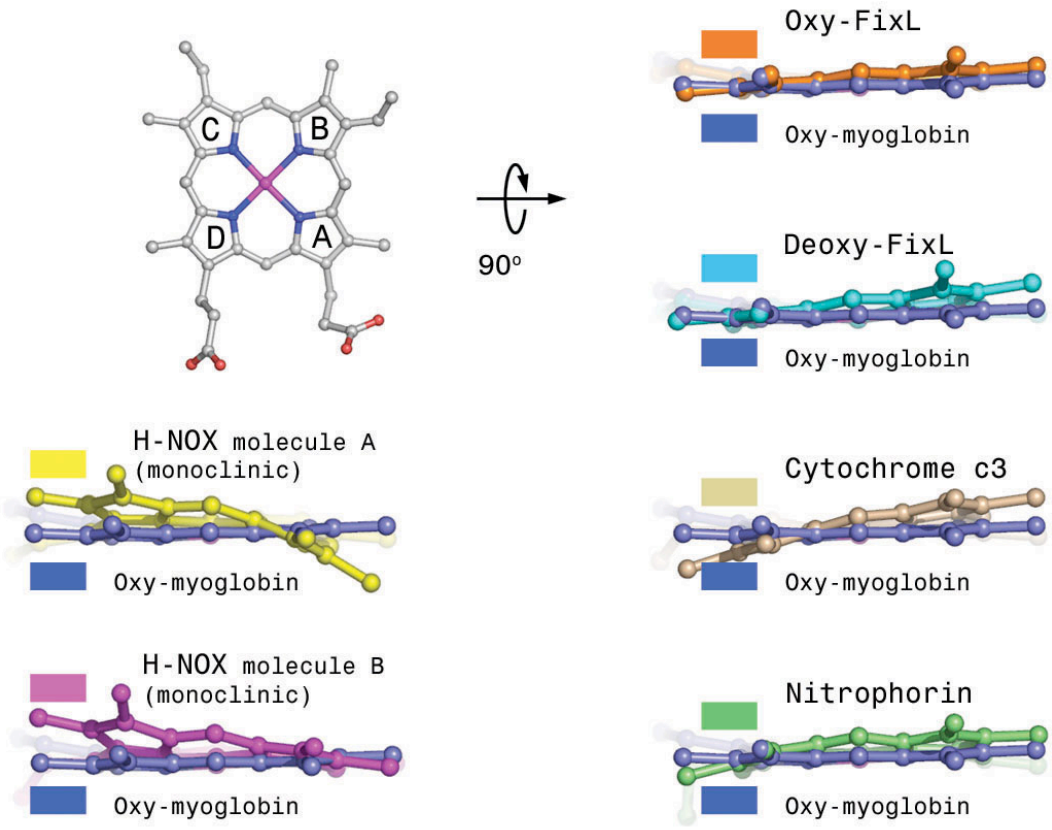

Figure 1.5. Comparison of *Tt* H-NOX heme with other distorted hemes. Pyrrole groups labeled A-D. Ball-and-stick representation of oxy-myoglobin heme (blue) compared with *Tt* H-NOX and other distorted hemes. This figure was obtain from Pellicena *et al.*,[19] National Academy of Sciences.

Thesis

My thesis is divided into three interrelated parts: 1. Probing the role of heme distortion in H-NOX proteins; 2. Using *Tt* H-NOX as a protein scaffold to fine-tune the reduction potential of a heme; and 3. Biochemical and structural characterization of H-NOX proteins.

Chapter 2 covers the investigation of the significance of heme distortion in the H-NOX family of proteins. To understand the role of heme distortion I designed a planar mutant of *Tt* H-NOX by mutating a conserved residue in the heme pocket. The crystal structure revealed a heme/protein conformation coupling similar to that seen in the wild-type structure. Flattening the heme significantly lowered the reduction potential of the heme and increased its affinity for oxygen. These studies showed that heme distortion is an important determinant for the structural and biochemical properties in H-NOX proteins.

With the knowledge gained from my initial studies on probing heme distortion, I propose using *Tt* H-NOX as a protein scaffold to fine-tune the reduction potential of a heme in Chapter 3. *Tt* H-NOX is an ideal candidate for engineering, since its expression levels are high and is thermostable. The approach is to trap distinct degrees of heme distortion by rationally engineering the protein scaffold of *Tt* H-NOX without significantly altering the heme environment (i.e. ligation state, hydrophobicity, etc.). The results from this study not only give valuable insight into heme chemistry, but provides a new tool to modulate the chemical properties of a heme cofactor. Further rational design of this construct to increase the reduction potential range will likely change the functionality of the protein and may potentially be used for broader applications.

Chapters 4 and 5 focus on the structural biology and molecular mechanisms of activation in H-NOX proteins. Specifically, the His-102 is completely conserved in all H-NOX proteins and is the residue that ligates the heme cofactor. This bond is severed upon activation in NO-binding H-NOX proteins. I solved a high resolution crystal structure of a mutant that mimics cleavage of the Fe-His bond. Key insights on the atomic details of the molecular mechanism of activation iare discussed. In chapter 5, I solved a crystal structure of a 5-coordinate unligated complex of *Tt* H-NOX. This was achieved by substituting the heme with a Zn-porphyrin that is closed shell and does not bind oxygen. The molecular details of the response to oxygen in H-NOX are presented.

Response to NO is better characterized than response to oxygen in H-NOX proteins. Tt H-NOX is the N-terminal domain of the membrane protein Tar4. In chapter 6, I present preliminary results on the biochemical characterization of the Tar4 protein. The objective is to reconstitute activity of Tar4, biochemically characterize activity, and develop an assay in response to ligand binding. Initial activity reconstitution experiments and quantitative analysis are presented along with future objectives and proposed experiments.

Chapter 2: Probing the Role of Heme Distortion in H-NOX Protein Family

Background

The very broad range of chemistry carried out by hemoproteins has attracted a vast amount of attention for many years. Representative examples include oxygen-transporting proteins, like the globins, and potent catalysts involving high-valent iron-oxo complexes, such as the cytochrome P-450s. There are a number of factors that direct and control the type of chemistry carried out by this ubiquitous class of proteins. The coordination environment provided by the protein, for example, plays a significant role in dictating both chemistry and function. The globins have evolved to stabilize the unligated Fe(II) oxidation state and the Fe(II)–O_2 complex using a proximal histidine ligand. In contrast, the thiol-ligated cytochrome P450s have a stable Fe(III) oxidation state; however, when reduced to Fe(II), the iron binds $O_2$and then generates a high-valent iron-oxo complex (formally the Fe(V) oxidation state). This potent oxidant is competent for hydroxylation chemistry of unactivated C–H bonds.

The unique and tunable chemical properties of the heme prosthetic group account for the wide range of functions observed within the hemoprotein family. The tetrapyrrole moiety of the heme is aromatic, and as such, hemes in isolation are planar. However, when protein-bound, the heme deviates significantly from planarity.[23,27-30] Although the types of heme distortions found in hemoproteins are energetically unfavorable[26], they are conserved in homologous proteins from different organisms[24], suggesting that heme distortion is important for function. Indeed, out-of-plane heme distortions have been shown to influence the biochemical properties of both noncovalent *b*-type cytochromes, such as the globins, where the heme is bound to the protein through coordination to the iron atom of an amino acid side chain, as well as the covalent *c*-type cytochromes, where a porphyrin vinyl group is attached to a protein cysteine residue by a thiol-ether linkage. For example, heme distortion affects the reduction potential[29,31,32], as well as ligand binding[28,33,34] and spectroscopic characteristics, of cytochrome *c* and model porphyrins.[35,36] Heme distortion also influences the mechanism of the "on/off" state in heme sensor proteins, such as FixL[37] and the nitrophorins[34], both *b*-type heme proteins.

Heme distortion and its functional outcomes are complicated. Past work has explored the environment within the pocket and the residues surrounding the bound heme; however, the role of distortion has been experimentally difficult to approach. Fortunately, the highly distorted heme in the Heme Nitric oxide/OXygen binding (H-NOX) domain from *Thermoanaerobacter tencongenesis* (*Tt* H-NOX) now provides a direct opportunity to address the importance and biochemical properties of heme nonplanarity.

The crystal structure of *Tt* H-NOX contains the most distorted heme observed to date.[19] In eukaryotes, H-NOX domains are found as a domain within soluble guanylate cyclase (sGC) as the receptor for nitric oxide (NO) in signaling during vasodilation and neurotransmission.[7] In prokaryotes, H-NOX proteins appear to fall into one of two classes. One type is a stand-

alone protein most often found in a predicted operon with a histidine kinase and less frequently with GGDEF-diguanylate cyclase domain. The other class is fused to methyl-accepting chemotaxis domains in the same open reading frame.[8,9,18] Homology to sGC as well as genomic placement suggests that H-NOX domains in prokaryotes are likely to serve as sensors for gases such as O_2 and NO. Recent results with the H-NOX from the facultative aerobe, *Shewanella oneidensis*, are consistent with this hypothesis.[18]

The out-of-plane heme distortions found in *Tt* H-NOX show large deviations (over 2 Å) from planarity. This distortion appears to be caused by van der Waals interactions in the heme cavity, with residue Pro115 making the largest contribution (Figure 2.1a). Pro115 is within van der Waals contact with pyrrole-D of the heme, causing the pyrrole to shift out of plane, generating a large kink in the heme propionate group. Multiple sequence alignments show that Pro115 is invariant among all H-NOX proteins, suggesting that heme distortion is conserved across the entire family. This idea has recently been substantiated as heme distortion is also observed in the crystal structures of *Nostoc* cyanobacteria H-NOX (*Ns* H-NOX).[38] Importantly, the same *Tt* H-NOX proline/heme interaction is maintained in *Ns* H-NOX, supporting the idea that heme distortion is universal to all H-NOX proteins.

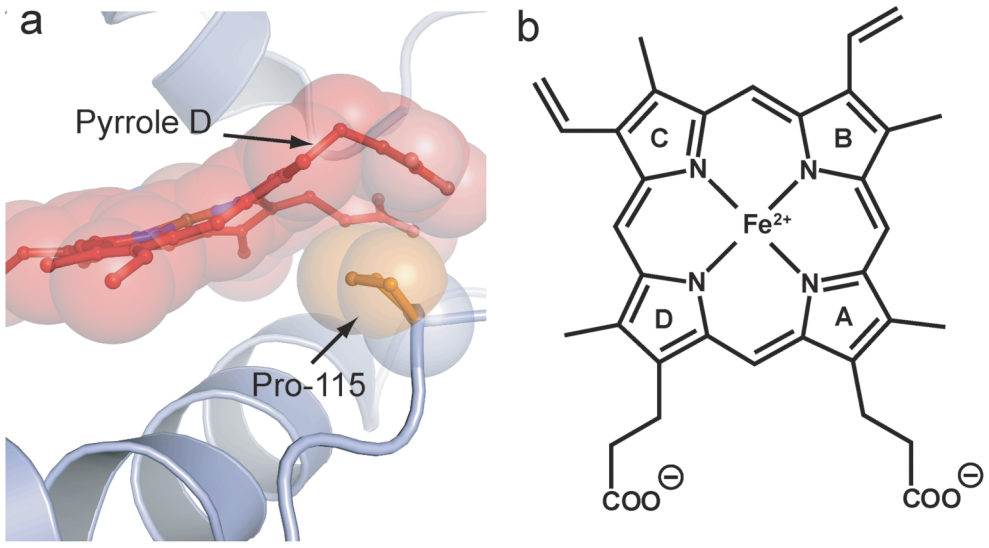

Figure 2.1. Heme distortion in wild-type *Tt* H-NOX. a) Ball-and-stick and space filling model of Pro115 and the surrounding heme environment of wild-type *Tt* H-NOX.[19] The invariant Pro115 (orange) makes the largest contribution to heme (red) distortion in *Tt* H-NOX. Pro115 pushes up against pyrrole D, which causes a pronounced kink in the connected propionate group. Out-of-plane distortions of up to 2 Å are observed in *Tt* H-NOX. b) Heme prosthetic group with pyrrole groups A–D labeled. Figure 2.1 was obtained from Olea *et al*.[39], The American Chemical Society.

The *Tt* H-NOX crystal structure contains two molecules in the unit cell, and one heme (molecule B) is slightly flattened compared to the other (molecule A). The degree of heme distortion is coupled to an N-terminal rotation in the wild-type structure.[19] In this work, to directly investigate heme flattening, Pro115 has been mutated to an alanine in *Tt* H-NOX, a mutation that should allow the heme to become less distorted and, if successful, will allow for the determination of the effects of distortion on both structure and properties. Results obtained show that the heme in P115A is significantly flattened. Additionally, the mutation increases the affinity for oxygen and, in contrast to earlier studies with other hemoproteins[33,40], decreases the reduction potential of the heme. Finally, a flatter heme in this mutant is correlated to a protein conformational change at the N-terminus where shifts of over 4.9 Å are observed.

Materials and Methods

Expression of P115A Mutant of *Tt* H-NOX in *E. coli*. Mutagenesis was carried out using the QuikChange protocol from Stratagene. Cell culture procedures and purification of P115A for kinetics were carried out as previously described.[9] Cell culture and expression procedures for P115A crystallization and redox potentiometry were carried out as described above with the exception that the growth media was Terrific Broth.

Purification of P115A for Crystallization. Cell lysis and thermal treatment were carried out as previously described.[9] The supernatant after thermal treatment was concentrated to 10 mL using a Vivaspin concentrator (Sartorius, 10 kDa) and loaded onto a Superdex 200 HiLoad 26/60 gel filtration column (Pharmacia) that was equilibrated with buffer A (50 mM TEA, pH 7.5, 50 mM NaCl, and 5% glycerol) at a flow rate of 0.5 mL min^{-1}. Fractions containing P115A were pooled on the basis of the intensity of the red/brown color and applied to a POROS HQ 7.9 mL (1 × 10 cm, 10 μm) anion-exchange column (Applied Biosystems) that had been equilibrated with buffer A. The flow rate was 10 mL min^{-1}, and the flow-through was collected. Aliquots (2 mL) of P115A were then loaded onto a Superdex 75 HiLoad 26/60 gel filtration column (Pharmacia) that was equilibrated with buffer A at a flow rate of 0.5 mL min^{-1}. P115A was isolated as the Fe(II)–O_2 complex[9] and stored at –80 °C.

Crystallization of Tt P115A. Samples of P115A were equilibrated with 20 mM TEA (pH 7.5) and concentrated to 30 mg mL^{-1}. Crystals were grown by hanging drop vapor diffusion by mixing 1 μL of the protein solution with 1 μL of the reservoir solution and equilibrating against a 750 μL reservoir of 0.1 M NaSCN, 0.1 M Tris (pH 9.1), 0.2 M $(NH_4)_2(SO_4)$, and 18% (w/v) PEG 8000 at 16 °C. Crystals began to appear within 24 h. Cryoprotection was achieved by transferring the crystals stepwise into mother liquor solutions containing 10% and 15% glycerol and ending with 20% glycerol and 5% xylitol. Crystals of P115A were obtained in the *C*2 space group, flash frozen in liquid propane, and stored in liquid nitrogen.

X-ray Data Collection, Phasing and Refinement. X-ray data were collected by using synchrotron radiation at beamline 8.2.1 at the Advanced Light Source, Lawrence Berkeley National Laboratory. Diffraction images were collected at 100 K with 10 s exposure time and 1° oscillations per frame. Data were processed with the HKL2000 suite.[41] Molecular

replacement was carried out with Phaser[42] using wild-type H-NOX (PDB ID 1U55) as a search model. Model building was carried out by using the programs O[43] and Coot.[44] Refinement was carried out by using CNS[45] and Phenix[46] with TLS refinement parameters incorporated. The final model includes four P115A molecules in the asymmetric unit. The structure of P115A was refined to a final R_{work} of 20.5% (R_{free} = 25.2%) at 2.12 Å.

Kinetics. The on-rate of O_2 binding to heme and dissociation of O_2 from heme were measured as previously described.[12]

Redox Potentiometry. Potentiometric titrations were performed as previously described.[47] The change in the Fe oxidation state in *Tt* H-NOX was monitored by the absorbance change at α/β region maximum (~557 nm). For P115A the oxidation state change was measured by the difference of absorbance of the α/β maximum of the oxidized and the α/β minimum of the reduced oxidation state spectra.

Results and Discussion

Design of a Planar Heme in *Tt* H-NOX. Guided by visual inspection of the structure of wild-type *Tt* H-NOX as well as energy minimizations[19] that predict Pro115 to contribute significantly to heme distortion, the P115A mutant was made. P115A was designed to replace the steric bulk of the cyclic three-carbon chain with a less bulky methyl group.

Structure Determination and Analysis of P115A. The crystal structure of the P115A *Tt* H-NOX domain was solved by molecular replacement and refined to 2.12 Å resolution with a final R_{work} value of 20.5% and an R_{free} value of 25.2% (Figure 2.2). A total of four Fe(II)–O_2 P115A molecules (molecules A–D) were built in a monoclinic asymmetric unit cell. Crystallographic data and refinement statistics are summarized in Table 2.1.

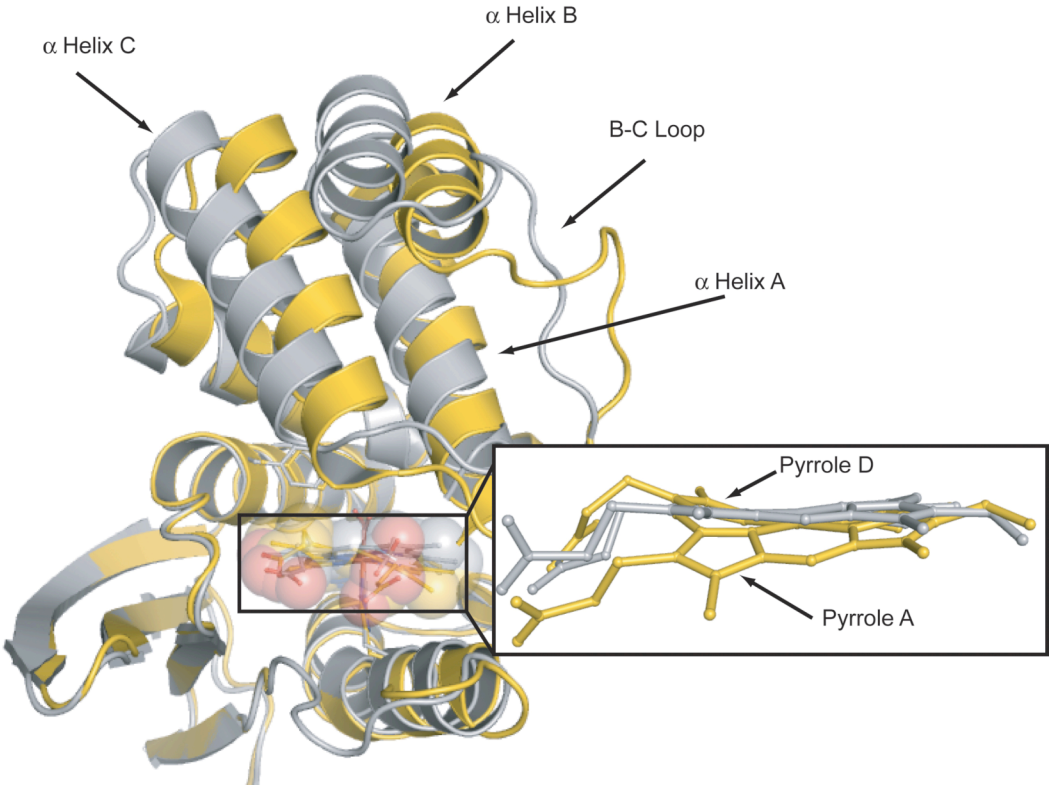

Figure 2.2 Structural comparison of P115A with wild-type *Tt* H-NOX. The heme in P115A (silver) is flatter than wild-type (gold). Significant translations are observed in the N-terminal region of the heme-flattened P115A crystal structure. Shown are molecule A from the monoclinic crystal structure of *Tt* wild-type H-NOX and molecule D from the P115A crystal structure. Figure 2.2 was obtained from Olea *et al*.[39], The American Chemical Society.

TABLE 2.1. Statistics of crystallographic data collection and refinement statistics

Data Collection	
Space group	*C2*
Cell dimensions	
a, *b*, *c* (Å)	116.3, 124.7, 83.6
α, β, γ (°)	126.6
Resolution (Å)	50-2.12 (2.20- 2.12)
R_{merge} (%)	5.5 (45.5)
I / σ[a]	20.9 (2.7)
Completeness[a] (%)	99.2 (99.0)
Redundancy	4.3 (3.6)
Refinement	
No. of reflections	53135
R_{work} / R_{free}[b] (%)	20.5/25.2
No. atoms	

Protein	6577
Heme	172
O_2 Molecules	4
Water molecules	176
B-factors	
Overall	49
Rms deviation	
Bond lengths (Å)	0.008
Bond angles (°)	0.898

[a] The values in parentheses relate to highest-resolution shells.
[b] R_{free} is calculated for a randomly chosen 5% of reflections.

Root mean square (rms) deviation from planarity, normal-coordinate analysis, and interpyrrole angles were calculated for all hemes in P115A (Appendix Tables A1 and A2). The N-terminal and overall rms deviation from wild-type *Tt* H-NOX were calculated for P115A (Appendix Table A3). Matrix plots based on the differences in α-carbon distances were calculated with the program DDMP (Center for Structural Biology at Yale University, New Haven, CT and Appendix Figures A1a–d). These plots show that the C-terminal region overlays well with wild-type, and consequently residues 1−83 were used to calculate N-terminal rms deviation. The iron-histidine tilt was calculated using the least-squares plane of the four pyrrole nitrogens in the heme (the other atoms in the macrocycle were excluded because of the high degree of distortion) and the five imidazole ring atoms of His102 using MOLEMAN2 (22).

Heme Distortion in P115A versus Wild-Type. All four molecules in the unit cell have hemes flatter than that of wild-type *Tt* H-NOX. Molecules C and D (Figure 2.3) show the most significant change from wild-type (Appendix Tables A1, A2 and A3). However, the heme atoms in molecule C have relatively high B-factor values that range from 49 to 78 $Å^2$. Therefore, further analysis is primarily focused on molecule D, which can be analyzed with higher certainty with B-factor values that range from 39 to 61 $Å^2$. Molecule A of the wild-type *Tt* H-NOX is used for comparison because it has the highest degree of heme distortion.

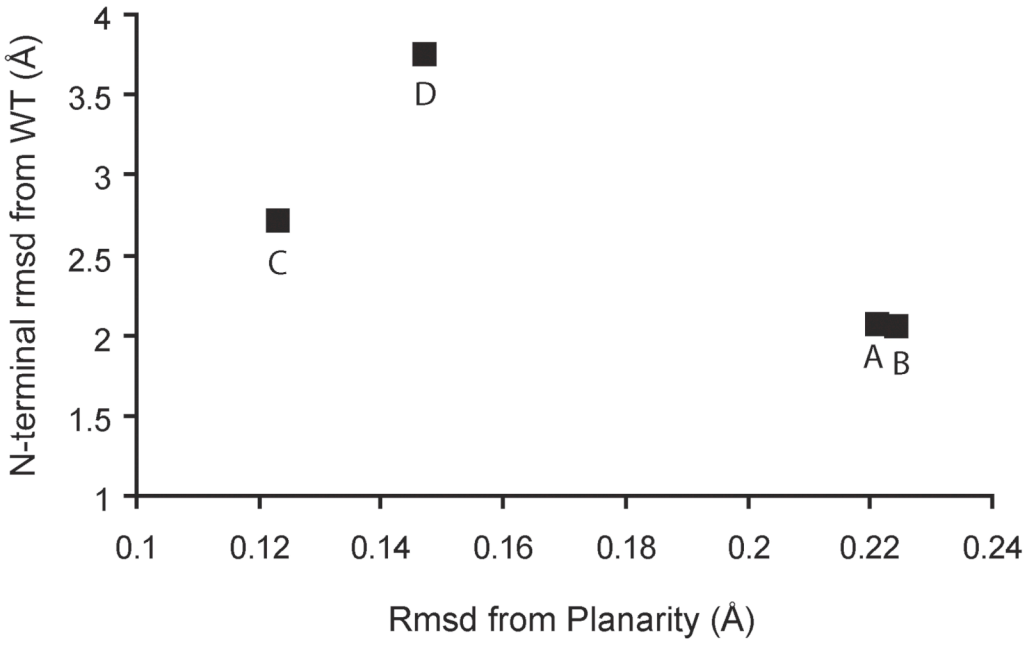

Figure 2.3. N-Terminal movement from wild-type *Tt* H-NOX (WT) *versus* heme distortion in P115A. The N-terminal (residues 1–83) rms deviation (Å) was calculated and plotted *versus* rms deviation (Å) from planarity for each of the four molecules in the asymmetric unit cell (A–D). Wild-type molecule A in the monoclinic space group was used for analysis. Figure 2.3 was obtained from Olea *et al*.[39], The American Chemical Society.

A comparison of P115A molecule D and wild-type *Tt* H-NOX molecule A is shown in Figure 2.2. The rms deviation from planarity in P115A has decreased significantly, approximately 3-fold compared to wild-type. Specifically, the rms deviation from planarity is 0.147 Å in P115A compared to 0.460 Å in the wild-type *Tt* H-NOX. The decrease in rms deviation from planarity in P115A from the most distorted heme in wild-type *Tt* H-NOX is approximately 3-fold.

Appendix Table A1 shows the major contributions to heme distortion in P115A and wild-type *Tt* H-NOX as calculated by normal-coordinate structural analysis.[24,48] The major contributors to heme distortion in wild-type *Tt* H-NOX are saddling and ruffling. In all four P115A molecules (A−D), the degree of both saddling and ruffling decreases with respect to all molecules of wild-type. For example, saddling and ruffling in P115A molecule D are 0.066 Å and −0.517 Å, respectively, while in wild-type molecule A they are −1.069 Å and −1.105 Å. The angles between the planes of the pyrrole rings within the heme in P115A decrease from that in the wild-type *Tt* H-NOX (Appendix Table A2). The pyrrole angles in molecule D range from 0° to 15°, whereas in the wild-type *Tt* H-NOX they range from 10° to 33°.

Overall, the P115A crystal structure shows that removal of the bulky and conformationally constrained proline leads to a general flattening of the heme, as demonstrated by the decrease in all interpyrrole angles as well as decreased saddling and ruffling displacements, described

above. This occurs because the pyrrole D ring and the associated propionate side chain move back into the porphyrin plane, resulting in more space in the heme pocket and allowing the heme to adopt a lower energy conformation. Therefore, the P115A structure illustrates the importance of Pro115 in maintaining the unusual deviation from planarity of the heme in *Tt* H-NOX. Because it is invariant across the entire H-NOX family, these results suggest that this residue maintains heme deformation throughout the family.

Heme Flattening Is Associated with a Movement of the N-Terminus in H-NOX. It was postulated that the degree of heme distortion would be coupled to the conformation of the wild-type structure. Difference distance matrix plots show that the C-terminus in P115A aligns well with wild-type (Appendix Figures A1a-d). A plot of heme distortion *versus* N-terminal movement in P115A (Figure 2.3) shows a clear trend between heme distortion and N-terminal movement. A significant conformational change is observed in P115A, especially in molecule D, as compared with wild-type *Tt* H-NOX molecule A (Figure 2.2 and Appendix Table A3). The N-terminal rms deviation between wild-type molecule A and P115A molecule D is 3.76 Å.

Upon heme flattening, the tight network of van der Waals interactions in the heme pocket is lost. In particular, residues Ile5 and Met1, both on α-helix A, which are in direct contact with heme pyrrole A and the attached propionate side chain, respectively, undergo significant movement upon heme flattening. Figure 2.4 shows the P115A heme methyl group connected to pyrrole A moving into the plane, causing Ile5, which is part of α-helix A, to shift away from the heme. Also upon heme flattening, the propionate side chain connected to pyrrole A pushes Met1 away from the heme and the C-terminal region.

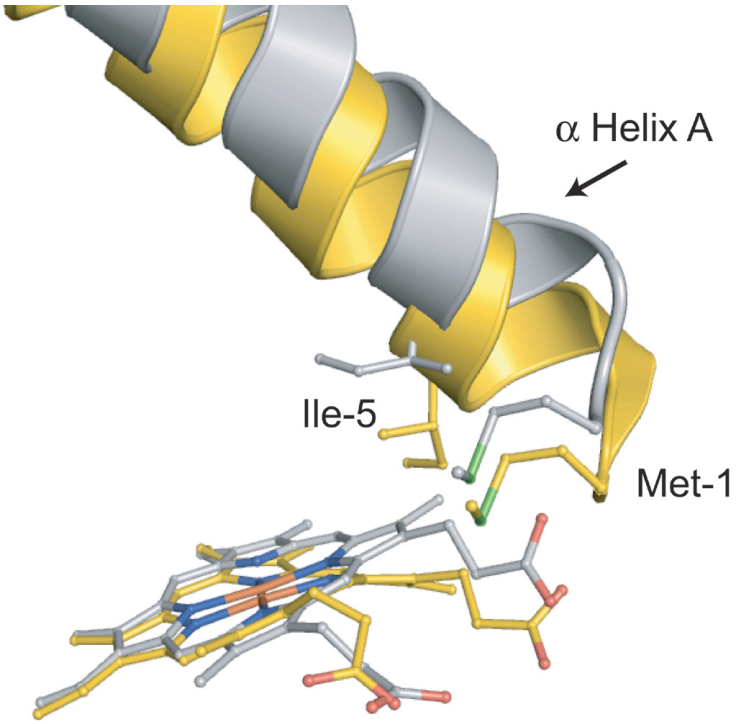

Figure 2.4. The effect of heme flattening on the N-terminal domain. Shown is a comparison of P115A molecule D (silver) and wild-type monoclinic *Tt* H-NOX molecule A (gold) heme/N-terminal interface. The planar heme makes new contacts with Met1 and Ile5 of α-helix A, which shifts the helix away from the C-terminal domain. Shifting of α-helix A, along with the rest of the N-terminal region, causes shifts over 4.9 Å. Figure 2.4 was obtained from Olea *et al*.[39], The American Chemical Society.

The major conformational shifts observed in P115A molecule D are localized to N-terminal α-helices A–D and the loop in between helices B and C (residues 32–45 or loop B–C) (Figure 2.2). As described in more detail above, α-helix A (residues 1−17) moves in conjunction with pyrrole A shifting back into plane. α-Helix C (residues 45−59) and loop B−C move along with α-helix A away from the heme and the C-terminal region. The most significant change observed in P115A can be seen in α-helix B (residues 19−29), which makes direct contact with helices A and C (Figure 2.2). Shifts over 4.9 Å in α-helix B are observed.

The conformation of the protein is intimately tied to the heme conformation. The large deviation in heme conformation from that of wild-type is caused by the loss of the tight network of van der Waals interactions in the heme pocket. Loss of local contacts with the heme due to heme flattening, especially at the distal pocket, results in N-terminal shifts that significantly alter the conformation of the protein. Clearly, the heme and the local protein environment are working in concert to maintain a particular conformational state in *Tt* H-NOX.

The molecular surface changes that occur upon heme flattening is a likely mechanism involved in signal transduction in this H-NOX domain. The *Tt* H-NOX domain is a member of the Tar4 family of receptors and is fused to a predicted methyl-accepting chemotaxis protein (MCP) with two predicted membrane spanning regions between these two domains. A model based on these domains places the H-NOX domain on the same side of the membrane as the MCP, suggesting that intermolecular contacts between the sensor H-NOX and the MCP are involved in the signal transduction mechanism. Thus, ligand-induced H-NOX conformational changes may control methylation of the MCP. Whether heme flattening contributes to the control of methylation has yet to be evaluated.

Higher Affinity for O_2 in P115A Is Caused by Proximal Effects at the Heme. It is expected that changes in heme structure will have influence on ligand binding affinity and other heme chemical and physical properties. To evaluate the effects of heme flattening on ligand binding of *Tt* H-NOX, O_2 binding kinetics were measured and compared to those of the wild-type H-NOX. The association and dissociation rates were measured as previously described for the wild-type *Tt* H-NOX (Appendix Table A4).[12] The dissociation rate of P115A was 0.22 ± 0.01 s^{-1}, compared to 1.22 ± 0.09 s^{-1} for the wild-type *Tt* H-NOX. No significant change was observed in the P115A association rate (10.4 ± 1.1 and 13.6 ± 1.0 μM^{-1} s^{-1} for P115A and wild-type, respectively), resulting in a protein with a higher affinity for O_2 (K_D is 21.2 ± 2.1 and 89.7 ± 6.2 nM for P115A and wild-type, respectively). Factors

such as the distal pocket H-bonding network in *Tt* H-NOX[12] and the strength of the Fe-His bonds are known to contribute to higher affinity for oxygen in hemoproteins.[49,50] Surprisingly, all Fe-His bond lengths and distal hydrogen bonds to O_2 in P115A are within error to those of the wild-type structure (data not shown), therefore some other factor must play a role in O_2 affinity.

The Fe-histidine tilt, which has also been shown to affect ligand affinity in hemoproteins[51], decreased in P115A compared to wild-type (Appendix Table A1 and Figure 2.5). Wild-type *Tt*H-NOX molecule A has a tilt of 78°, whereas the tilt in P115A molecule D is nearly perpendicular with a tilt of 87° (Figure 2.5). It is likely that flattening the heme in P115A allows for optimized bond overlap between the proximal histidine and iron, thus creating a stronger proximal bond that stabilizes the Fe(II)−O_2 complex and may explain the slower off-rate of O_2 in P115A.

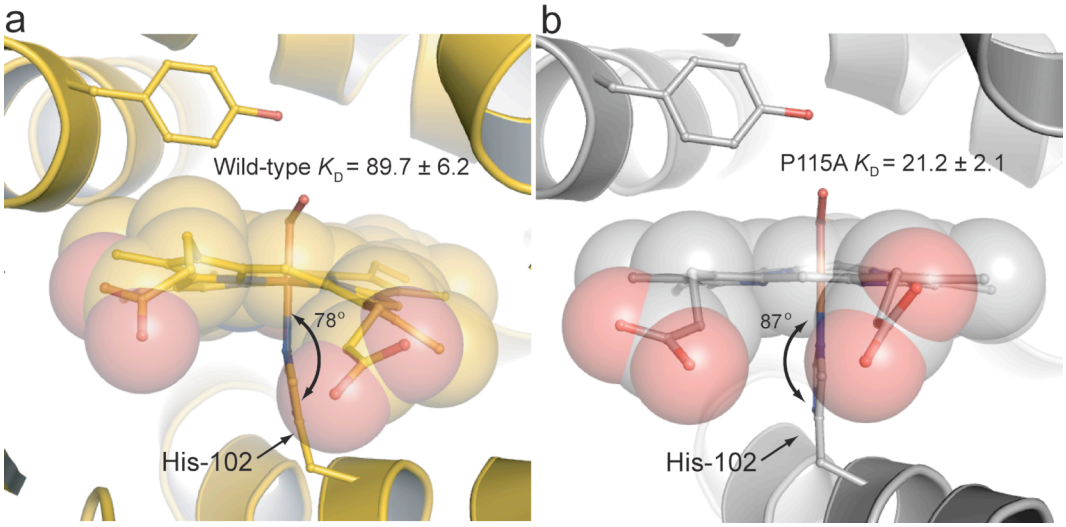

Figure 2.5. Comparison of the iron–histidine bond geometry. Shown are the iron–histidine tilts of a) wild-type *Tt* H-NOX (gold) and b) P115A (silver). The least-squares plane of the heme was calculated using the four pyrrole nitrogens of the heme (other atoms were excluded because of the high degree of distortion) and the five imidazole ring atoms of His102 using MOLEMAN2.[52] Wild-type has a tilt of 78°, whereas P115A has a tilt of 87°. Figure 2.5 was obtained from Olea *et al*.[39], The American Chemical Society.

We have speculated that *Tt* H-NOX serves as an oxygen sensor for the obligate anaerobe *T. tengcongensis* based on the fact that O_2 binding to this H-NOX is very tight (K_D = 90 nM). The fold of *Tt* H-NOX may tune the affinity for oxygen by distorting the heme so that the K_D is set for the appropriate physiological response. The situation may not be this simple, however. Taylor and colleagues[53] showed that *Desulfovibrio vulgaris* Hildenborough, a sulfate-reducing bacterium thought to be an obligate anaerobe, actually preferred an oxygen concentration of 0.02–0.04% (0.24–0.48 μM). This O_2 concentration was also shown to

support growth. Hence, sensors for O_2 are likely tuned to respond to changing environmental conditions and complex physiological responses.

Reduction Potential Decreases in P115A. To determine whether chemical properties of the heme are sensitive to heme conformation, the reduction potential was measured for P115A and *Tt* H-NOX. P115A has a reduction potential significantly lower than that of wild-type. The reduction potentials of P115A and wild-type *Tt*H-NOX are –3.8 ± 10.2 and 167.0 ± 6.7 mV *versus* the standard hydrogen electrode (SHE) (Figure 2.6), respectively.

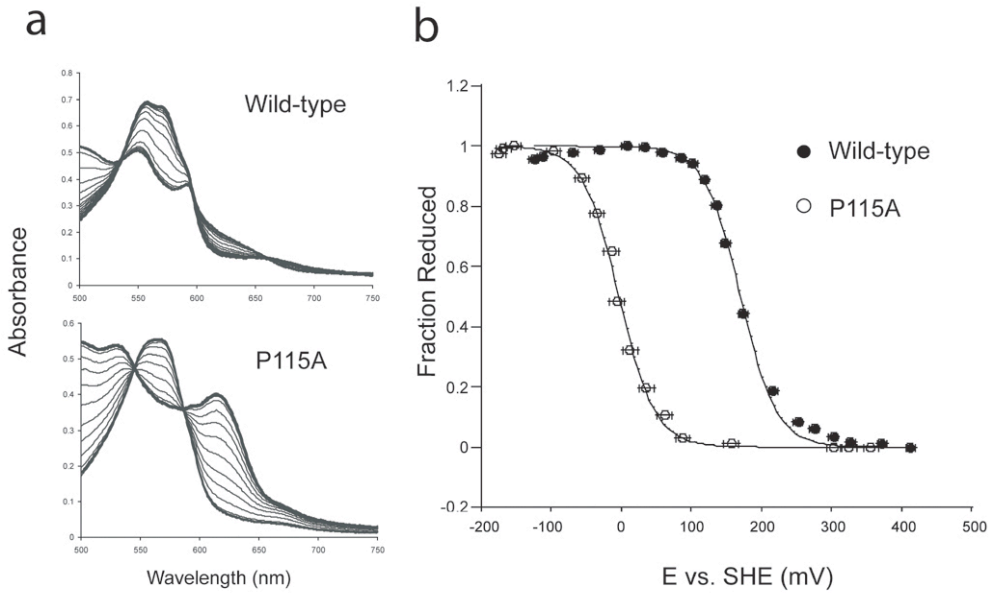

Figure 2.6. Reduction potential of wild-type *Tt* H-NOX and P115A. a) Titration spectra for wild-type *Tt* H-NOX and P115A. b) Titration curves for wild-type *Tt* H-NOX and P115A. The reduction potentials of P115A and wild-type *Tt* H-NOX were determined against the standard hydrogen electrode (SHE). The ratio of reduced Fe^{2+} to oxidized Fe^{3+} heme was measured on the basis of their α/β maximum at approximately 557 nm for wild-type. The difference in absorbance of the α/β maximum for reduced and the α/β minimum for oxidized was used to calculate the fraction reduced for P115A. The voltage against the SHE was measured for both oxidative and reductive titrations of wild-type and P115A. Error bars represent the standard error. Figure 2.6 was obtained from Olea *et al*.[39], The American Chemical Society.

Previous studies have suggested that factors such as electrostatic interactions near the heme pocket control hemoprotein reduction potentials.[54-57] In particular, it has been demonstrated that the reduction potential increases as a function of decreasing dielectric constant[58,59]; however, we cannot definitively comment on a change in the dielectric environment in P115A *versus* the wild-type protein. While the P115A mutant was designed to specifically address the role of heme distortion, the mutation could introduce other changes such as an alteration in the dielectric of the heme environment.

Implications for the Role of Heme Distortion in H-NOX Proteins. Our results show that (i) Pro115 is important for maintaining heme distortion in *Tt* H-NOX, (ii) heme distortion maintains a particular molecular oxygen K_D and a particular heme iron reduction potential, presumably at their physiologically relevant values, and (iii) heme distortion is correlated with movement in the N-terminal region of the *Tt* H-NOX. Thus, the heme and the surrounding environment work in conjunction to maintain conformation and function in *Tt* H-NOX.

As noted by Shelnutt and colleagues[23], porphyrin deformations are often conserved within functional classes of proteins, strongly supporting the idea that these deformations are important for function. Pro115 is likely to be important for the function of the H-NOX family since it is conserved in the entire class of proteins. Heme distortion in *Tt* H-NOX is essential for maintaining its structural conformation and biochemical properties. The data show that heme distortion contributes to maintaining a specific K_D for oxygen and reduction potential of the heme iron. Additionally, heme distortion is related to the conformation of *Tt* H-NOX. The heme and the surrounding environment work in concert to maintain a particular conformation and fold.

Conclusions

The influence of heme distortion on function has been a long-standing question and certainly related to the diverse chemistry exhibited by this large class of proteins. While many structural and biochemical studies over the past several decades have made note of heme distortion, a systematic approach has not appeared. The challenge is to trap the heme in different conformations under similar conditions (pH, salinity, temperature, etc.) and ligation state. The H-NOX family, for the reasons outlined above, provides the opportunity to carry out such an investigation, and the first step in this regard is reported here. As discussed, heme distortion in the nitrophorins is significant.[32,34] Walker and colleagues[33] attempted to trap a flattened heme in nitrophorin 2. They speculated that distal pocket mutations in the protein would flatten the heme and speculated further about a change in redox potential. However, very little change in heme conformation was observed between the hemes of both the wild-type protein and the mutant crystal structures (PDB codes 2A3F and 2ALL). The H-NOX results presented in this paper show a heme trapped in different conformational states generated by a single point mutation. The differences in ligand binding and redox potential correlate with the changes in heme distortion; however, our results do not agree with a previous report that shows an opposite trend in heme ruffling *versus* redox potential in cytochromes c_3.[40] Clearly, the redox potential and ligand binding will depend on multiple factors including the heme environment, ligands to the iron and covalent *versus* noncovalent heme, as well as the degree of heme distortion. The large movement of the N-terminal region of the protein was unexpected and provides a clear example of protein conformation linked to the heme cofactor. The movement was presaged by what we previously observed in molecules A and B in our first structure[19]; however, it was uncertain whether the heme conformation and N-terminal shift were an outcome of the crystallization. Our results here unambiguously show the importance of heme conformation in protein structure and chemistry.

Chapter 3: Modulating the Redox Potential of a Heme Using an H-NOX Domain

Redox reactions are fundamental transformations in biochemistry and metals and metallo reactions centers are essential in these reactions.[60] Bioinorganic model complexes have been designed that are tailor-made to span a broad range of redox potentials and have found broad applications.[61-65] For example, the reduction potential at the copper center in electron transfer proteins has been modulated to design efficient and renewable energy devices.[63] Redox active proteins have a broad range of potentials that are utilized in many aspects of cellular function including photosynthesis, oxidative phosphorylation, and signal transduction. Nature has exploited many different protein scaffolds in order to achieve a wide range of functionality from only a handful of reaction centers.

Hemoproteins are a ubiquitous class of metalloproteins involved in many diverse and complex redox reactions, including electron transfer, oxygen activation, and gas transport.[66,67] Although hemoproteins employ the same heme cofactor, the individual reduction potentials can vary up to 1000 mV.[67-69] While hemoproteins have been studied for decades, the factors responsible for fine-tuning heme reduction potential remain to be fully elucidated though certainly the local environment and ligands provided by the protein play an important role. A clearer understanding of heme redox chemistry could facilitate the rational design of hemoproteins with desirable chemical properties.

Many studies have contributed greatly to our knowledge of factors that control the reduction potential of hemoporteins. In human myoglobin, it was shown that introduction of charged and polar residues in the heme environment significantly influence the reduction potential of the heme.[54,70] Subsequent studies on cytochromes and theoretical calculations demonstrated the importance of the hydrophobicity of the heme pocket and control of the reduction potential.[71-73] It has also been shown that the ligation and spin state of the heme greatly influences the redox properties of hemoproteins involved in electron transfer.[58,74,75] Synthetic peptide-based proteins have been designed to fine-tune heme reduction potentials.[76] Utilizing *de novo* four-helix bundles called protein "maquettes" the reduction potential of the heme was varied over 400 mV through change in hydrophobicity surrounding the heme.[68]

The heme cofactor is an aromatic, highly conjugated molecule, and planar when free in solution. However, it is clear from high-resolution crystal structures and spectroscopic studies that protein-bound hemes are not planar and adopt of variety of conformations[4-9] that appear to affect heme reduction potential.[23,24,39] Importantly, modes of heme distortion are conserved within the same classes of hemoproteins,[24] suggesting that heme distortion is critical for biological function.[35] Bending the porphyrin macrocycle is energetically unfavorable, which also suggests the bending the porphyrin is important for functionality.[26] To understand the effects of heme distortion on reduction potential, synthetic porphyrins have been designed over the past few decades with various degrees of heme deformation.[23] Bulky substituents have been added to the porphyrin to bend the porphyrin through steric effects.[23] Although much was learned from these studies, the addition of unnatural substituents may

influence the reduction potential solely based on their electron withdrawing or donating properties. Biological outcomes of porphyrin bending would benefit from studies using a natural protein scaffold where a heme could be engineered to bring about subtle changes in the degree of distortion while maintaining the coordination and chemical environment of the porphyrin.

In previous studies[39,77], it was shown that upon flattening of the heme in the **H**eme **N**itric oxide / **OX**ygen binding (H-NOX) protein from *T. tengcongensis* (*Tt* H-NOX), the reduction potential was significantly decreased. Optimized overlap between the pi-orbitals of the porphyrin and histidine and the d-orbitals of the iron was suggested to be a factor in the dramatic decrease in reduction potential. The rationale was that the porphyrin contributes more electron density into the iron, which make the iron more electron dense and, therefore, lowering the reduction potential. However, whether a direct correlation between the degree of distortion and reduction potential of the heme is still unclear.

The goal of this study was to generate mutants of the *Tt* H-NOX with varying degrees of heme distortion and to correlate those changes with the reduction potential of a heme cofactor. The mutants would have the same ligation state as the wildtype protein and would have minimal changes to the heme environment. The conservative mutations in the heme pocket made minimal perturbations in protein hydrophobicity and crystal structures show that hydrogen bond networks, especially with conserved residues in the heme pocket were intact. Redox potentiometry and pH titrations showed that the degree of heme distortion is directly correlated with the electronic properties of the heme iron. Our data suggest that flattening of the porphyrin leads to increased electron density on the heme iron, which leads to a decrease in reduction potential. The protein scaffolds described here can be used to not only build more protein variants, including those with different axial ligands and unnatural porphyrins, but also highlights how hemoprotein scaffolds can dramatically influence heme electronic properties by only changing porphyrin conformation.

Materials and Methods

Expression of the I5L and I5L/P115A mutants of *Tt* H-NOX in *E. coli*. Mutagenesis, cell culture, and expression procedures were carried out as previously described.[9]

Purification of the I5L and I5L/P115A mutants in *E. coli* for crystallization and potentiometry. Cell lysis and thermal treatment were carried out as described with the exception of an ultracentrifugation step after cell lysis.[9] The supernatant after thermal treatment was loaded onto a Toyopearl Q 650M anion exchange column that was equilibrated buffer A (50 mM TEA, pH 7.5, and 50 mM NaCl) at a flow rate of 1.5 mL/min. The flow-through was equilibrated over Sephadex G-25 column equilibrated in buffer B (50 mM HEPES pH 6.25). The red flow through was collected and loaded on a SP 650M cation exchange column equilibrated in buffer B at 1 mL/min. The protein was eluted off the cation exchange column applying a salt gradient of 0-40% buffer C (50 mM HEPES and 500 mM NaCl pH 6.25) at 1 mL/min in 2 mL fractions were collected. Red-colored fractions were initially pooled based on Coomassie stain and for subsequent runs based on a Soret: A_{280} ratio

above 1.6. Both I5L and I5L/P115A were isolated as the Fe(II)-O_2 complex[9], and stored at -80 °C in a final buffer of 50 mM HEPES, 200 mM NaCl, and 5% glycerol at pH 6.25.

Crystallization of the I5L mutant. Samples of I5L were equilibrated with 20 mM TEA pH 7.5 and concentrated to 25 mg/mL. Orthorhombic crystals were grown by sitting drop vapor diffusion by mixing 1 μL of protein solution with 4 μL of the reservoir solution and equilibrating against 700 μL of 0.1 M MES pH 6, 0.1 M LiCl, and 26% polyethylene glycol for two days at 16 °C. Cryoprotection was achieved by addition of mother liquor substituted with 30% glycerol in increasing glycerol amounts of 5% to a final concentration of 15% glycerol, flash frozen, and stored in liquid nitrogen.

Crystallization of the I5L/P115A mutant. Samples of I5L/P115A were equilibrated with 20 mM TEA pH 7.5 and concentrated to 30 mg/mL. Monoclinic crystals were grown by sitting drop vapor diffusion by mixing 1 μL of protein solution with 3 μL of the reservoir solution and equilibrating against 700 μL of 0.05 M MES pH 6, 0.1 M LiCl, and 22% polyethylene glycol for two days at 16 °C. Cryoprotection was achieved by addition of mother liquor substituted with 40% glycerol in increasing amounts of 5% glycerol to a final concentration of 25% glycerol, flash frozen, and stored in liquid nitrogen.

X-ray data collection, phasing, and refinement of the I5L mutant. X-ray data were collected by using synchrotron radiation at beamline 8.2.1 at the Advanced Light Source, Lawrence Berkeley National Laboratory. Diffraction images were collected at 100 K with 7 s exposure time and 1° oscillations per frame. Data were processed with the HKL2000 suite.[41] Molecular replacement was carried out with the CCP4 program
Phaser[42] using P115A H-NOX (PDB ID: 3EEE) as the search model. Model building was carried out by using the program Coot[44] and refinement was carried out using CNS and Phenix with TLS refinement parameters incorporated. The final model includes 2 I5L molecules in the asymmetric unit. The structure of I5L was refined to a final overall R_{work} and R_{free} of 21.7% and 26.0% at 2.15 Å resolution, respectively.

X-ray data collection, phasing, and refinement the I5L/P115A mutant. X-ray data were collected by using synchrotron radiation at beamline 8.2.1 at the Advanced Light Source, Lawrence Berkeley National Laboratory. Diffraction images were collected at 100 K with 5 s exposure time and 1° oscillations per frame. Data processing, phasing, model building and refinement were carried out as described above. The final model includes 2 I5L/P115A molecules in the asymmetric unit. The structure of I5L/P115A was refined to a final overall R_{work} and R_{free} of 18.9% and 23.5% at 2.04 Å resolution, respectively.

Spectrophotometric Redox Titrations of the I5L and I5L/P115A mutants. Potentiometric titrations of I5L and I5L/P115A were performed as described previously.[39]

Results and Discussion

Design of *Tt* H-NOX variants with altered heme distortion. The I5L and I5L/P115A mutations to the *Tt* H-NOX scaffold were chosen as candidates for altering the porphyrin

conformation based on previous results[39] along with energy minimizations and visual inspection of the wild-type crystal structure.[19] The I5L mutation was designed to disrupt the tight van der Waals interactions between the distal face of pyrrole A and the γ and δ carbons of I5 (Figure 1a-1b). The P115A mutation was designed to eliminate the steric bulk of P115 on the proximal side of pyrrole D (Figure 1c).[39] The overall rationale was to design the protein scaffold to distort the porphyrin with distinct degrees of distortion and study the chemical properties of each construct.

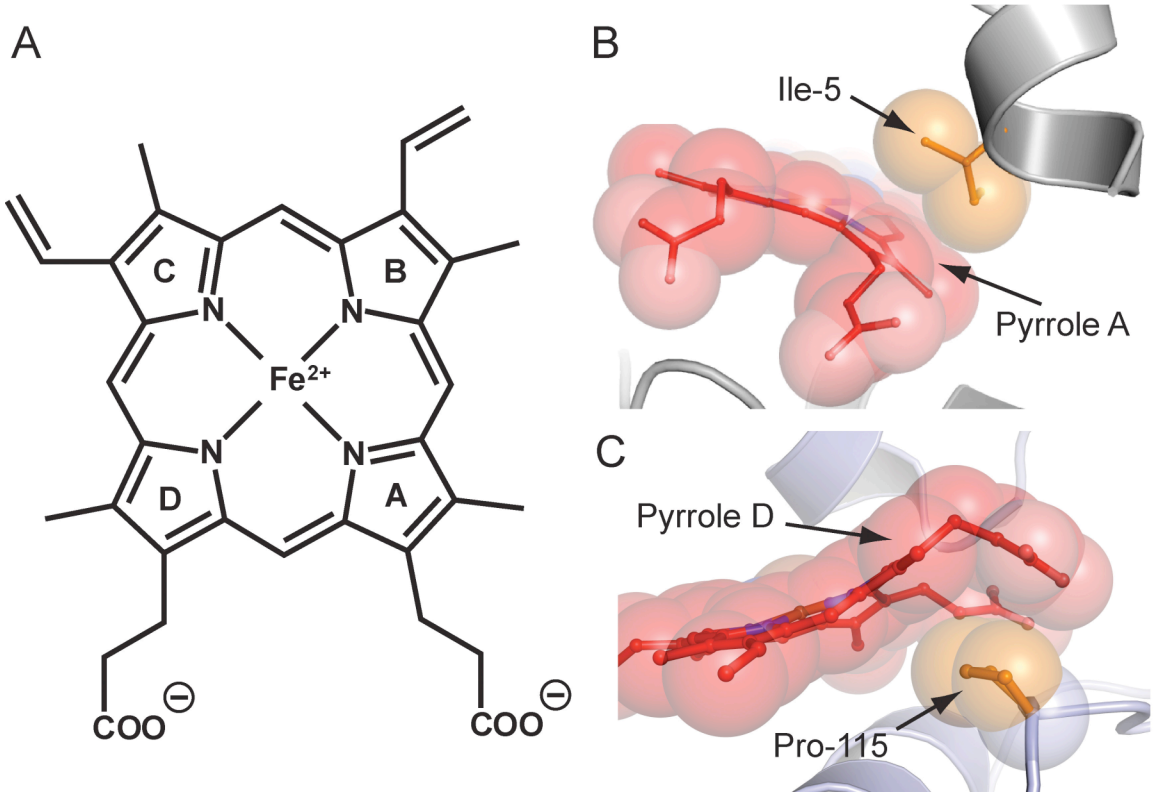

Figure 3.1. Heme Distortion in wild-type *Tt* H-NOX. A) Heme prosthetic group with pyrrole groups A-D labeled. B) Ball-and-stick and space filling model of Ile-5 and C) Pro-115 and the surrounding heme environment of wild-type *Tt* H-NOX. Ile-5 and Pro-115 push down and up against the heme, respectively, causing pronounced kinks in the heme. Out-of-plane distortions up to 2 Å are observed in the crystal structure.

Importantly, neither hydrophilic nor aromatic residues were introduced in the heme pocket with these mutations to minimize differences in the dielectric constant in the heme pocket. The net change in partition coefficient of I5L, I5L/P115A, and P115A is 0.11, -0.38, and -0.49 (Appendix Table A5).[78] Introducing polar or aromatic residues will strongly influence the electronic properties of the heme by changing hydrophobicity of the heme pocket and or disrupting hydrogen-bonding networks. Thus, changes in reduction potential of the heme will be a consequence of changing the heme pocket environment and minimally on changes in heme distortion.

Structure determination and analysis of the I5L and I5L/P115A mutants. The crystal structures of I5L and I5L/P115A were solved by molecular replacement using the P115A *Tt* H-NOX crystal structure (PDB ID 3EEE) as a search model to resolutions of 2.15 and 2.04 Å, respectively. The crystallographic data collection and refinement statistics are summarized in Table 3.1. Both structures contain 2 molecules in the asymmetric unit. The R_{work} values for I5L and I5L/P115A are 21.7% and 18.9% and the R_{free} values are 26.0% and 23.5%, respectively.

TABLE 3.1. Statistics of crystallographic data collection and refinement statistics

	I5L		**I5L/P115A**
Data Collection			
Space group	*$P2_12_12$*		*C2*
Cell dimensions			
a, *b*, *c* (Å)	79.825, 126.095, 42.742		127.158, 79.828, 43.322
α, β, γ (°)	90		β = 102.25
Resolution (Å)	2.15		2.04
R_{merge} (%)	6 (42)		5 (14)
I / σ[a]	24.7 (4.8)		22.7 (8.3)
Completeness[a] (%)	99.5 (99.8)		99.4 (95.0)
Redundancy	6.7		3.7
Refinement			
No. of reflections	24124		26928
R_{work} / R_{free}[b] (%)	21.7/26.0		18.9/23.5
No. atoms			
Protein	3066		3098
Heme	86		86
O_2 Molecules	2		2
Solvent molecules	59		148
B-factors			
Overall	43.8		26.0
Rms deviation			
Bond lengths (Å)	0.007		0.008
Bond angles (°)	0.974		1.054

[a] The values in parentheses relate to highest-resolution shells.
[b] R_{free} is calculated for a randomly chosen 5% of reflections.

The root mean square (rms) deviation from planarity, normal-coordinate structural analysis, and interpyrrole angles were calculated for all hemes in I5L and I5L/P115A (Appendix Tables A6 and A7). The iron-histidine tilt was calculated using the least-squares plane of the four pyrrole nitrogens in the heme and the five imidazole ring atoms of His-102 using MOLEMAN2 [52].

Structural comparison of mutants versus wild-type *Tt* H-NOX. The crystal structures of I5L and I5L/P115A show that heme distortion has decreased from wild-type *Tt* H-NOX (Fig. 3.2a-b). All structures are overlaid and compared with monoclinic wild-type molecule A since it has the highest degree of heme distortion. The rms deviation from planarity of I5L heme molecules A and B are both 0.34 Å. The rms deviations from planarity for I5L/P115A heme molecules A and B are 0.20 and 0.16 Å, respectively. Both mutants have lower rms deviations from planarity than wild-type *Tt* H-NOX (0.46 Å). The degree of saddling and ruffling, the iron-histidine tilt, and interpyrrole angles in all heme cofactors for both mutants are lower than the wild-type protein (Appendix Tables A6 and A7).

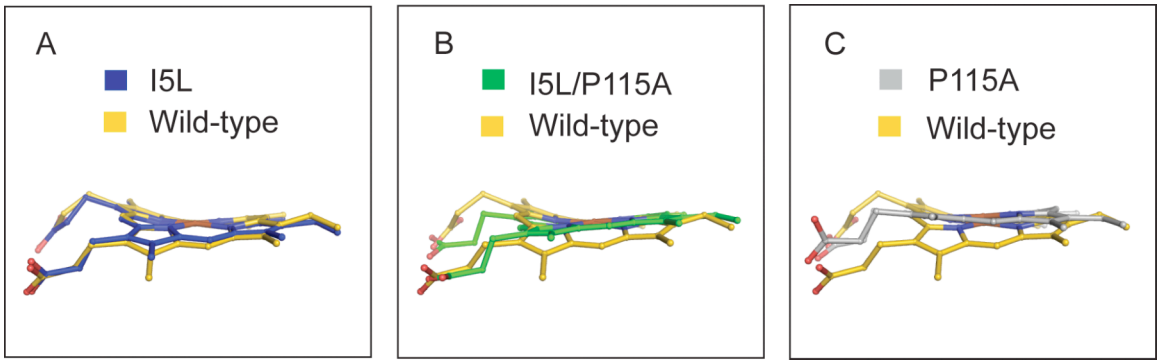

Figure 3.2. Comparison of mutants of *Tt* H-NOX with wild-type *Tt* H-NOX. Shown are A) I5L molecule B (blue), B) I5L/P115A molecule A (green), and C) P115A molecule D (silver) overlaid with wild-type *Tt* H-NOX monoclinic molecule A. All mutants of *Tt* H-NOX have been crystallized with distinct degrees of heme distortion and N-terminal movements from wild-type.

The I5L mutation causes a disruption of the pyrrole A and γ/δ carbon interaction, which allows the heme cofactor to relax and move back into plane. The P115A mutation eliminates the steric bulk at the proximal side of the heme and allows pyrrole D to move back into plane. The double mutant, I5L/P115A did not have an additive effect on inducing planarity of the heme. The two mutations had a counterbalancing effect on each other and the degree of distortion is higher than the single mutant P115A. Regardless, I5L/P115A has a distinct degree of distortion and its chemical properties will be compared to the other constructs.

Previous studies showed that pertubation of the hydrophobicity of the heme pocket,[54,57,59,70] ligation state,[56,58] and changes in the protein scaffold[55,79] effect the reduction potential of the heme. The approach taken here was to minimize those effects on heme reduction potential and focus on physical changes of the porphyrin. It is important to note that the

crystallographic data are in agreement with solution resonance Raman data.[77] All analyses probing the chemical properties will be carried out in solution; therefore it is important that solution experiments are congruent with all crystallographic data. Engineering flatter hemes with distinct degrees of distortion allows for a detailed and quantitative analysis of the effects of porphyrin distortion on heme electronic properties.

Correlation of redox potential with heme distortion. Previous redox potentiometry experiments with *Tt* H-NOX show that the reduction potential is significantly altered when the heme is flattened. The P115A mutant had a reduction potential approximately 180 mV lower than wild-type *Tt* H-NOX.[15] Since the I5L and I5L/P115A mutants also have decreased heme distortion, the reduction potential was measured to assess whether a trend exists between heme distortion and redox potential (Figure 3.3).

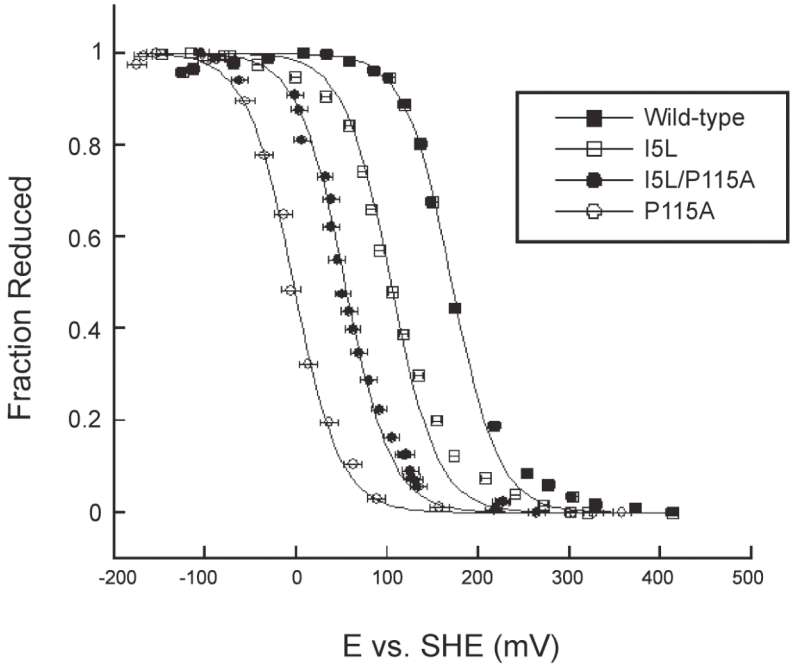

Figure 3.3. Reduction Potential of wild-type and mutants. Titration curves for wild-type[39], I5L, I5L/P115A, and P115A[39] were determined against the standard hydrogen electrode (SHE). The ratio of reduced Fe^{2+} to oxidized Fe^{3+} heme was measured based on their α/β maximum at approximately 557 (reduced) nm for wild-type and I5L. The difference absorbance of the a/b maximum for reduced and the α/β minimum for oxidized was used to calculate the fraction reduced for I5L/P115A and P115A. The voltage against the SHE was measured for both oxidative and reductive titrations of wild-type and mutants. Error bars represent the standard error for wild-type and P115A and range and standard deviation for I5L and I5L/P115A, respectively.

The reduction potential was measured and calculated as described.[39,47] The midpoint potentials for I5L and I5L/P115A were 101.5 ± 5.0 and 56.0 ± 8.9 mV, respectively. The midpoint potentials of the wild-type protein, I5L, I5L/P115A, and P115A were plotted against the mean rms deviation from planarity (Figure 3.4). A clear trend between heme distortion and reduction potential is observed. Specifically, I5L has an intermediate mean rms deviation from planarity of 0.34 Å and a lower reduction potential than wild-type and a higher reduction potential than both I5L/P115A and P115A. The reduction potential of I5L/P115A is approximately 60 mV higher than P115A, however, the mean heme rmsd from planarity is within error. Although the mean rms deviations for both I5L/P115A and P115A are within error, the individual heme cofactors in the asymmetric unit (four hemes in the asymmetric unit) of the crystal structure of P115A samples lower rms deviations from planarity than I5L/P115A (Figure 3.4 and Appendix Table A6), which may explain the lower reduction potential in the P115A mutant.

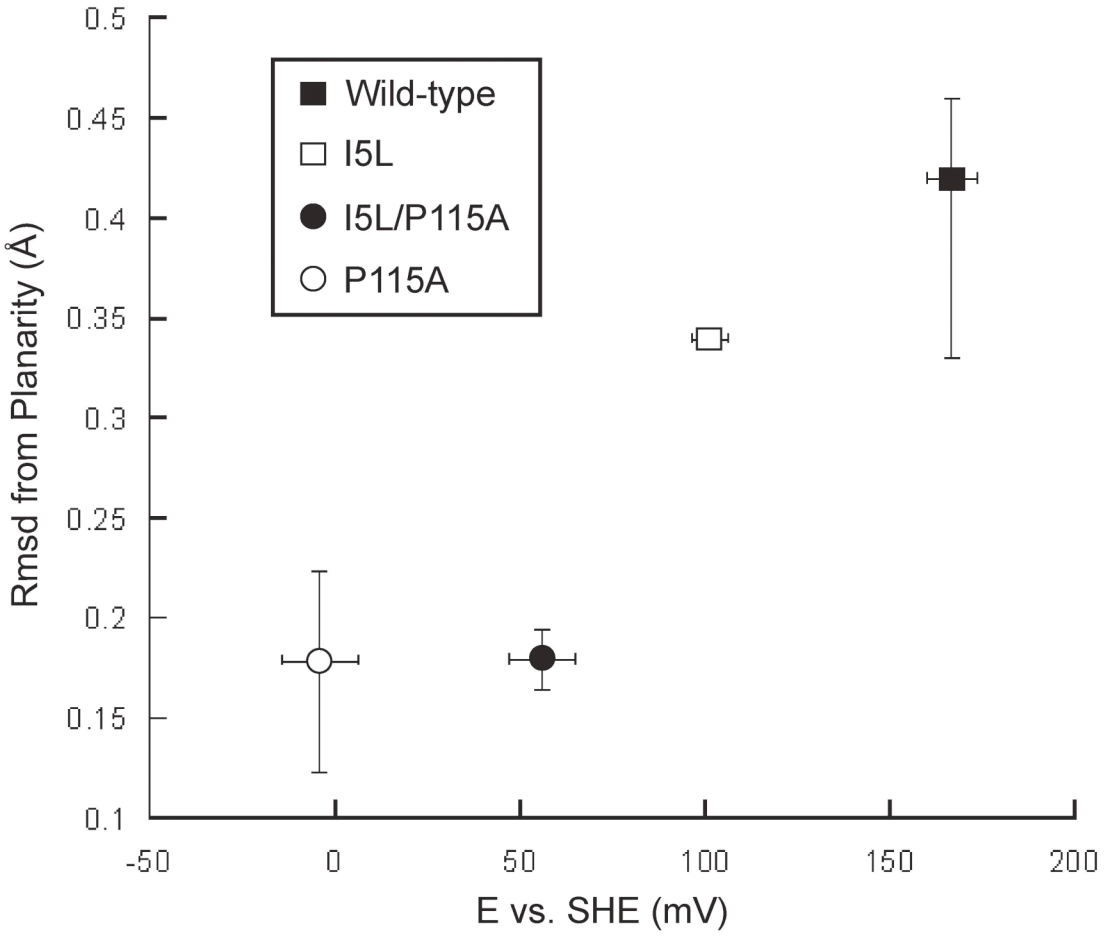

Figure 3.4. Heme distortion versus reduction potential in wild-type and mutants. Plotted is the mean rms deviation from planarity of wild-type and mutants versus the mean reduction potential against SHE. The error bars for the potential represent the standard error for wild-type and P115A and the range and standard deviation for I5L and I5L/P115A. The

vertical bars for the rmsd from planarity represent the range of values for all molecules in the AU for each protein.

The net partition coefficient changes likely are not influencing the reduction potential in our model construct. For example, the partition coefficient in the I5L mutant is increased and should, based purely on dielectric environment, increase in reduction potential. Additionally, the ligation state of the iron remains constant in each of the constructs. However, this is not the case as the reduction potential decreases from wild-type approximately 60 mV. Moreover, a near linear decrease in reduction potential correlating to heme distortion was observed. Thus, the differences in reduction potential are likely to be a consequence of mechanical changes of the porphyrin. Taken together, the data show that as the planarity of the heme cofactor increases, the reduction potential decreases in *Tt* H-NOX with minimal perturbations on the heme environment.

Heme distortion influences the electronics at the heme iron. The reduction potential data show that the electron density at the heme iron decreases as a function of heme distortion. Spectra from the ferric complexes of the wild-type and mutant proteins offer evidence for electron deficiency at the heme iron in the more distorted porphyrins shown (Figure 3.5). The ferric spectrum of wild-type *Tt* H-NOX is characteristic of a 6-coordinate hydroxide-bound heme with a Soret maximum at 415 nm and α/β bands at 590/550 nm, respectively (Figure 3.5B-D).[80] In contrast, the spectra of both I5L/P115A and P115A are characteristic of 6-coordinate aqua-bound heme groups. The Soret maxima for I5L/P115A and P115A are at 404 and 405 nm and the α/β bands are at 615/530 and 610/533 nm, respectively. The spectrum of ferric I5L is characteristic of a mixture of both aqua and hydroxide-bound heme with a Soret maximum of 408 nm and α/β bands at 588/542. The absorption data indicate that the mutant proteins are stabilizing a different protonation state of the axial ligand than wild-type *Tt* H-NOX.

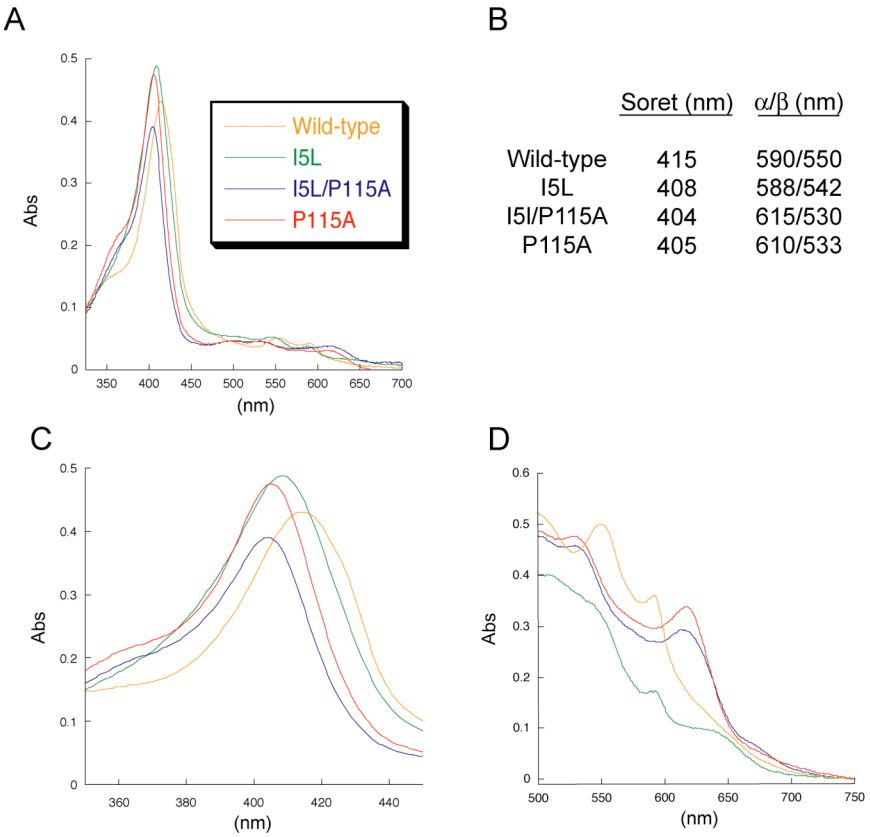

Figure 3.5. Ferric Spectra of wild-type and mutants. A) Full spectra of wild-type mutants. B) Values for λ max of the Soret and α/β regions. Spectral zoom in on the C) Soret and D) α/β regions of wild-type and planar mutants.

The Lewis acidity of the heme iron influences the pK_a of the bound oxygen atom in the ferric form of the heme and change the protonation state of the ligand (favoring either water or hydroxide). The distorted heme in wild-type *Tt* H-NOX would be expected to have an increased Lewis acidity, and therefore, stabilize hydroxide. In contrast, the more electron rich iron in the flatter heme would likely increase the pK_a of the water ligand and thus stabilize the aqua form.

To test this hypothesis, a pH titration was conducted on the ferric forms of wild-type and mutant *Tt* H-NOX proteins. The pK_a values for the distal bound water for wild-type and I5L *Tt* H-NOX were 6.8 and 7.9, respectively (Figure 3.6). The pK_a values of both the I5L/P115A and P115A mutants could not be determined, however, within the range of the experiment since the bound hydroxide ligand could not be protonated due to the stability of the protein at high pH. No change in the absorption spectra of the I5L/P115A and P115A mutants was observable up to a pH of 10 (indicating that the the pK_a values of these mutants are greater than 10).

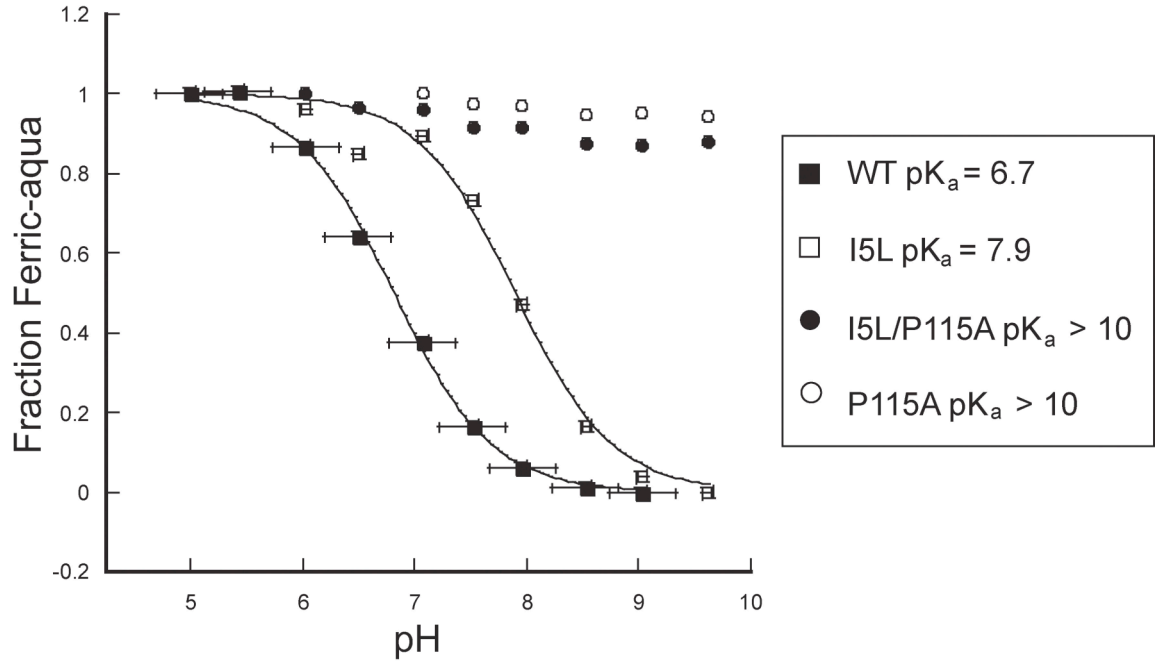

Figure 3.6. pH titration curves and pK$_a$ values of wild-type and mutants. Titrations for wild-type and I5L were fit to the Henderson-Hasselbalch equation. Error bars for wild-type and I5L represent the standard deviation. The pK$_a$ values for I5L/P115A and P115A could not be determined within the range of the experiment.

The results of the reduction potential measurements and pH titration suggest that porphyrin distortion promotes electron deficiency at the heme iron. The determination of the pK$_a$ values further shows evidence of the effects of porphyrin distortion on the electrons of the iron. Importantly, both experiments demonstrate strong evidence for heme distortion controlling the chemistry at the heme in solution.

Molecular orbital model for control of reduction potential. The lone pair nitrogens on the heme pyrroles and the histidine residues in the protein overlap with the d_{x2-y2} and d_{z2} of the iron, respectively (Figure 3.7). The interactions are anti-bonding and, therefore, are high-energy frontier orbitals.[81] Heme distortion in wild-type *Tt* H-NOX causes the orbital overlap to be non-ideal. The interpyrrole angle values in this protein increase up to 32 degrees. Additionally, the iron-histidine tilt is approximately 10 degrees higher than the most planar heme cofactor. The protein scaffold distorts the heme, which bends and weakens the iron/porphyrin bond.

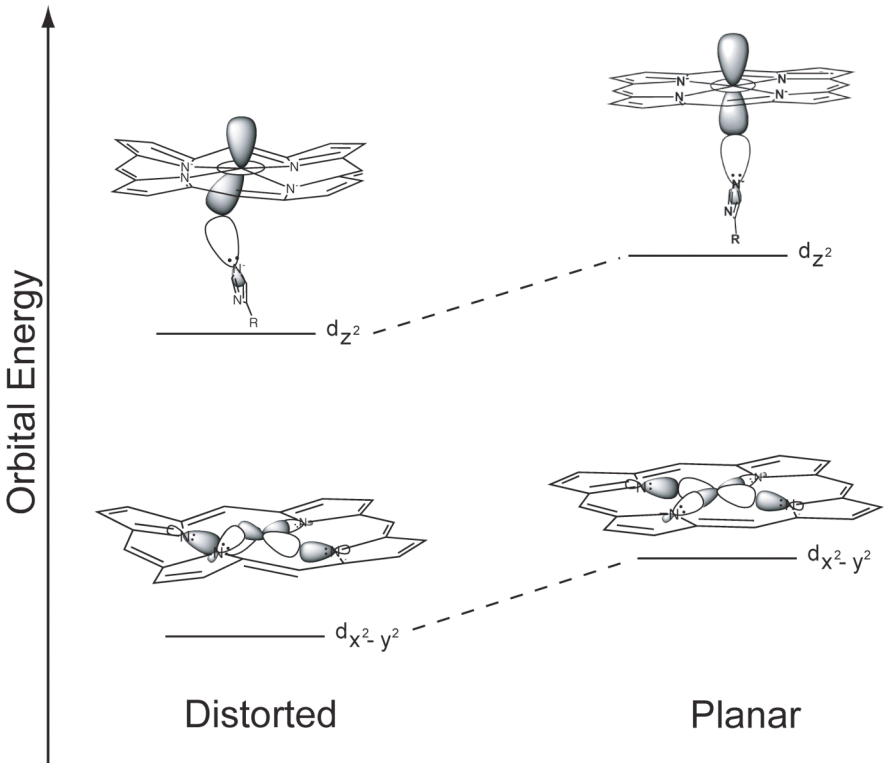

Figure 3.7. Theoretical orbital energy schematic of distorted and planar heme orbital interactions. Shown is a model of the relative energies of the $d_{x2\text{-}y2}$ and d_{z2} orbitals in a distorted and planar heme. Orbital spheres are modeled in for the iron d-orbitals, the lone pairs of the nitrogen pyrrole groups in the heme, and the nitrogen in the proximal histidine.

The mutants have relaxed heme cofactors where overlap in these orbitals is more optimal. The enhanced overlap destabilizes these anti-bonding orbitals, which would cause them to increase in energy (Figure 3.7). This can be explained by the MO model, where the planar heme frontier orbitals, $d_{x2\text{-}y2}$ and d_{z2}, are higher in energy. The higher energy orbitals in the more relaxed Fe (III) heme will less likely accept electrons, thus providing a possible explanation for the lower reduction potential as compared to the wild-type protein.

Conclusions

Previous studies with synthetic porphyrins show that bending the porphyrin significantly changes the reduction potential.[29,31,82,83] The electron withdrawing and donating properties of the substituents in synthetic porphyrins affect the electronic properties of the porphyrin, which heavily influences the reduction potential. Synthetic proteins have been engineered to tune the reduction potential of the heme by inserting charged residues.[68] The ideal system to study the chemical properties of a heme and fine-tuning the reduction potential is in a native protein scaffold.

Previous work demonstrated that mutating a conserved residue, P115, in an H-NOX protein flattened the porphyrin and changed the chemical properties of the heme. Details of how the electronics of the heme are influenced by distortion and whether a trend exists remained unclear. Here we report the crystal structures of mutant proteins with distinct degrees of heme distortion within the context of the same protein scaffold. The degree of heme distortion was found to correlate with the electronic properties of the heme iron. Heme distortion affects the reduction potential of the iron and pH titration experiments support the idea that the electron density of the iron decreases as a function of heme distortion.

Our model suggests the orbital overlap in the distorted heme is decreased, leading to less electron density localized at the iron and an increase in reduction potential. When the heme is planar, the porphyrin contributes more electron density to the iron, making it[82] more electron rich, which correlates with a lower reduction potential Thus, the protein scaffold fine-tunes the electron properties of the heme through modulating heme distortion. Future experiments with different axial ligands and unnatural porphyrins could broaden the range of reduction potentials and change the functionality of the heme cofactor for broader applications.

Chapter 4: Insights Into the Molecular Mechanism of H-NOX Activation

Background

Nitric oxide (NO) signaling in mammals controls processes such as smooth muscle relaxation and neurotransmission via cGMP, which is produced upon activation of the enzyme soluble guanylate cyclase (sGC).[6,7,84] In sGC, NO-mediated breakage of the Fe-His bond leads to increased catalytic activity. Recently, heme domains related to sGC were identified in prokaryotes and were termed Heme-Nitric oxide/OXygen binding (H-NOX) domains.[9,19] Prokaryotic H-NOX proteins fall into two distinct classes. The first consists of a stand-alone H-NOX protein most often found in a predicted operon with either a histidine kinase or, less frequently, with a GGDEF-diguanylate cyclase domain. The second class consists of H-NOX domains fused to methyl-accepting chemotaxis proteins.[8,9,18] Homology to the sGC heme domain as well as genomic location adjacent to putative signaling proteins suggests that H-NOX domains likely serve as O2 and NO sensors in prokaryotes.[9,18]

Consistent with this hypothesis, the ferrous NO complex of the H-NOX from the facultative aerobe, *Shewanella oneidensis* (*So* H-NOX), which belongs to the first class of H-NOX proteins, inhibits autophosphorylation of a histidine kinase encoded in the same operon, whereas the ferrous unliganded protein has no effect on kinase activity.[18] Similar to mammalian sGC, *So* H-NOX is high spin in the ferrous unliganded state, which then forms a transient six-coordinate complex upon binding NO that rapidly converts to a low-spin five-coordinate ferrous nitrosyl complex (Figure 4.1).[15-17] The proximal Fe-His bond is severed upon formation of the five-coordinate NO species, and it is postulated that this results in an activated state through a conformational change induced by the movement of the proximal helix containing the histidine away from the heme cofactor when the Fe-His bond breaks (Figure 4.1).

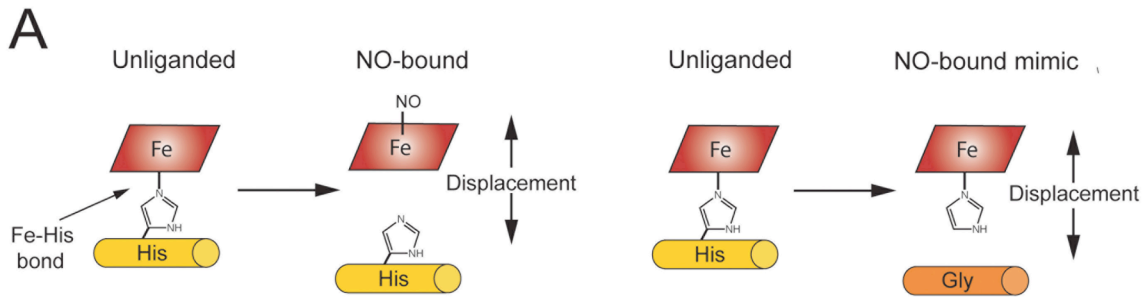

Figure 4.1. H102G mutant rationale. Nitric oxide (NO) binds in a five-coordinate state where the proximal Fe-His bond is broken, which leads to a displacement of the heme and proximal α-helix (α-helix F). Displacement of the heme and proximal helix in the axial histidine mutant. Figure 4.1 was adapted from Olea *et al.*,[85] John Wiley & Sons, Inc.

To date, several crystal structures of prokaryotic H-NOX domains have been solved.[19,20,38] The H-NOX domain from *Thermoanaerobacter tengcongensis* (*Tt* H-NOX), which belongs to the second class of H-NOX domains, binds both NO and O_2. A distal hydrogen-bonding network identified in the structure has been found to play a central role in O_2binding.[12,19] Studies probing the importance of heme cofactor conformation showed that bending of the heme is correlated to N-terminal movement of the protein in *Tt* H-NOX.[39] Although the correlation between heme conformation and protein structure is compelling, the role of this movement in the molecular mechanism of signal transduction was not clear.

To better understand the mechanistic basis of H-NOX activation, solution structures were solved that mimic the active five-coordinate NO and inactive (unliganded) *So* H-NOX.[86] These structures suggest that removal of the Fe-His bond, mimicked by the axial Fe-His mutant (H103G), results in conformational changes in the heme cofactor and a N-terminal shift in the protein similar to those observed in P115A *Tt* H-NOX.[39] Much insight into the structural changes resulting from mimicking "cleavage" of the Fe-His bond was gained from the NMR study. However, because of limitation in isotopic labeling, especially at the heme, the NMR structures do not allow for an in-depth, atomic analysis of the structural changes.

High-resolution crystallography, in contrast, can provide detailed information on all atoms in the protein and heme cofactor with high accuracy. *Tt* H-NOX is an ideal protein to study H-NOX structure because crystals typically diffract to ~2 Å. Thus, the analogous axial histidine mutant, H102G, was made in *Tt* H-NOX. The goal of this study was to obtain insight into the molecular mechanism of H-NOX activation. The results with the axial ligand mutant should provide key structural information on H-NOX activation in atomic level detail. Information from the crystal structure will demonstrate whether heme cofactor conformation and structure correlation is a general mechanism with heme and proximal helix displacement, which mimics Fe-His bond dissociation, in H-NOX proteins.

Materials and Methods

Protein purification. Mutagenesis was carried out using the QuikChange protocol from Stratagene. Expression and purification of *Tt* H-NOX H102G were carried out as previously described[9,87] with the addition of 10 mM imidazole to all purification buffers and expression media. It has been demonstrated that heme binding in the axial histidine H-NOX mutants can be rescued with exogenous imidazole.[87]

H102G crystallization - F1 crystal form. Samples of *Tt* H-NOX H102G were exchanged into buffer containing 20 m*M* TEA (pH 7.5) and 10 m*M* imidazole (buffer A) and oxidized using 100 equiv of potassium ferricyanide [$K_3Fe(CN)_6$]. Potassium ferricyanide was removed using a PD10 column (Amersham Biosciences) preequilibrated with buffer A and H102G was then concentrated to 30 mg mL^{-1}. Crystals were grown using sitting drop vapor diffusion by mixing 1 μL of the protein solution with 1 μL of the reservoir solution equilibrating against a

700 μL reservoir of 28% (w/v) PEG 3350 and 0.25 M $Mg(CH_3COO)_2$ at 20°C. Crystals began to appear within 24 h. Cryoprotection was achieved by transferring the crystals stepwise into mother liquor solutions containing increasing concentrations of glycerol ending with 15% (v/v) glycerol. Crystals were flash frozen in liquid nitrogen and stored for later use in data collection.

H102G crystallization - F2 crystal form. H102G samples were prepared as mentioned above. Small needle clusters were grown using hanging drop vapor diffusion by mixing 1 μL of the protein solution with 1 μL of reservoir solution, 20% (w/v) PEG 3350 and 0.2 M KCl, and equilibrated against 700 μL of the reservoir solution at 4°C. Large single crystals were grown overnight by mixing 1μL of a 15 mg mL^{-1} protein solution with 1 μL of seeding solution. Seeding mother liquor was generated with the Seed Bead kit (Hampton Research). Crystals began to appear within 24 h. Cryoprotection was achieved as described above.

X-ray data collection, phasing, and refinement. X-ray data were collected using synchrotron radiation at beamline 5.0.3 at the Advanced Light Source, Lawrence Berkeley National Laboratory. Diffraction images were collected at 100 K with 5 s exposure times and 1° oscillation per frame. Data were processed using the HKL2000[41] suite, and molecular replacement was performed using Phaser[42] with wild-type *Tt* H-NOX (PDB ID 1U55) as the search model. Model building was carried out using Coot[44] and refined using Phenix.[46] The final models for crystal forms F1 and F2 were refined to a final R_{work} of 21.5 and 20.7% (R_{free} of 25.1 and 25.5%) at 2.0 and 2.1 Å, respectively.

Results and Discussion

Structure determination and analysis of *Tt* H-NOX H102G. The H102G *Tt* H-NOX mutant was expressed and purified as previously described[9,87] and crystallized in several crystal forms. The crystal structure was solved by molecular replacement in two crystal forms (F1 and F2) and refined to 2.0 and 2.1 Å, respectively. The R_{work} for crystal forms F1 and F2 was 21.5 and 20.7%, respectively, and the R_{free}values were 25.1 and 25.5%, respectively (PDB ID: 3LAH and 3LAI). A total of two and three Fe(III)-bis-imidazole H102G molecules for crystals F1 and F2, respectively, were built in orthorhombic asymmetric unit cells. Crystallographic data and refinement statistics are summarized in Table I.

TABLE 1. Statistics of crystallographic data collection and refinement

	F1	F2
Data Collection		
Space group	$P2_12_12_1$	$P2_12_12_1$
Cell dimensions		
a, *b*, *c* (Å)	61.4, 88.7, 89.2	61.4, 86.5, 122.7
α, β, γ (°)	90	90

Resolution (Å)	44.6-2.0	50-2.1
R_{merge} (%)	7.3 (43.5)	6.9 (38.1)
I / σ[a]	24.8 (2.9)	27.5 (4.3)
Completeness[a] (%)	97.5 (80.1)	100 (100)
Redundancy	6.9	7.1
Refinement		
No. of reflections	33172	36487
R_{work} / R_{free} [b] (%)	21.5/25.1	22.4/24.9
No. atoms		
Protein	3196	4739
Heme	86	129
Imidazole Molecules	4	6
Solvent molecules	147	120
B-factors		
Overall	31	37
Rms deviation		
Bond lengths (Å)	.008	.023
Bond angles (°)	0.867	1.564

[a] The values in parentheses relate to highest-resolution shells.
[b] R_{free} is calculated for a randomly chosen 5% of reflections.

H102G was compared to wild-type Fe(III) *Tt* H-NOX (PDB ID: 1U56 Molecule A) to maintain consistency in the oxidation states for structural analysis. Using the Difference Distance Matrix Program (Center for Structural Biology at Yale University, New Haven, CT), C-terminal residues 120-175 of H102G were aligned with wild type. N-terminal root mean square deviation (RMSD) from wild-type *Tt* H-NOX was calculated for H102G (Appendix Table A9). Figure 4.2a shows the electron density maps ($2F_o$ - F_c) of H102G (crystal form F2 Molecule a A and B) at 1.0s contour levels. The electron density map was generated with the imidazoles and hemes omitted. The electron density map clearly shows the disconnection of the proximal helix from the heme cofactor in the H102G mutant. Additionally, all atoms in the heme pocket have low *B* factors (~20-40 $Å^2$) relative to the rest of the protein (~>40 $Å^2$) and thus can be modeled with high confidence.

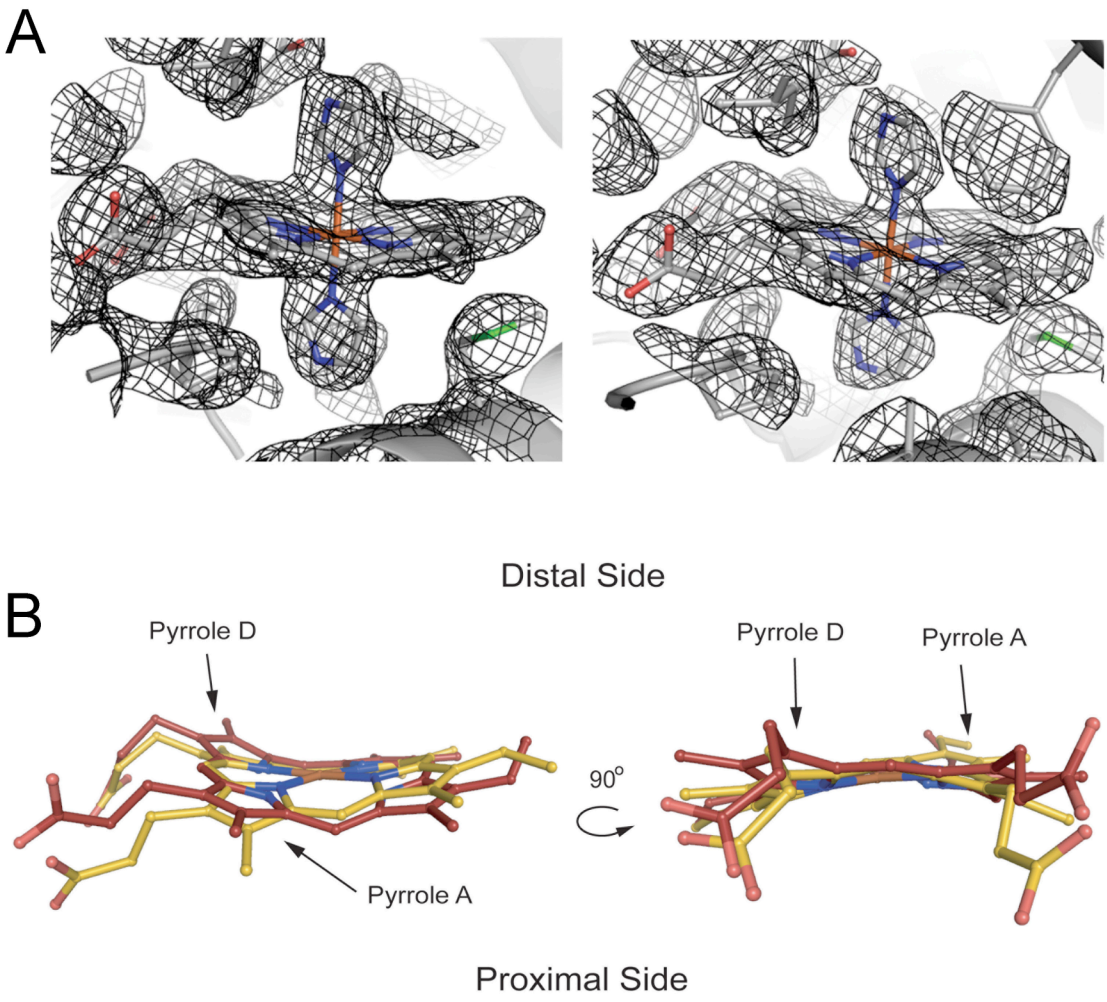

Figure 4.2. Electron density map and structural comparison of H102G (PDB ID: 3LAH and 3LAI) versus wild type (PDB ID: 1U56). a) 2Fo - Fc electron density map of the heme pockets in H102G crystal form F2 (PDB ID: 3LAI) for molecules A and B at 1.0σ contour levels. The imidazoles and hemes were omitted during the generation of the electron density map. b) H102G heme cofactor (maroon) overlaid with wild type (gold). The heme cofactor in H102G adopts a significantly different conformation when compared with wild type. Pyrroles A and D move toward the distal pocket. Figure 4.2 was adapted from Olea *et al.*,[85] John Wiley & Sons, Inc.

All five molecules in both crystal forms of the H102G H-NOX exhibit significant differences in conformation compared with wild-type *Tt* H-NOX, as illustrated by an alignment of H102G with wild type in Figure 4.3. The N-terminus in H102G is displaced from wild type with N-terminal RMSD values that range from 2.78 to 3.78 Å (Appendix Table A9). Importantly, the same movements are observed in two different crystal forms that vary in unit cell dimensions and asymmetric units, which act as a control to show that changes observed are not a result of a crystallographic artifact. Molecule B from H102G crystal F2 was used for subsequent analyses because it has the largest N-terminal RMSD from wild type.

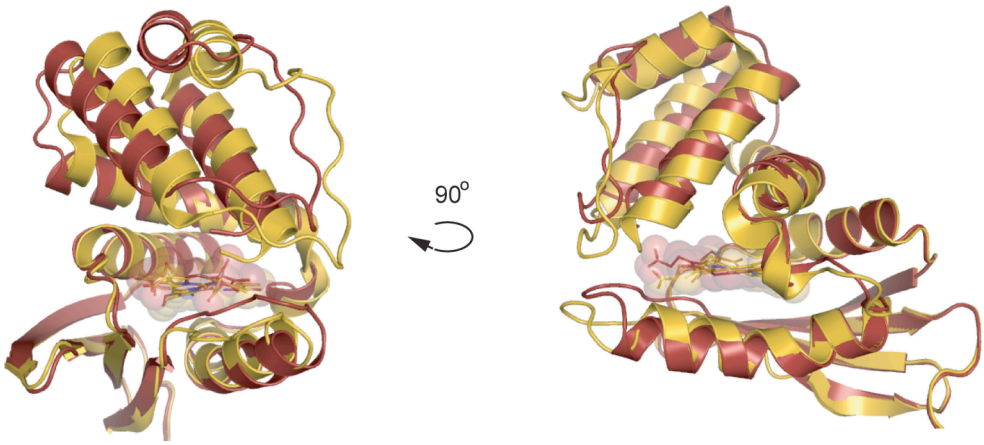

Figure 4.3. Effects of H102G on the overall structure. Overall structural comparison of H102G (maroon) versus wild type (gold). A significant N-terminal shift away from wild type is observed in H102G. Shown are F2 molecule B and molecule A for H102G and wild type, respectively. Figure 4.3 was adapted from Olea *et al.*,[85] John Wiley & Sons, Inc.

Analysis of the heme-binding pocket

Although free porphyrin is planar in solution, protein-bound heme cofactors are not planar and adopt various conformations.[23] The heme cofactor from wild-type *Tt* H-NOX contains one of the most distorted hemes reported to date.[19] Biochemical and structural studies have revealed that heme distortion is correlated to changes in heme reactivity, ligand binding, and protein conformation.[19,29,31-34,39,88] As observed in the structure reported here, disconnection of the heme and proximal helix in the H102G mutant results in a significantly relaxed heme cofactor conformation. A comparison of the heme cofactors shows that pyrroles A and D move away from the proximal side of the heme pocket toward the distal side in the H102G mutant compared with wild type (Figure 4.2b).

Normal-coordinate analysis (NSD) was carried out on the heme cofactor in H102G for both crystal forms (Appendix Table A10). The major heme distortion modes in the wild-type protein are saddling and ruffling (Appendix Table A10). In Fe(III) wild-type molecule A, the NSD values for saddling and ruffling are -1.115 and -1.171, respectively. Dissociation of the heme from the proximal helix reduces saddling, whereas little change in ruffling is observed. Specifically, saddling in H102G ranges from -0.263 to 0.725. Heme ruffling, however, is similar to that of wild-type *Tt* H-NOX with a range between -0.980 and -1.216. Thus, the structure shows that only one distortion mode is affected upon removal of His-102, which mimics cleavage of the Fe-His bond.

Overall, the H102G crystal structure suggests that dissociation of the Fe-His bond leads to a general conformational change of the heme exemplified by a decrease in saddling. The resulting increased space in the heme pocket allows the heme to relax to a lower energy conformation. The H102G structure may illustrate the importance of the Fe-His bond in maintaining the unusually large deviation from planarity of the heme in *Tt* H-NOX. All H-

NOX proteins possess proximal histidine ligation to the heme iron and strong evidence suggests that NO binding leads to breakage of this bond in most non-O_2-binding H-NOX proteins.[15,16] Thus, this type of heme conformational change may be a general feature in the H-NOX family that leads to an effect on downstream function.

Conformational change in the H102G mutant

Local rearrangements of heme pocket residues Met-1 and Ile-5 in H102G made possible by relaxation of the heme translate into large displacements of the N-terminus (greater than 6 Å) compared with wild-type *Tt* H-NOX (Figure 4.4a, Appendix Table A9). Met-1 and Ile-5 move together with pyrrole A and the attached propionate group (Figure 4.4a-b). This propionate group moves above the plane of the heme toward the N-terminus and correlates with the observed N-terminal shift of the protein. Hydrogen-bonding contacts with the propionate groups, including those in the conserved YxSxR motif, have not appreciably changed from wild type.[19] Both Met-1 and Ile-5 are part of a-helix A, which is at the beginning of the N-terminus and make van der Waals contact with the distal side of the heme. The helices that comprise the rest of the N-terminus move along with a-helix A about a pivot point between two glycines within a-helices D and G (residues 61-81 and 138-153, respectively), similar to those in *So* H-NOX.[86]

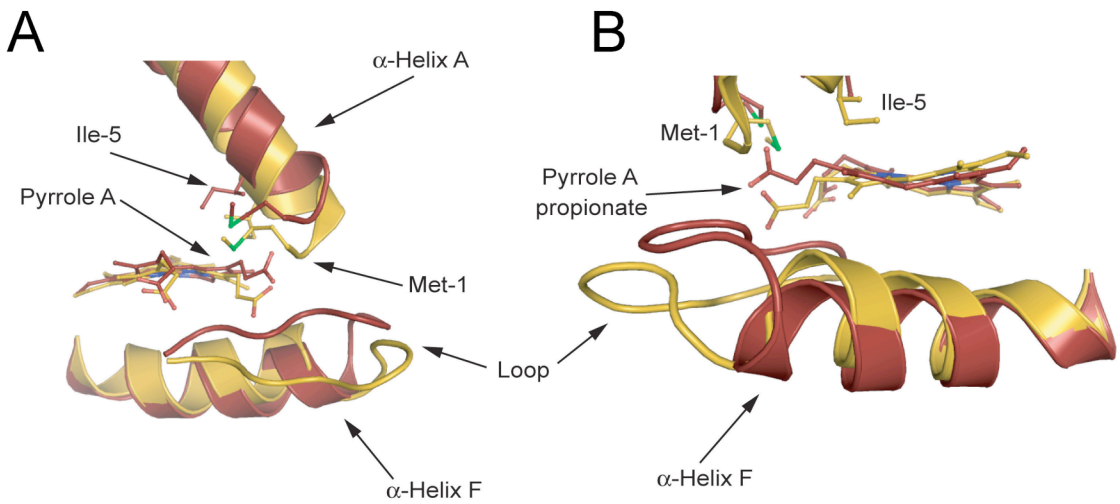

Figure 4.4. Effects of H102G on the local heme environment. A) Pyrrole A, Met-1, and Ile-5 move with the heme causing large conformational changes at the N-terminus. B) The propionate group attached to pyrrole A moves above the heme plane along with an insertion of the loop following α-Helix F. The H102G mutant allows for displacement of α-helix F away from the heme cofactor. Figure 4.1 was adapted from Olea *et al.*,[85] John Wiley & Sons, Inc.

The H102G mutant also results in movement of α-helix F (residues 90-107) as observed in Figure 4.4b. The liberated a-helix F moves away from the distal pocket toward the C-terminus of the protein. Along with the movement of the propionate group mentioned above, the loop between α-helix F and β-sheet A (residues 108-113) moves with the pyrrole A propionate

group (Figure 4.4a-b). In the previous crystal structures of *Tt* H-NOX, the loop between α-helix F and β-sheet A was highly disordered and could not be modeled-in with high confidence. However, in the H102G structure, the loop is ordered and surprisingly moves with the N-terminus and heme propionate group.

Previously, the design of a flattened heme mutant (P115A) in *Tt* H-NOX has demonstrated that changes in the degree of heme distortion are coupled to N-terminal displacement.[39] This proline makes tight van der Waals contact with the heme in wild-type *Tt* H-NOX, and the less crowded heme pocket in the mutant provides room for the heme to relax. The change in heme deformation was found to be correlated to movement in the N-terminal half of the protein. Here, we find that elimination of the α-helix F attachment to the heme cofactor via the H102G mutation results in similar structural changes. Thus, the elimination of the connection between the heme and α-helix F, which is suggested to occur upon five-coordinate NO formation, is consistent with our model linking heme distortion and N-terminal movement.

It is important to note that the distal imidazole makes a hydrogen bond with Tyr-140. The distance between the Fe and Tyr is increased by 1 Å; however, this is also observed in published structures (PDB ID: 3EEE and 3IQB) of mutants with planar hemes that are oxygen bound.[39,89] If the histidine is responsible for the structural change alone, the 1 Å increase is not enough to account for the >6 Å movement at the N-terminus. Thus, the mechanism of the structural change is likely caused by heme flattening.

A conserved molecular mechanism for Fe-His bond dissociation. The high-resolution crystal structure reported here of H102G shows that changes in the conformation of the heme cofactor can be ascribed to a decrease in the amount of saddling. The N-terminus/heme coupled movement is similar to what is observed for the P115A mutant. That is, pyrrole A moves above the plane toward the distal side of the heme pocket, along with its attached propionate group, eliciting a shift in the N-terminal half of the protein through interactions with a-helix A. NMR structures of the analogous axial histidine mutant in *So* H-NOX also show a relaxation of the heme cofactor.[15] Despite the fact that the resolution of these structures is limited because of restricted isotopic labeling of the heme, a flattening of the heme was observed, as well as a conformational change at the N-terminus.

We recently speculated that the Fe-His bond and the distorted heme may act as a "loaded spring" through maintaining the heme and protein in an inactive conformation in *So* H-NOX.[15] Upon NO binding, the Fe-His bond is broken and the five-coordinate complex is formed, which leads to a kinase inhibitory form of *So* H-NOX. Here, we propose that the *Tt* H-NOX H102G mutation mimics NO binding through movement of the proximal helix away from the heme, allowing the heme to adopt a more relaxed conformation. When the Fe-His bond is broken, the heme may adopt a lower energetic conformation and stored potential energy is released, leading to the observed structural changes in the protein. The observation of similar conformational changes in two different homologues representing two classes of H-NOX domains suggests that the structural changes may be general with Fe-His bond dissociation and is possibly important for sensing and transmitting a ligand-binding signal.

Conclusions

The crystal structure of the axial histidine H102G mutant in *Tt* H-NOX, a mimic of the five-coordinate NO complex, was solved to 2.0 Å. The high-resolution structure showed that only one major heme distortion mode was affected by disconnection of the heme and proximal helix, which likely mimics Fe-His bond breakage, and atoms that were disordered in previous crystals structures are participating in the movement of the protein. Local changes at the heme cofactor and in the heme pocket lead to global conformational changes in the protein. These significant conformational changes caused by dissociation of the heme and proximal helix have now been observed in two different H-NOX homologues. Removal of the Fe-His bond may lead to heme and protein conformational changes, which likely represent a general mechanism for activation in the H-NOX family.

Chapter 5: Crystal Structure of a 5-coordinate Unligated Mimic of an O_2-binding H-NOX

Background

There are two sub-classes of H-NOX domains.[9] One class, which is found in mammals and facultative aerobes are selective for binding NO in the presence of atmospheric concentrations of oxygen. The other class is found in insects and anaerobic bacteria and bind oxygen in a six-coordinate complex. In oxygen-binding H-NOX domains, the distal pocket contains a conserved hydrogen-bonding network that is responsible for selectivity of oxygen.[12] In atypical cyclases, the unligated complex of H-NOX has no effect on cyclase activity. However, when bound to oxygen in the 6-coordinate complex, cyclase activity is inhibited.[11] Previous structural studies on H-NOX domains has concentrated on the non-oxygen binding H-NOX protein properties.[38,85,86] However, very little is known about the mechanism of ligand binding in H-NOX proteins that bind oxygen.

Tt H-NOX is an oxygen binding H-NOX and has been crystallized in the six-coordinated oxygen-bound state. This construct serves as a model for oxygen binding H-NOX domains and is an excellent candidate for X-ray crystallographic studies, since the wild-type and mutant constructs have been crystallized numerous times.[19,20,39,85,89,90] A crystal structure of an unligated complex will provide insight into the response of ligand binding in oxygen-binding H-NOX domains.

Previous attempts at obtaining an unligated crystal structure of *Tt* H-NOX have met with failure due to the high affinity for oxygen. The K_D for oxygen is 90 nM and at atmospheric conditions *Tt* H-NOX is completely oxygen bound.[39] Under anaerobic conditions the unligated complex can be formed (Figure 5.1A), however the complex rebinds O_2 within the timescale of crystal growth.

Zn-porphyrin (Figure 5.1B) has been incorporated in globins as a model of the unligated complex.[91-93] The Zn-porphyrin binds to the protein in a 5-coordinate unligated fashion mimicking the ferrous unligated complex. Zn-porphyrin is closed-shell and thus is square planar in solution, however due to proximity effects in the protein, histidine ligates to the Zn metal. Thus, the goal would be to incorporate the Zn-porphyrin into *Tt* H-NOX to obtain a mimic of the ferrous unligated complex.

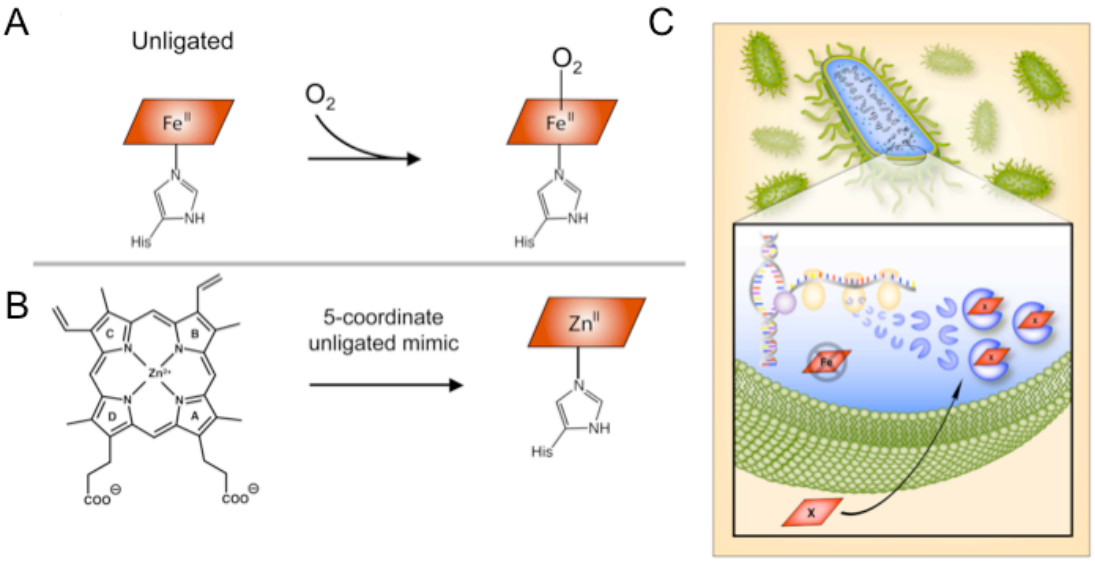

Figure 5.1. Zn-porphyrin acts as a mimic of the ferrous unligated state and native incorporation of orthogonal porphyrins. A) Schematic of oxygen binding in H-NOX domains. In atypical sGC, cyclase activity is inhibited upon binding oxygen. B) Zn-porphyrin acts as a mimic of the ferrous unligated H-NOX protein. C) Schematic of the heme knock-out *E. coli* cell line. The *E. coli* strain has a step in the heme biosynthesis pathway mutated and an uncharacterized heme intake mutation. Orthogonal porphyrins are supplemented during protein expression are natively incorporated into heme proteins. Figure 5.1C was obtained from Woodward *et al.*,[94] Nature Publishing Group.

The method to strip hemes and incorporate orthogonal porphyrins is harsh and is not ideal for crystallography.[95] Woodward *et al.* have developed and method to incorporate orthogonal porphyrins in Nitric Oxide synthase (NOS, Figure 5.1c).[95] The method utilizes an *E. coli* strain that has a gene in the heme biosynthesis pathway knocked-out and an uncharacterized heme permeability mechanism.[96] This method has been fined-tuned for total incorporation of mesoporphyrin into *Tt* H-NOX.[90]

The method for incorporating orthogonal porphyrins in *E. coli* was used to obtain the Zn-substituted *Tt* H-NOX domain (Zn *Tt* H-NOX). Zn *Tt* H-NOX was crystallized and the crystal structure was solved to 2.12 Å. Comparison of the oxy-bound and Zn *Tt* H-NOX shows dramatic structural changes associated with ligand binding. The crystal structure shows a relationship with heme conformation and N-terminal movement seen in other H-NOX domains. These studies may reveal insight into the molecular mechanism of response to ligand binding in oxygen-binding H-NOX domains.

Materials and Methods

Expression and purification of Zn *Tt* H-NOX. Cell culture and expression procedures were carried out as described.[90]

Crystallization of Zn *Tt* H-NOX. All crystallization experiments were conducted with minimal exposure to light and crystal trays were placed in the dark. Samples of Zn *Tt* H-NOX were equilibrated with 20 mM TEA pH 7.5 and concentrated to 25 mg/mL. Crystals were grown by sitting drop vapor diffusion by mixing 1 μL of protein solution with 1 μL of the reservoir solution and equilibrating against 700 μL of 20% 3350 PEG and 0.1-0.2 M NaF overnight at 16°C. Cryoprotection was achieved by addition of mother liquor substituted with 30% glycerol in increasing glycerol amounts of 5% to a final concentration of 15% glycerol, flash frozen, and stored in liquid nitrogen.

X-ray data collection, phasing, and preliminary refinement of Zn *Tt* H-NOX. X-ray data were collected by using synchrotron radiation at beamline 5.0.3 at the Advanced Light Source, Lawrence Berkeley National Laboratory. Diffraction images were collected at 100 K with 5 s exposure time and 1° oscillations per frame. Data were processed anomalously with the HKL2000 suite.[41] Molecular replacement was carried out with the CCP4 program Phaser[42] using wild-type *Tt* H-NOX (PDB ID: 1U55) as the search model. Model building was carried out by using the program Coot[44] and refinement was carried out using Phenix.[46] The model includes 6 Zn *Tt* H-NOX molecules in the asymmetric unit. The structure was refined to an overall R_{work} and R_{free} of 20.6% and 23.6% at 2.12 Å resolution, respectively.

Results and Discussion

Structure Determination and Analysis of Zn *Tt* H-NOX. The crystal structure was solved by molecular replacement with wild-type *Tt* H-NOX (PDB ID: 1U55) and single-wavelength anomalous dispersion (SAD) to 2.12 Å. The crystal structure contains 6 molecules of Zn *Tt* H-NOX in the asymmetric unit. The UV-vis of dissolved crystals shows a characteristic of a 5-coordinate Zn-porphyrin complex.[91] Data collection and refinement of Zn *Tt* H-NOX are summarized in Table 5.1.

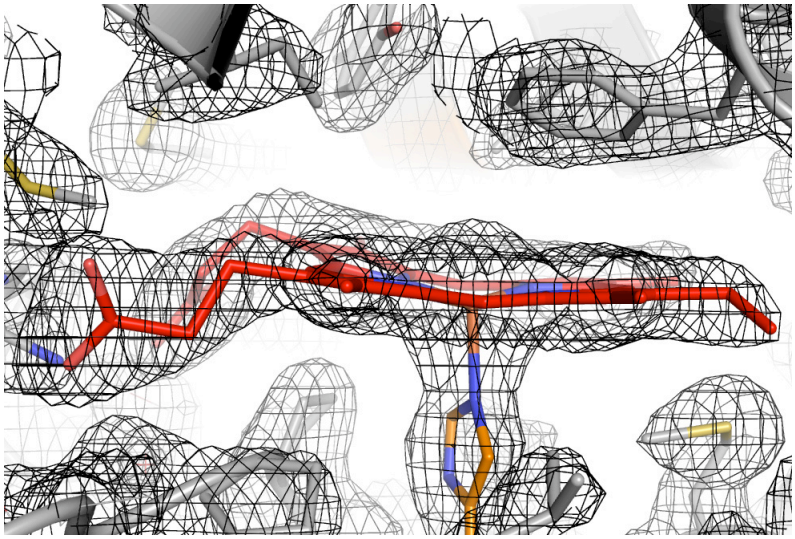

Figure 5.2. Electron Density Map of Zn *Tt* H-NOX. The Zn-porphyrin is shown in red and His-102 is shown in orange. The electron density map was calculated with the Zn-porphyrin and His-102 residue omitted at 1.5 σ. The electron density is continuous between the His and Zn bond. Importantly, no electron density is observed above the heme.

TABLE 5.1. Preliminary Statistics of crystallographic data collection and refinement statistics

Data Collection	
Space group	$P3_1$
Cell dimensions	
a, *b*, *c* (Å)	112.7, 112.7, 123.1
α, β, γ (°)	90, 90, 120
Resolution (Å)	50-2.12 (2.20- 2.12)
R_{merge} (%)	8.2 (69.3)
I / σ[a]	20.2 (2.4)
Completeness[a] (%)	100 (100)
Redundancy	5.7 (5.4)
Refinement	
No. of reflections	83875
R_{work} / R_{free}[b] (%)	20.6/23.6
No. atoms	9346
Protein	
Zn-porphyrin	258
Water molecules	305
Rms deviation	
Bond lengths (Å)	0.009
Bond angles (°)	1.253

[a] The values in parentheses relate to highest-resolution shells.
[b] R_{free} is calculated for a randomly chosen 5% of reflections.

An electron density map was calculated with the Zn-porphyrin and the proximal histidine side-chain omitted. A clear link between the Zn and His is observed in the electron density map. The Zn-His bond length is within error of the wild-type Fe-His (Appendix Table A11). Importantly, no electron density is observed above the plane of the porphyrin indicating that no ligand is bound in the distal pocket. The data clearly show that Zn *Tt* H-NOX is a potential mimic of a 5-coordinate unligated complex. Root mean square deviation from planarity and normal-coordinate analysis were calculated for all 6 Zn-porphyrins in the asymmetric unit (Appendix Table A12). N-terminal deviation from wild-type were calculated for Zn *Tt* H-NOX as described (Appendix Table A13).[39]

Significant Conformational Change Observed Upon O_2-binding. A dramatic protein conformation difference is observed in Zn *Tt* H-NOX when compared to oxy-bound wild-

type. Similar to previous structural studies of H-NOX domains, a large N-terminal shift is observed upon ligand binding in wild-type *Tt* H-NOX. The N-terminus rotates around a glycine pivot point identical to that observed in *So* H-NOX[86] and *Tt* H102G.[85] The largest N-terminal shift of all H-NOX proteins is observed when comparing oxy-bound wild-type and Zn *Tt* H-NOX. Specifically, over a 6 Å shift is observed upon ligand binding.

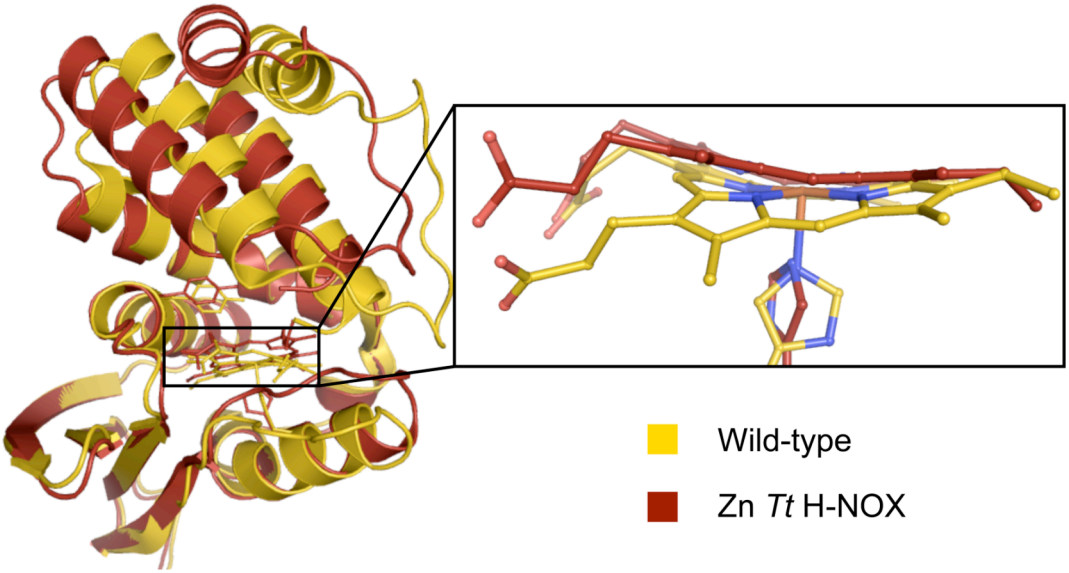

Figure 5.3. Comparison of Zn *Tt* H-NOX with Wild-type. Zn molecule A and wild-type molecule A (1U55) are shown in maroon and gold, respectively. A shift over 6 Å at the N-terminus is observed upon oxygen binding. The 5-coordinate Zn-porphyrin mimic is significantly flatter than wild-type.

Porphyrin Distortion in Zn *Tt* H-NOX. The Zn-porphyrins in all 6 molecules in the asymmetric unit are significantly flatter than wild-type (Figure 5.3 and Appendix Table A12). In wild-type the rmsd from planarity is as high as 0.46 Å, whereas it ranges from 0.19-0.23 Å in Zn *Tt* H-NOX. The major contributions to porphyrin distortion in wild-type as calculated by normal-coordinate structural decomposition (NSD) are ruffling and saddling. In wild-type molecule A, which has the highest degree of porphyrin distortion, the values of ruffling and saddling are -1.105 and -1.069, respectively. In Zn *Tt* H-NOX both ruffling and saddling decrease significantly. The values for ruffling and saddling range from -0.248 to -0.560 and -0.237 and -0.392 Å, respectively.

Doming of the porphyrin is observed in the Zn-porphyrin. In wild-type *Tt* H-NOX, the Fe was in the plane of the heme, so no significant doming modes were observed. However, the Zn metal dips below the plane of the porphyrin in a similar fashion as ferrous unligated globin structures.[25] The NSD doming modes were calculated for Zn *Tt* H-NOX and ranged from 0.315 to 0.451, respectively (Appendix Table A12). The trans effect from the distal ligand is absent in Zn *Tt* H-NOX, therefore allowing the Zn to be pulled out of plane the proximal histidine ligand.

Mechanism for Oxygen-binding. Several key structural changes occur upon oxygen binding. The distance between the metal and all residues in the distal hydrogen-bonding network are shorter when oxygen-bound (Appendix Table A11). The distance between the Tyr-140 hydroxyl when oxy-bound is 5.14 Å, whereas in Zn *Tt* H-NOX it is 6.11 Å. The distances from the heme of Trp-9 and Asn-74 are 8.50 and 8.36 Å when unligated and decrease to 7.21 and 6.79 Å when oxygen-bound, respectively. Essentially, the oxygen ligand acts as a link between the N-terminus and the heme (Figure 5.4).

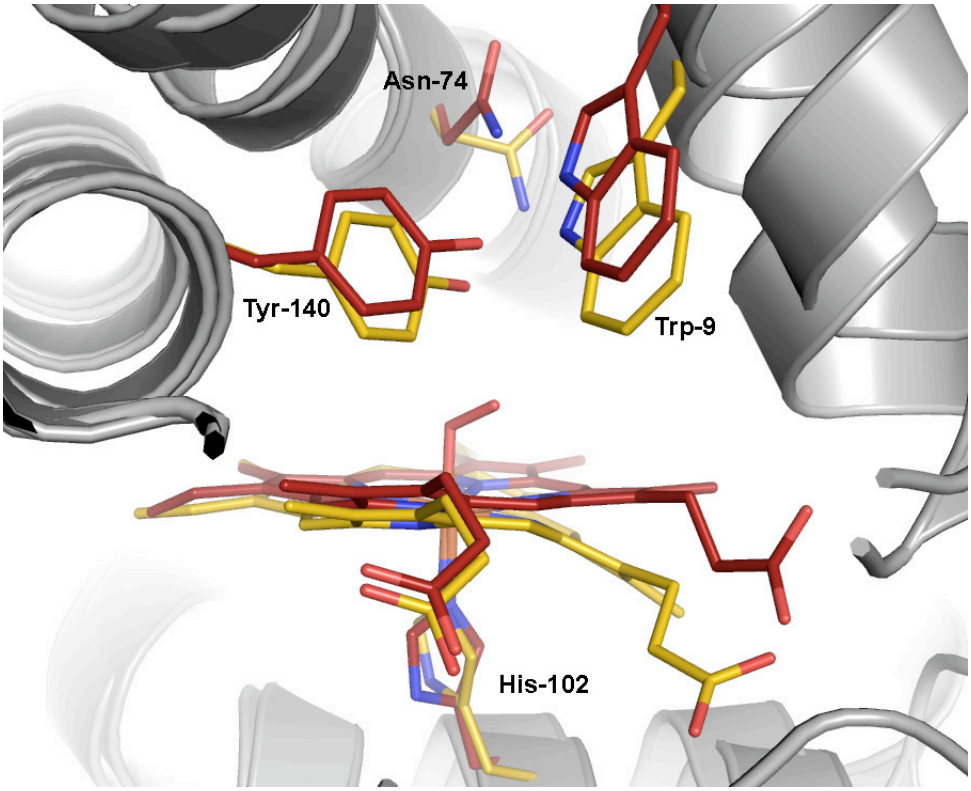

Figure 5.4. Hydrogen bonding network in wild-type vs. Zn *Tt* H-NOX. The distal hydrogen bonding residues Trp-9, Asn-74, and Tyr-140 are shown. Zn and wild-type *Tt* H-NOX residues are shown in maroon and gold, respectively. All hydrogen-bonding residues are farther away from the metal center in Zn *Tt* H-NOX.

The linking of the two domains causes a shift up to 6 Å at the N-terminus (Figure 5.5). The N-terminal rmsd of Zn *Tt* H-NOX from the oxygen-bound wild-type ranges from 4.10 to 4.43 Å. The largest N-terminal rmsd from wild-type for all H-NOX mutants previously reported was 3.76 Å for P115A *Tt* H-NOX.[39] It is important to note that all other H-NOX constructs in previous studies contained mutations to the protein scaffold and that the question invariably arose whether the protein folding may have contributed to the results. Here, the wild-type scaffold was used and the heme was natively incorporated during protein expression, which further validates previous experiments probing H-NOX mechanism using mutants.

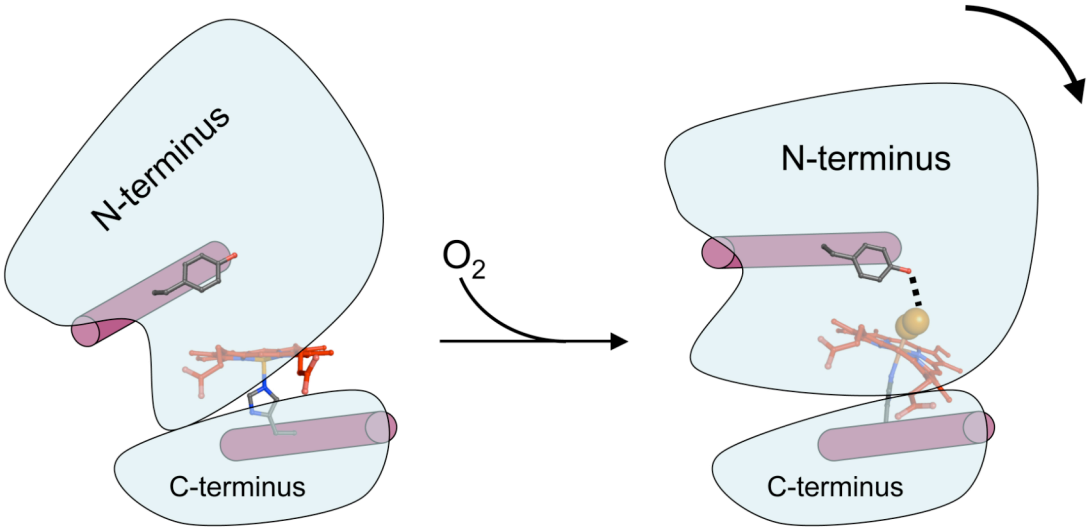

Figure 5.5. Proposed Model for Response for Oxygen-binding. Oxygen links the N-terminus to the C-terminal domain in *Tt* H-NOX. An N-terminal shift over 6 Å is observed upon oxygen binding.

The degree of heme distortion significantly increases upon oxygen binding. When the two domains are pulled together by oxygen, the heme pocket decreases in size. The heme is allowed less flexibility in the pocket since new van der Waals interactions from heme pocket residues are introduced. Oxygen-binding created by a tight packing of the heme forces the porphyrin to adopt a non-planar conformation.

It has been shown previously that bending the porphyrin in *Tt* H-NOX changes the binding and electrochemical properties of the heme. The H-NOX domain is part of a membrane protein that contains a methyl-accepting chemotaxis protein (MCP) predicted to sense oxygen.[39] MCP domain mechanisms are part of an adaptive response where the initial stimulus has less effect over time. Specifically, heme deformation in *Tt* H-NOX decreases the affinity for oxygen over 4-fold. Whether the decrease in oxygen binding in response to stimuli is part of an adaptive response in Tar4 is yet to be determined.

Conclusions

The crystal structure of an unligated mimic of *Tt* H-NOX was solved to 2.12 Å resolution. Oxygen-binding causes a large conformational change in the protein and heme cofactor. Oxygen acts as a link between the N- and C-terminal domains of *Tt* H-NOX. Tyr-140, which is part of the N-terminus, hydrogen bonds to the oxygen stabilizing a six-coordinate ferrous-oxy complex. Forming of the hydrogen bond causes Tyr-140, and consequently, the rest of the N-terminus to shift towards the heme and C-terminus. Upon oxygen binding the heme

pocket encloses on the heme, distorting it significantly from planarity. These results provide new insight into the molecular mechanism of oxygen binding in H-NOX proteins.

Chapter 6: Initial Biochemical Characterization of Tar4

Background

There are two broad categories of H-NOX proteins. The first do not form a complex with O_2 and appear to be NO sensors. Examples include the NO receptor soluble guanylate cyclase found in mammals and the H-NOXs from facultative aerobes such *Shewanella oneidensis*. The second category contains a distal hydrogen-bonding network that stably binds O_2 and is predicted to sense oxygen. The response and regulation by NO is better characterized in mammals and prokaryotes,[7,18] whereas, only one oxygen-binding H-NOX domain from *Drosophila* has been biochemically characterized.[11]

The H-NOX domain from *Thermoanerobacter tengcongensis* (*Tt* H-NOX) is part of a Tar4 protein predicted to sense oxygen (Figure 6.1). Tar4 is comprised of an N-terminal H-NOX domain followed by a TM-2 transmembrane region and a C-terminal methyl-accepting chemotaxis protein (MCP). Since *T. tengcongensis* is an obligate anaerobe and the H-NOX binds O_2 with very high affinity, it is predicted that Tar4 is part of an oxygen avoidance mechanism. The high affinity of the H-NOX domain for oxygen may allow Tar4 to be a sensitive sensor of O_2 and with subsequent activation of the MCP domain, lead to chemotaxis away from oxygen.

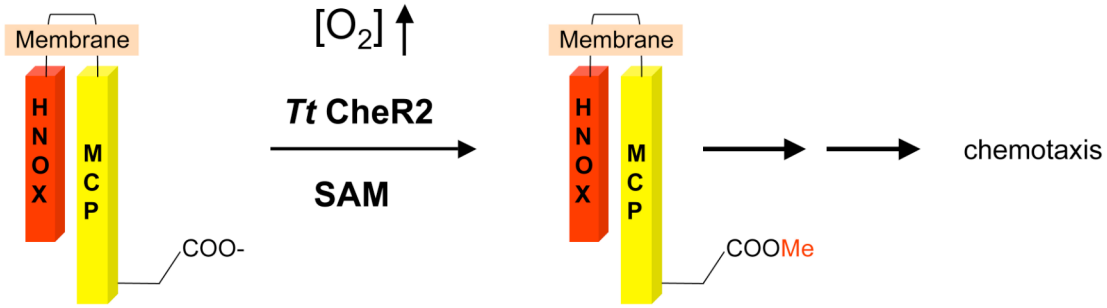

Figure 6.1. Tar4 is Predicted to be Involved in Chemotaxis. Tar4 contains an H-NOX, type-2 transmembrane spanning, and a methyl-accepting chemotaxis (MCP) domain. It is predicted that the H-NOX domain will bind oxygen and activate the MCP domain to become methylated by the methyltranferase, *Tt* CheR2. The methylated MCP may act on downstream proteins leading to chemotaxis in *T. tengcongensis*.

The proposed mechanism for sensing oxygen is through an allosteric interaction between the H-NOX and MCP domain. Under strict anaerobic conditions, the H-NOX domain would be in the ferrous unligated state and predicted to be locked in a particular conformation (See Chapter 5, this thesis). Upon oxygen binding, there is a major conformational change caused by the relative movement of N- and C-terminal domains. This conformational change likely leads to the generation or elimination of contacts with the MCP domain. The MCP domain

will then be in a state favoring methylation by a cognate methyl transferase, predicted to be *Tt* CheR2 (Figure 6.1).

Many kinetic and structural studies have been conducted on *Tt* H-NOX and mutants;[12,39,89] however, no functional characterization currently exists. The goal is to reconstitute activity of Tar4 and to develop a working assay where methylation activity can be monitored as a function of oxygen binding. Next, will be to incorporate mutants of the H-NOX domains that have been kinetically and structurally characterized into Tar4. This chapter focuses on initial results of reconstituting Tar4 and quantitative analysis on the MCP domain. Future directions will also be discussed.

Materials and Methods

Materials. The pET20b vector and *E. coli* Tuner (DE3) competent cell line were purchased from Novagen, *T. tengcongenis* genomic DNA was purchased from DMSZ (German Collection of Microorganisms and Cell Cultures). Restriction enzymes and were purchased from New England Biolabs (NEB). IPTG was from Promega. The High Fidelity PCR and Ligation kits were purchased from Roche. Miniprep and gel extraction kits were purchased from Qiagen. Ni-NTA superflow resin was purchased from Qiagen. Talon Metal Affinity Resin was purchased from Clontech. 4-(2-Aminoethyl)-benzenesulfonylfluoride hydrochloride (PefaBloc) was from BIOSYNTH. Primers were from Elim Biopharmaceuticals. S-adenosylmethionine was from NEB. Tridiated S-Adenosyl-L-[Methyl-^{3}H]methionine was purchased from PerkinElmer.

Expression Vectors. Tar4 and *Tt* CheR2 was PCR amplified from *T. tengcongenis* genomic DNA. The upstream and downstream primers for Tar4 were 5'-GGAATTCCATATGAAGGGGACAATCGTCGGGACATGG-3' 5'-CTGCAGCGCCCGCTCAAACTTTGTATTTATCAAGCTCCTTC-3', respectively. The upstream and downstream primers for *Tt* CheR2 were 5'-CTGCACATATGGTAGGCTATGAGGAATTTG-3' and 5'-GCTGCGGCCGCTTTTTGAAAACTGATTTTTTTGTAG-3', respectively for a C-terminal 6-His tag. For the MCPc249 construct upstream primer was 5'-CTGCACATATGCCTGCTAAG AATCTTCATG-3' and the downstream was the same for Tar4. For all upstream and downstream primers the NdeI and NotI restrictions sites were used, respectively. All PCR fragments were gel purified, digested, and ligated in the pET20b expression vector. All constructs were sequenced by Elim Biophamaceuticals.

Expression. Tar4 and MCPc249 were expressed as previously described.[9] *Tt* CheR2 was expressed as previously described[9] except with 200 μM IPTG added during induction.

Protein Purification. Tar4, MCPc249, and *Tt* CheR2 cells were lysed and homogenized as previously described.[9] Tar4 lysate was centrifuged at 25000g for 1 hr. The supernatant was collected and centrifuged at 100,000g for 2 hr. The membrane containing pellets were washed with 50 mM TEA, 1 M NaCl, pH 7.5 using a dounce homogenizer. The 100,000g and high salt wash steps were repeated twice. MCPc249 lysate subjected to thermal treatment

at 70 °C for 45 min and centrifuged at 100,000g for 1 hr. The supernatant was applied to a POROS HQ 7.9 mL anion-exchange column (Applied Biosystems) that had been equilibrated with 50 mM TEA, 50 mM NaCl, pH 7.5 and washed with 5 column volumes at a flow rate of 10 mL/min. MCPc249 was eluted from the column using a linear gradient of 50 to 500 mM NaCl in a total volume of 100 mL at 10 mL/min. Fractions were run on SDS-PAGE and collected based on purity (> 95%). The was then run over a SP 650M cation exchange column equilibrated in 50 mM Hepes pH 6.25 at 1 mL/min. Flow-through was collected, glycerol was added to a final concentration of 5 %, and stored at -80 °C. *Tt* CheR2 lysate was subjected to thermal treatment and centrifuged as described above. The supernatant was collected and applied to a 10 mL Ni-NTA Superflow (Qiagen) column and washed with 20 column volumes of 50 mM TEA, 10 mM imidazole, 300 mM NaCl, pH 7.5. The protein sample was eluted with of 50 mM TEA, 250 mM imidazole, 300 mM NaCl, pH 7.5 and purity was determined by SDS PAGE (> 95%). The identity of MCPc249 and *Tt* CheR2 was determined by Electrospray Ionization mass spectrometry (UC Berkeley – QB3 Institute Mass Spectrometry Facility) and protein concentrations were determined by the Bradford method.

Methylation assay. Reactions contained 5 μM Tar4 or MCPc249, 50 μM S-adenosylmethionine (SAM) ([^{3}H-methyl]SAM 50 Ci/mmol; MP Biomedicals), 0.1 μM *Tt* CheR2 in 50 mM TEA/NaCl at pH 7.5. Reactions were quenched on filter paper and washed with 200 mL of 10 % TCA and 500 mL 99% ethanol. The filter paper was dried and placed in scintillation vials containing 10 mL of scintillation liquid (MP Biomedicals) and measured with LS 650 (Beckman Coulter).

Mass Spectrometry. Methylation reactions containing the soluble MCPc249 domain were analyzed by nanoelectrospray ionization (nanoESI). The reactions were injecting into a reverse phase ultraperformance liquid chromatography column connected to a quadrupole tome-of-flight mass spectrometer (Q-Tof Premiere, Waters). Trypsin digested reactions were analyzed by tandem mass spectrometry (MS/MS). Data were processed with ProteinLynx Global Server software (Waters).

Results

Reconstitution of Tar4 Activity. Tar4 enriched membranes were isolated from *E. coli.* Tar4 was placed in solution with tritiated SAM and *Tt* CheR2 for 30 min and analyzed by liquid scintillation. The reaction with Tar4, SAM, and *Tt* CheR2 showed a significant increase in activity compared with a control reaction without transferase and control membranes where Tar4 was no expressed. The MCPc249 soluble domain of Tar4 also showed activity in the presence of transferase.

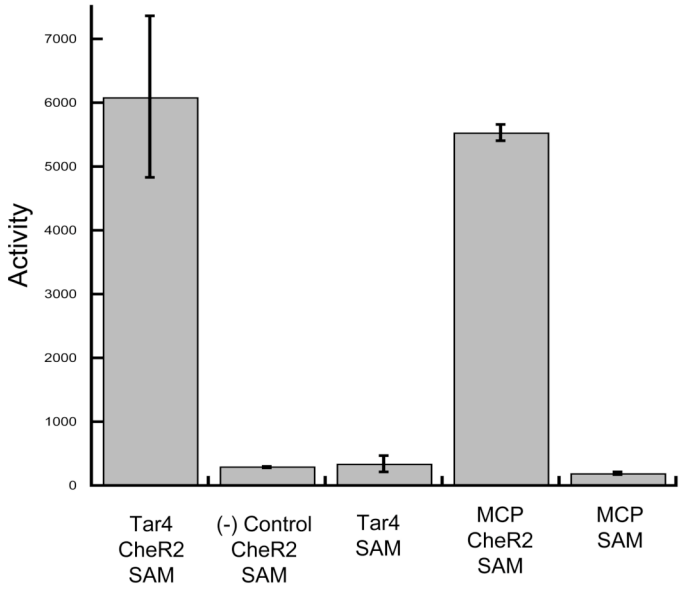

Figure 6.2. Reconstitution of Tar4 activity. Tar4 activity end-point assays after 30 min. are shown. Tar4 is active in the presence of *Tt* CheR2 and SAM. Negative control membranes and reactions without *Tt* CheR2 show no activity. MCPc249 is active in the presence of *Tt* CheR2 and SAM.

MCPc249 is the soluble MCP domain (residues 249-602) of Tar4. The soluble domain can be used for quantitative analysis with mass spectrometry, since the membrane samples are not amenable with MS. The reactions solutions were analyzed by nanoESI with and without *Tt* CheR2 to determine the number of methylation sites in the MCP domain (Figure 6.3). In the presence of transferase, an increase in mass of 28 Da is observed for MCPc249. The increase of 28 Da corresponds to 2 methyl groups.

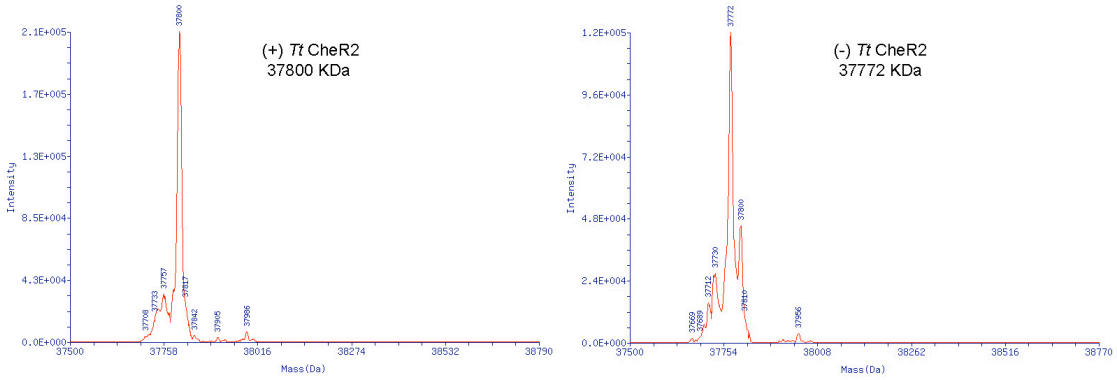

Figure 6.3. MCPc249 is Methylated at Two Sites. Nanoelectrospray ionization of the intact MCPc249 with (+) and without (-) *Tt* CheR2. An increase in mass of 28 Da is observed in the presence of SAM and *Tt* CheR2 indicative of two sites of methylation.

To determine the sites of methylation, reactions that had been incubated with transferase overnight were trypsinized. The peptides were analyzed by tandem mass spectrometry (MS/MS). Over 83% sequence coverage of MCPc249 was achieved (Figure 6.4). Only one

methylation site, Glu-557, was identified with MS/MS. Although only one site was identified, five other glutamates were not covered in the MS/MS experiment. Different digestion strategies such as alternative peptidases will be implemented to identify the second methylation site.

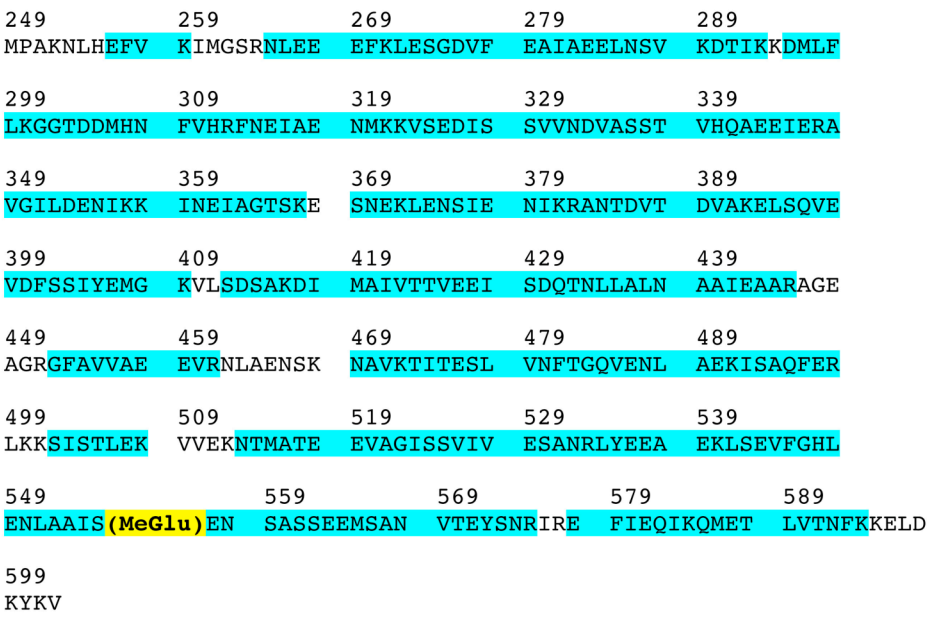

Figure 6.4. Identification of Methylation Sites in MCPc249. MCPc249 was methylated and digested with trypsin. The digested protein was analyzed using liquid chromatography tandem mass spectroscopy (MS/MS). Highlighted residues are covered peptides. Glu-557 was identified as being methylated.

Future Directions

It is predicted that Tar4 is a sensor for oxygen in *T. tengcongensis* and that ligand binding is coupled to changes in heme distortion with a downstream effect on a signal transduction pathway (Chapter 5, this thesis).[19,39] Currently, a methylation assay for Tar4 in the presence and absence of oxygen is under development. The rates of methylation will be determined for oxy-bound and the ferrous unligated complex of Tar4. The addition of oxygen scavengers in a sealed vial and monitoring methylation over time will most likely achieve the anaerobic conditions required to deoxygenate the H-NOX domain.

Mutations in the heme pocket, driven by several structures that have been already solved, will be introduced into Tar4 and assayed for activity. Specifically, P115A will be the first candidate to be used in the assay, since it is known that this mutation leads to a significant relaxation of the distorted heme. Also, a Zn porphyrin will be incorporated into Tar4. The Zn *Tt* H-NOX is potential mimic for the ferrous unligated complex and the porphyrin is planar and the protein a major conformational change from wild-type is observed. Zn porphyrin Tar4 construct is stable in air, so this construct can be used if potential problems with the anaerobic assay arise.

References

(1) Moncada, S.; Palmer, R. M.; Higgs, E. A. *Pharmacol. Rev.* **1991**, *43*, 109-42.
(2) Haagen-Smit, A. J. *Ind. and Eng. Chem.* **1952**, *44*, 1342-1346.
(3) MacMicking, J.; Xie, Q. W.; Nathan, C. *Annu. Rev. Immunol.* **1997**, *15*, 323-50.
(4) Hare, J. M.; Colucci, W. S. *Prog. Cardiovasc. Dis.* **1995**, *38*, 155-66.
(5) Toda, N.; Okamura, T. *Pharmacol. Rev.* **2003**, *55*, 271-324.
(6) Derbyshire, E. R.; Marletta, M. A. *Handb Exp Pharmacol* **2009**, 17-31.
(7) Denninger, J. W.; Marletta, M. A. *Biochim. Biophys. Acta* **1999**, *1411*, 334-50.
(8) Iyer, L. M.; Anantharaman, V.; Aravind, L. *BMC Genomics* **2003**, *4*, 5.
(9) Karow, D. S.; Pan, D.; Tran, R.; Pellicena, P.; Presley, A.; Mathies, R. A.; Marletta, M. A. *Biochemistry* **2004**, *43*, 10203-10211.
(10) Gray, J. M.; Karow, D. S.; Lu, H.; Chang, A. J.; Chang, J. S.; Ellis, R. E.; Marletta, M. A.; Bargmann, C. I. *Nature* **2004**, *430*, 317-22.
(11) Huang, S. H.; Rio, D. C.; Marletta, M. A. *Biochemistry* **2007**, *46*, 15115-22.
(12) Boon, E. M.; Huang, S. H.; Marletta, M. A. *Nature Chem Biol* **2005**, *1*, 53-9.
(13) Boon, E. M.; Marletta, M. A. *Curr. Opin. Chem. Biol.* **2005**, *9*, 441-6.
(14) Boon, E. M.; Marletta, M. A. *J. Inorg. Biochem.* **2005**, *99*, 892-902.
(15) Stone, J. R.; Marletta, M. A. *Biochemistry* **1996**, *35*, 1093-9.
(16) Zhao, Y.; Brandish, P. E.; Ballou, D. P.; Marletta, M. A. *Proc. Natl. Acad. Sci. U.S.A.* **1999**, *96*, 14753-8.
(17) Cary, S. P.; Winger, J. A.; Derbyshire, E. R.; Marletta, M. A. *Trends Biochem Sci* **2006**, *31*, 231-9.
(18) Price, M. S.; Chao, L. Y.; Marletta, M. A. *Biochemistry* **2007**, *46*, 13677-13683.
(19) Pellicena, P.; Karow, D. S.; Boon, E. M.; Marletta, M. A.; Kuriyan, J. *Proc. Natl. Acad. Sci. U.S.A.* **2004**, *101*, 12854-12859.
(20) Nioche, P.; Berka, V.; Vipond, J.; Minton, N.; Tsai, A. L.; Raman, C. S. *Science* **2004**, *306*, 1550-3.
(21) Boon, E. M.; Davis, J. H.; Tran, R.; Karow, D. S.; Huang, S. H.; Pan, D.; Miazgowicz, M. M.; Mathies, R. A.; Marletta, M. A. *J. Biol. Chem.* **2006**, *281*, 21892-902.
(22) Schmidt, P. M.; Schramm, M.; Schroder, H.; Wunder, F.; Stasch, J. P. *J. Biol. Chem.* **2004**, *279*, 3025-32.
(23) Shelnutt, J. A.; Song, X. Z.; Ma, J. G.; Jia, S. L.; Jentzen, W.; Medforth, C. J. *Chem. Soc. Rev.* **1998**, *27*, 31-41.
(24) Jentzen, W.; Ma, J. G.; Shelnutt, J. A. *Biophys. J.* **1998**, *74*, 753-763.
(25) Springer, B. A.; Sligar, S. G.; Olson, J. S.; Phillips, G. N. *Chem. Rev.* **1994**, *94*, 699-714.
(26) Anderson, K. K.; Hobbs, J. D.; Luo, L. A.; Stanley, K. D.; Quirke, J. M. E.; Shelnutt, J. A. *J. Am. Chem. Soc.* **1993**, *115*, 12346-12352.
(27) Zbylut, S. D.; Kincaid, J. R. *J. Am. Chem. Soc.* **2002**, *124*, 6751-6758.
(28) Li, D.; Stuehr, D. J.; Yeh, S. R.; Rousseau, D. L. *J. Biol. Chem.* **2004**, *279*, 26489-99.
(29) Ravikanth, M.; Chandrashekar, T. K. *Coordination. Chem.* **1995**, *82*, 105-188.
(30) Weichsel, A.; Andersen, J. F.; Roberts, S. A.; Montfort, W. R. *Nature Structural Biology* **2000**, *7*, 551-554.

(31) Barkigia, K. M.; Chantranupong, L.; Smith, K. M.; Fajer, J. *J. Am. Chem. Soc.* **1988**, *110*, 7566-7567.
(32) Maes, E. M.; Roberts, S. A.; Weichsel, A.; Montfort, W. R. *Biochemistry* **2005**, *44*, 12690-9.
(33) Shokhireva, T.; Berry, R. E.; Uno, E.; Balfour, C. A.; Zhang, H.; Walker, F. A. *Proc. Natl. Acad. Sci. U.S.A.* **2003**, *100*, 3778-83.
(34) Roberts, S. A.; Weichsel, A.; Qiu, Y.; Shelnutt, J. A.; Walker, F. A.; Montfort, W. R. *Biochemistry* **2001**, *40*, 11327-37.
(35) Ma, J. G.; Laberge, M.; Song, X. Z.; Jentzen, W.; Jia, S. L.; Zhang, J.; Vanderkooi, J. M.; Shelnutt, J. A. *Biochemistry* **1998**, *37*, 5118-5128.
(36) Ryeng, H.; Ghosh, A. *J. Am. Chem. Soc.* **2002**, *124*, 8099-8103.
(37) Gong, W.; Hao, B.; Mansy, S. S.; Gonzalez, G.; Gilles-Gonzalez, M. A.; Chan, M. K. *Proc. Natl. Acad. Sci. U.S.A.* **1998**, *95*, 15177-82.
(38) Ma, X.; Sayed, N.; Beuve, A.; van den Akker, F. *EMBO J.* **2007**, *26*, 578-88.
(39) Olea, C., Jr.; Boon, E. M.; Pellicena, P.; Kuriyan, J.; Marletta, M. A. *ACS Chem. Biol.* **2008**, *3*, 703-710.
(40) Ma, J. G.; Zhang, J.; Franco, R.; Jia, S. L.; Moura, I.; Moura, J. J.; Kroneck, P. M.; Shelnutt, J. A. *Biochemistry* **1998**, *37*, 12431-12442.
(41) Otwinowski, Z.; Minor, W. *Macromol. Cryst., Part A* **1997**, *276*, 307-326.
(42) McCoy, A. J.; Grosse-Kunstleve, R. W.; Storoni, L. C.; Read, R. J. *Acta Crystallogr., Sect. D* **2005**, *61*, 458-464.
(43) Kleywegt, G. J.; Jones, T. A. *Acta Crystallogr., Sect. D* **1996**, *52*, 829-832.
(44) Emsley, P.; Cowtan, K. *Acta Crystallogr., Sect. D* **2004**, *60*, 2126-2132.
(45) Brunger, A. T.; Adams, P. D.; Clore, G. M.; DeLano, W. L.; Gros, P.; Grosse-Kunstleve, R. W.; Jiang, J. S.; Kuszewski, J.; Nilges, M.; Pannu, N. S.; Read, R. J.; Rice, L. M.; Simonson, T.; Warren, G. L. *Acta Crystallogr., Sect. D* **1998**, *54*, 905-921.
(46) Adams, P. D.; Grosse-Kunstleve, R. W.; Hung, L. W.; Ioerger, T. R.; McCoy, A. J.; Moriarty, N. W.; Read, R. J.; Sacchettini, J. C.; Sauter, N. K.; Terwilliger, T. C. *Acta Crystallogr., Sect. D* **2002**, *58*, 1948-54.
(47) Dutton, P. L. *Methods Enzymol.* **1978**, *54*, 411-435.
(48) Shelnutt, J. A. *Journal of Porphyrins and Phthalocyanines* **2001**, *5*, 300-311.
(49) Giangiacomo, L.; Ilari, A.; Boffi, A.; Morea, V.; Chiancone, E. *J. Biol. Chem.* **2005**, *280*, 9192-202.
(50) Capece, L.; Marti, M. A.; Crespo, A.; Doctorovich, F.; Estrin, D. A. *J. Am. Chem. Soc.* **2006**, *128*, 12455-61.
(51) Friedman, J. M.; Rousseau, D. L.; Ondrias, M. R.; Stepnoski, R. A. *Science* **1982**, *218*, 1244-6.
(52) Kleywegt, G. J.; Jones, T. A. *Acta Crystallogr., Sect. D* **1999**, *55*, 941-944.
(53) Johnson, M. S.; Zhulin, I. B.; Gapuzan, M. E.; Taylor, B. L. *J. Bacteriol.* **1997**, *179*, 5598-601.
(54) Mauk, A. G.; Moore, G. R. *J. Biol. Inorg. Chem.* **1997**, *2*, 119-125.
(55) Mao, J. J.; Hauser, K.; Gunner, M. R. *Biochemistry* **2003**, *42*, 9829-9840.
(56) Kennedy, M. L.; Silchenko, S.; Houndonougbo, N.; Gibney, B. R.; Dutton, P. L.; Rodgers, K. R.; Benson, D. R. *J. Am. Chem. Soc.* **2001**, *123*, 4635-4636.

(57) Kassner, R. J. *Proc. Natl. Acad. Sci. U.S.A.* **1972**, *69*, 2263-2267.
(58) Tezcan, F. A.; Winkler, J. R.; Gray, H. B. *J. Am. Chem. Soc.* **1998**, *120*, 13383-13388.
(59) Cowley, A. B.; Kennedy, M. L.; Silchenko, S.; Lukat-Rodgers, G. S.; Rodgers, K. R.; Benson, D. R. *Inorg. Chem.* **2006**, *45*, 9985-10001.
(60) Holm, R. H.; Kennepohl, P.; Solomon, E. I. *Chem. Rev.* **1996**, *96*, 2239-2314.
(61) Gilardi, G.; Fantuzzi, A.; Sadeghi, S. J. *Curr. Opin. Struct. Biol.* **2001**, *11*, 491-9.
(62) Kanan, M. W.; Nocera, D. G. *Science* **2008**, *321*, 1072-1075.
(63) Marshall, N. M.; Garner, D. K.; Wilson, T. D.; Gao, Y. G.; Robinson, H.; Nilges, M. J.; Lu, Y. *Nature* **2009**, *462*, 113-116.
(64) Lu, Y.; Yeung, N.; Sieracki, N.; Marshall, N. M. *Nature* **2009**, *460*, 855-62.
(65) Gilardi, G.; Fantuzzi, A. *Trends Biotechnol.* **2001**, *19*, 468-76.
(66) Sykes, A. G. *Heme-Fe Proteins*; Academic Press: San Diego, 2001; Vol. 51.
(67) Reedy, C. J.; Elvekrog, M. M.; Gibney, B. R. *Nucleic Acids Res.* **2008**, *36*, D307-313.
(68) Shifman, J. M.; Gibney, B. R.; Sharp, R. E.; Dutton, P. L. *Biochemistry* **2000**, *39*, 14813-21.
(69) Paoli, M.; Marles-Wright, J.; Smith, A. *DNA Cell Biol.* **2002**, *21*, 271-80.
(70) Varadarajan, R.; Zewert, T. E.; Gray, H. B.; Boxer, S. G. *Science* **1989**, *243*, 69-72.
(71) Rivera, M.; Seetharaman, R.; Girdhar, D.; Wirtz, M.; Zhang, X.; Wang, X.; White, S. *Biochemistry* **1998**, *37*, 1485-94.
(72) Gunner, M. R.; Honig, B. *Proc. Natl. Acad. Sci. U.S.A.* **1991**, *88*, 9151-5.
(73) Bertrand, P.; Mbarki, O.; Asso, M.; Blanchard, L.; Guerlesquin, F.; Tegoni, M. *Biochemistry* **1995**, *34*, 11071-9.
(74) Fisher, M. T.; Sligar, S. G. *J. Am. Chem. Soc.* **1985**, *107*, 5018-5019.
(75) Battistuzzi, G.; Borsari, M.; Cowan, J. A.; Ranieri, A.; Sola, M. *J. Am. Chem. Soc.* **2002**, *124*, 5315-5324.
(76) Kennedy, M. L.; Gibney, B. R. *Curr. Opin. Struct. Biol.* **2001**, *11*, 485-90.
(77) Tran, R.; Boon, E. M.; Marletta, M. A.; Mathies, R. A. *Biochemistry* **2009**, *48*, 8568-8577.
(78) Abraham, D. J.; Leo, A. J. *Proteins* **1987**, *2*, 130-52.
(79) Pascher, T.; Chesick, J. P.; Winkler, J. R.; Gray, H. B. *Science* **1996**, *271*, 1558-60.
(80) Antonini, E.; Brunori, M. *Hemoglobin and Myoglobin in Their Reactions with Ligands*; 1st ed.; North-Holland Publishing Company: Amsterdam, 1971; Vol. 21.
(81) Albright, T., Burdett, J.K., and Whangbo, M. *Orbital Interactions in Chemistry*; Wiley & Sons: New York, 1985.
(82) Patra, R.; Chaudhary, A.; Ghosh, S. K.; Rath, S. P. *Inorg. Chem.* **2008**, *47*, 8324-8335.
(83) Kadish, K. M.; Lin, M.; Van Caemelbecke, E.; De Stefano, G.; Medforth, C. J.; Nurco, D. J.; Nelson, N. Y.; Krattinger, B.; Muzzi, C. M.; Jaquinod, L.; Xu, Y.; Shyr, D. C.; Smith, K. M.; Shelnutt, J. A. *Inorg. Chem.* **2002**, *41*, 6673-87.
(84) Russwurm, M.; Koesling, D. *EMBO J.* **2004**, *23*, 4443-50.
(85) Olea, C., Jr.; Herzik, M. A., Jr.; Kuriyan, J.; Marletta, M. A. *Protein Sci.* **2010**, *19*, 881-887.
(86) Erbil, W. K.; Price, M. S.; Wemmer, D. E.; Marletta, M. A. *Proc. Natl. Acad. Sci. U.S.A.* **2009**, *106*, 19753-60.
(87) Zhao, Y.; Schelvis, J. P.; Babcock, G. T.; Marletta, M. A. *Biochemistry* **1998**, *37*, 4502-9.

(88) Lee, W. C.; Reniere, M. L.; Skaar, E. P.; Murphy, M. E. *J. Biol. Chem.* **2008**, *283*, 30957-63.
(89) Weinert, E. E.; Plate, L.; Whited, C. A.; Olea, C., Jr.; Marletta, M. A. *Angew. Chem., Int. Ed. Engl.* **2010**, *49*, 720-3.
(90) Winter, M. B.; McLaurin, E. J.; Reece, S. Y.; Olea, C., Jr.; Nocera, D. G.; Marletta, M. A. *J. Am. Chem. Soc.* **2010**, *In Press*.
(91) Hoffman, B. M. *J. Am. Chem. Soc.* **1975**, *97*, 1688-1694.
(92) McNaughton, L.; Hernandez, G.; LeMaster, D. M. *J. Am. Chem. Soc.* **2003**, *125*, 3813-3820.
(93) Huang, Y.; Doyle, M. L.; Ackers, G. K. *Biophys. J.* **1996**, *71*, 2094-105.
(94) Woodward, J. J.; Martin, N. I.; Marletta, M. A. *Nat. Methods* **2007**, *4*, 43-5.
(95) Teale, F. W. *Biochim. Biophys. Acta* **1959**, *35*, 543.
(96) Li, J. M.; Umanoff, H.; Proenca, R.; Russell, C. S.; Cosloy, S. D. *J. Bacteriol.* **1988**, *170*, 1021-5.
(97) Gilles-Gonzalez, M. A.; Gonzalez, G.; Perutz, M. F.; Kiger, L.; Marden, M. C.; Poyart, C. *Biochemistry* **1994**, *33*, 8067-73.
(98) Aono, S.; Kato, T.; Matsuki, M.; Nakajima, H.; Ohta, T.; Uchida, T.; Kitagawa, T. *J. Biol. Chem.* **2002**, *277*, 13528-38.

Appendix

Table A1. Heme deviations from planarity of P115A and wild-type *Tt* H-NOX[a]

	rms deviation[b]	Saddling[c]	Ruffling[c]	Tilt[e] (degrees)
P115A				
Heme A	0.221	-0.499	-0.612	80
Heme B	0.224	-0.395	-0.766	84
Heme C	0.123	-0.043	-0.488	88
Heme D	0.147	0.066	-0.517	87
Wild-type monoclinic[d]				
Heme A	0.460	-1.069	-1.105	78
Heme B	0.330	-0.634	-0.814	86
Wild-type orthorhombic[d]				
Heme A	0.450	-1.092	-1.094	80
Heme B	0.440	-0.994	-1.210	81

[a]Fe(II)-O_2 complexes.

[b]rms deviation from planarity in angstroms.

[c]Heme conformations calculated using normal-coordinate analysis [19,24]. The numerical value shown is the displacement along the normal mode in angstroms.

*d*19

[e]Calculated using the least squares plane of the 4 pyrrole nitrogens in the heme (other atoms were excluded due to the high degree of distortion) and the five imidazole ring atoms of H102 in MOLEMAN2 [52]. The acute angle is shown.

Table A2. Heme deviations from planarity in the crystal structure of P115A

Angles between pyrrole groups in P115A and wild-type H-NOX[a]						
	ΦA-B	ΦB-C	ΦC-D	ΦD-A	ΦA-C	ΦB-D
P115A						
Heme A	8.86	12.04	14.26	10.25	15.22	16.35
Heme B	8.65	12.71	17.05	11.15	16.55	17.43
Heme C	1.16	10.43	8.79	8.35	9.71	9.51
Heme D	10.31	15.20	9.88	0.28	9.69	10.07

Wild-type orthorhombic[b]						
heme A	15.30	20.00	29.30	23.00	32.10	28.00
heme B	21.80	15.20	28.00	23.90	30.90	31.80
Wild-type monoclinic[b]						
heme A	17.30	18.20	24.10	27.30	32.60	27.40
heme B	15.90	9.80	26.90	11.50	16.50	27.40

[a]ΦA-B, ΦB-C, etc. refer to the angles in degrees between the planes formed by pyrrole groups A and B, and B and C, respectively.

*b*19

Table A3. N-terminal and overall rms deviation of P115A from wild-type *Tt* H-NOX.

Rms deviation from wild-type[a]		
	N-terminal[b] rmsd (Å)	Overall[c] (Å)
P115A		
Molecule A	2.07	1.68
Molecule B	2.07	1.64
Molecule C	2.72	2.12
Molecule D	3.76	2.77

[a]The monoclinic Molecule A wild-type (PDB ID 1U55) *Tt* H-NOX was used to calculate P115A rms deviation from wild-type.

[b]*Tt* H-NOX residues 1-83 were used for the analysis.

[c]All *Tt* H-NOX residues (1-188) were used in analysis.

Figures A1a-d. Alpha carbon difference distance matrix plots (DDMP) of wild-type *Tt* H-NOX vs. P115A Molecules A-D (Structural Biology at Yale University, New Haven, CT). The most significant changes occur with respect to the N-terminal region (residues 1-83). The C-terminal residues have no change with respect to each other from wild-type. Regions in residues 109-113 are part of a disordered loop in all *Tt* H-NOX mutants.

Figure A1a.

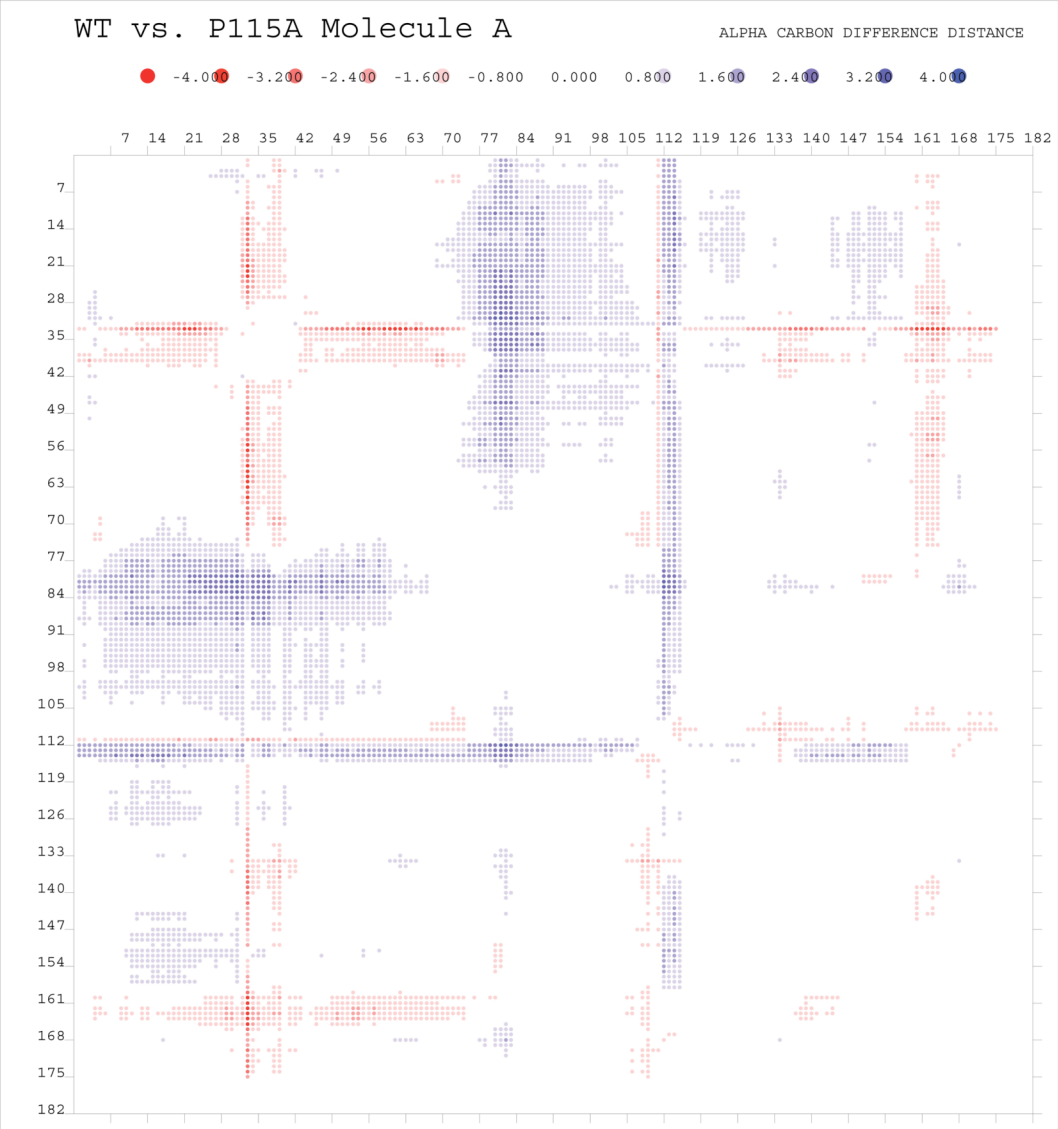

Figure A1b.

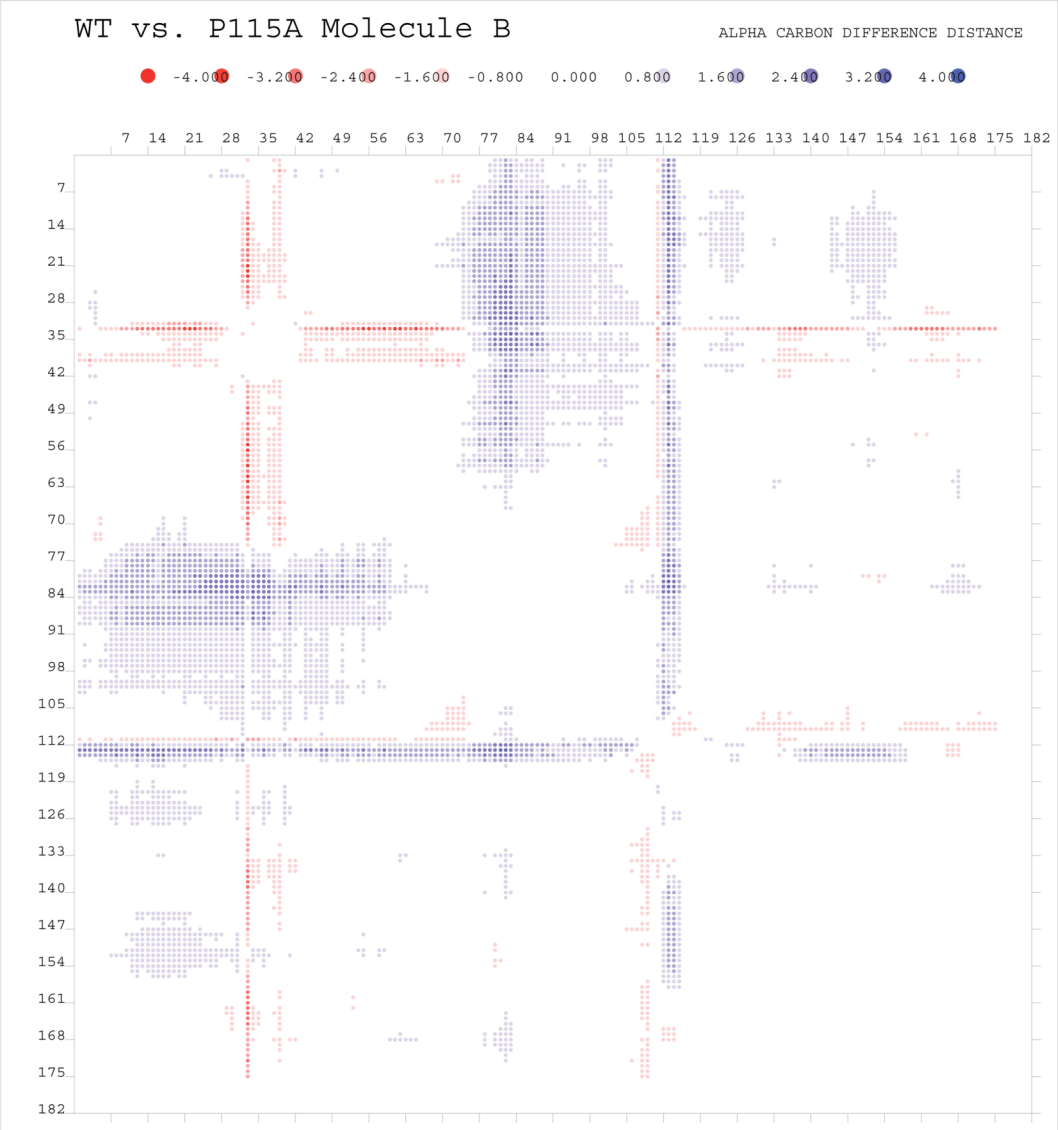
WT vs. P115A Molecule B
ALPHA CARBON DIFFERENCE DISTANCE
-4.000 -3.200 -2.400 -1.600 -0.800 0.000 0.800 1.600 2.400 3.200 4.000
7 14 21 28 35 42 49 56 63 70 77 84 91 98 105 112 119 126 133 140 147 154 161 168 175 182

Figure A1c.

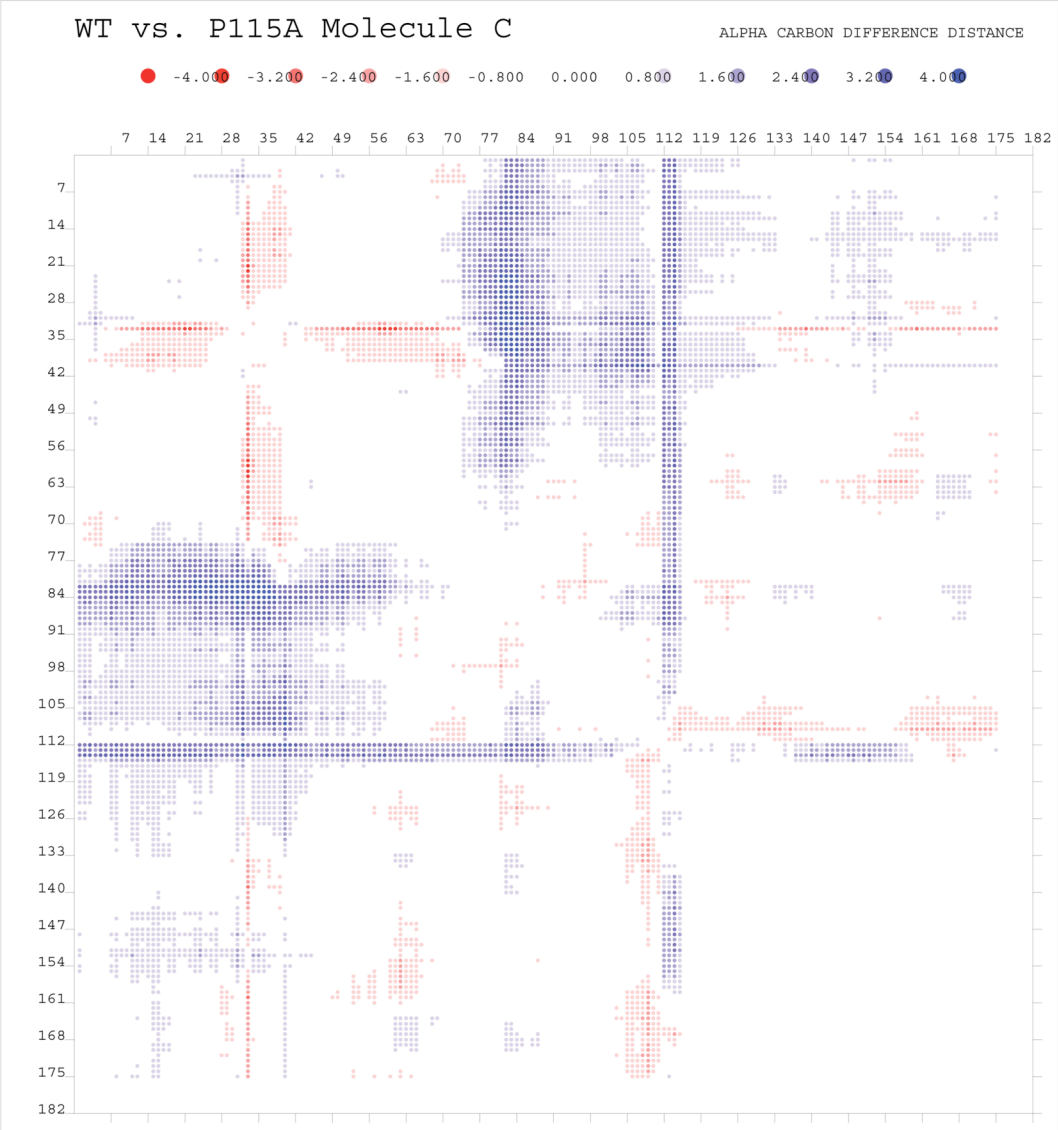
WT vs. P115A Molecule C
ALPHA CARBON DIFFERENCE DISTANCE
-4.000 -3.200 -2.400 -1.600 -0.800 0.000 0.800 1.600 2.400 3.200 4.000
7 14 21 28 35 42 49 56 63 70 77 84 91 98 105 112 119 126 133 140 147 154 161 168 175 182

Figure A1d.

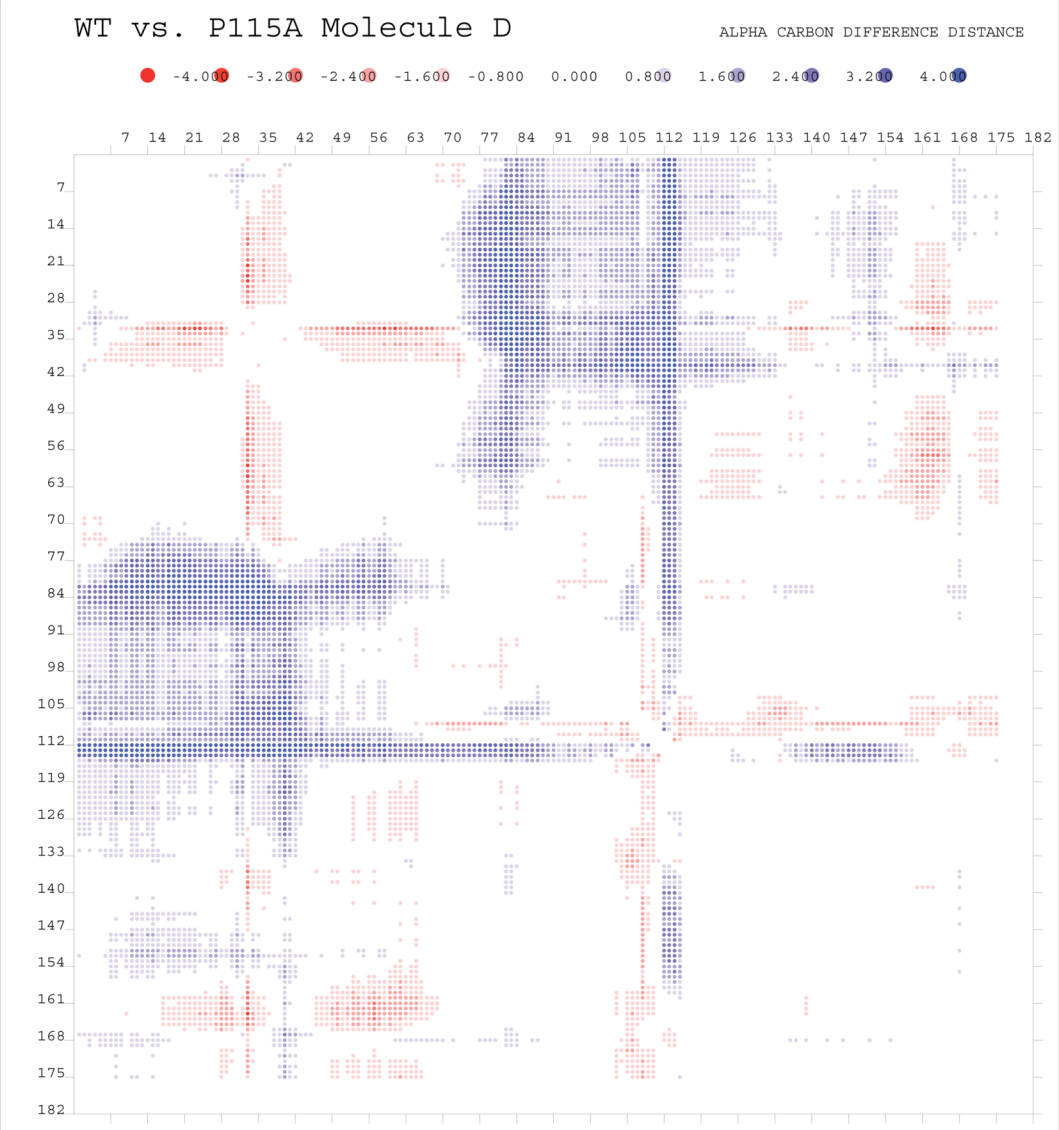

Table A4. O_2-binding kinetic constants for *Tt* H-NOX and some ferrous heme proteins

Protein	K_D (nM)	k_{on} ($\mu M^{-1}s^{-1}$)	k_{off} (s^{-1})
Tt H-NOX[a]	89.7 ± 6.2	13.6 ± 1.0	1.22 ± 0.09
P115A[b]	21.2 ± 2.1	10.4 ± 1.1	0.22 ± 0.01
Sw Mb[c]	880	17	15
Bj FixL[d]	140000	0.14	20
HemAT-B[e]	720	32	23

*a*12

[b]this work

*c*25

*d*97

*e*98

Table A5. Net partition coefficient difference of mutants of *Tt* H-NOX

	π^a
I5L	0.11
I5L/P115A	-0.38
P115A	-0.49

[a] Net change in partition coefficient calculated using methods from Abraham and Leo. [78]

Table A6. Heme deviations from planarity of mutants of and wild-type *Tt* H-NOX[a]

	rms deviation[b]	Saddling[c]	Ruffling[c]	Tilt[f] (degrees)
I5L				
Heme A	0.34	-0.832	-0.634	81
Heme B	0.34	-0.816	-0.758	79
I5L/P115A				
Heme A	0.20	-0.448	-0.216	88
Heme B	0.16	-0.415	-0.261	86
P115A[d]				
Heme A	0.22	-0.499	-0.612	80
Heme B	0.22	-0.395	-0.766	84
Heme C	0.12	-0.043	-0.488	88
Heme D	0.15	0.066	-0.517	87
Wild-type monoclinic[e]				
Heme A	0.46	-1.069	-1.105	78
Heme B	0.33	-0.634	-0.814	86
Wild-type orthorhombic[e]				
Heme A	0.45	-1.092	-1.094	80
Heme B	0.44	-0.994	-1.210	81

[a]Fe(II)-O_2 complexes.

[b]rms deviation from planarity in angstroms.

[c]Heme conformations calculated using normal-coordinate analysis [19,24]. The numerical value shown is the displacement along the normal mode in angstroms.

d 39

*e*19

[f]Calculated using the least squares plane of the 4 pyrrole nitrogens in the heme (other atoms were excluded due to the high degree of distortion) and the five imidazole ring atoms of H102 in MOLEMAN2 [52]. The acute angle is shown.

Table A7. Heme deviations from planarity in the crystal structure of P115A

Angles between pyrrole groups in P115A and wild-type H-NOX[a]						
	ΦA-B	ΦB-C	ΦC-D	ΦD-A	ΦA-C	ΦB-D
I5L						
Heme A	10.58	6.97	26.14	21.01	17.08	24.69
Heme B	11.02	12.42	23.84	19.18	21.05	23.90
I5L/P115A						
Heme A	2.21	6.46	18.13	14.72	8.10	13.92
Heme B	1.29	8.19	13.74	9.53	8.20	10.81
P115A[b]						
Heme A	8.86	12.04	14.26	10.25	15.22	16.35
Heme B	8.65	12.71	17.05	11.15	16.55	17.43
Heme C	1.16	10.43	8.79	8.35	9.71	9.51
Heme D	10.31	15.20	9.88	0.28	9.69	10.07
Wild-type orthorhombic[c]						
heme A	15.30	20.00	29.30	23.00	32.10	28.00
heme B	21.80	15.20	28.00	23.90	30.90	31.80
Wild-type monoclinic[c]						
heme A	17.30	18.20	24.10	27.30	32.60	27.40
heme B	15.90	9.80	26.90	11.50	16.50	27.40

[a]ΦA-B, ΦB-C, etc. refer to the angles in degrees between the planes formed by pyrrole groups A and B, and B and C, respectively.

b 39

*c*19

Table A8. Soret and α/β values for ferric wild-type and mutants of *Tt* H-NOX at pH 7.5

Ferric spectra λ max at pH 7.5		
	Soret (nm)	**α/β (nm)**
Wild-type	**415**	**590/550**
I5L	**408**	**588/542**
I5L/P115A	**404**	**615/530**
P115A	**405**	**610/533**

Table A9. N-terminal root mean square deviation (rmsd) values for H102G from wild-type

	N-terminal rmsd (Å) from WT Ferric[a,b]
H102G F1	
Molecule A	2.78
Molecule B	3.20
H102G F2	
Molecule A	2.83
Molecule B	3.78
Molecule C	3.26

[a]The orthorhombic molecule A wild-type (PDB ID 1U56) *Tt* H-NOX was used to calculate

[b]*Tt* H-NOX residues 1-83 were used for the analysis.

Table A10. NSD calculations for wild-type and H102G

	Saddling[a]	Ruffling[a]
Wild-type Ferric[b]		
Heme A	-1.115	-1.171
Heme B	-0.711	-0.554
H102G F1		
Heme A	-0.413	-0.980
Heme B	-0.365	-1.044
H102G F2		
Heme A	-0.263	-1.142

Heme B	-0.497	-1.216
Heme C	-0.725	-1.029

[a]Heme conformations calculated using normal-coordinate structural (NSD) analysis.[24,48] The numerical value shown is the displacement along the normal mode in Å.

b 19

Table A11. Distances of bond in the heme pocket of wild-type and Zn *Tt* H-NOX.

	Metal-His (Å)	Metal-W9 (Å)	Metal-N74 (Å)	Metal-Y140 (Å)	PyrA-Metal (Å)	PyrB-Metal (Å)	PyrC-Metal (Å)	PyrD-Meta (Å)
Zn								
Mol A	**2.15**	**8.48**	**8.32**	**6.13**	**2.08**	**2.05**	**2.01**	**2.14**
Mol B	**2.14**	**8.53**	**8.25**	**5.99**	**2.06**	**2.04**	**2.09**	**2.09**
Mol C	**2.25**	**8.47**	**8.29**	**6.05**	**2.02**	**2.06**	**2.02**	**2.13**
Mol D	**2.15**	**8.53**	**8.3**	**5.98**	**2.08**	**1.96**	**2.1**	**2.14**
Mol E	**2.19**	**8.5**	**8.5**	**6.22**	**2.06**	**2.05**	**2.09**	**2.18**
Mol F	**2.2**		**8.52**	**6.27**	**2.06**	**2.04**	**2.1**	**2.16**
avg	**2.18**	**8.50**	**8.36**	**6.11**				
error	**0.04**	**0.03**	**0.12**	**0.12**				
Ferrous								
Mol A	**2.12**	**6.9**	**6.92**	**5.05**	**1.98**	**1.98**	**1.98**	**1.97**
Mol B	**2.02**	**7.6**	**6.79**	**5.36**	**1.98**	**2**	**1.99**	**2.01**
Mol C	**2.13**	**7.16**	**6.66**	**5.02**	**1.95**	**1.95**	**1.98**	**2.01**
Mol D	**2.07**	**7.17**	**6.8**	**5.14**	**2**	**2**	**1.96**	**1.96**
avg	**2.09**	**7.21**	**6.79**	**5.14**				
error	**0.05**	**0.29**	**0.11**	**0.15**				
Ferric								
Mol A	**2.15**	**6.86**	**6.87**	**4.79**	**1.95**	**1.97**	**1.96**	**1.97**
Mol B	**2.14**	**7.96**	**6.83**	**5.35**	**1.97**	**2.02**	**1.95**	**2.01**
avg	**2.145**	**7.41**	**6.85**	**5.07**				
error	**0.01**	**1.1**	**0.04**	**0.56**				

Table A12. Rmsd from planarity and NSD calculations for Zn *Tt* H-NOX.

	rms deviation[a]	Saddling[b]	Ruffling[b]	Doming[b]
Zn *Tt* H-NOX				
Heme A	0.20	-0.339	-0.248	0.412
Heme B	0.21	-0.333	-0.303	0.451
Heme C	0.21	-0.392	-0.465	0.315
Heme D	0.23	-0.369	-0.560	0.375
Heme E	0.19	-0.237	-0.361	0.345

Heme F	0.19	-0.260	-0.380	0.324

[a]rms deviation from planarity in angstroms.

[b]Heme conformations calculated using normal-coordinate analysis [19,24]. The numerical value shown is the displacement along the normal mode in angstroms.

Table A13. N-terminal root mean square deviation (rmsd) values for Zn *Tt* H-NOX

Rms deviation from wild-type[a]	
	N-terminal[b] rmsd (Å)
Zn *Tt* H-NOX	
Molecule A	4.37
Molecule B	4.33
Molecule C	4.38
Molecule D	4.43
Molecule E	4.29
Molecule F	4.10

[a]The orthorhombic molecule A wild-type (PDB ID 1U55) *Tt* H-NOX was used to calculate

[b]*Tt* H-NOX residues 1-83 were used for the analysis.